STRUCTURAL AND FUNCTIONAL EVALUATION OF THE HUMAN MIDBRAIN

DOPAMINERGIC SYSTEM USING HIGH RESOLUTION MRI AT 7 T

By

MARIAM COASTER

Dissertation

Submitted to the Faculty of the

Graduate School of Vanderbilt University

in partial fulfillment of the requirements

for the degree of

DOCTOR OF PHILOSOPHY

In

Neuroscience

May, 2012

Nashville, Tennessee

Approved:

Professor John C. Gore

Professor David H. Zald

Professor Frank Tong

Professor Ron L. Cowan

Professor Adam W. Anderson

To my parents, Eapen and Susan, for their wholehearted dedication and support throughout life,

and to my husband, Scott, for his commitment and unconditional kindness.

ACKNOWLEDGEMENTS

discussions and have constantly challenged me and helped me think critically as a scientist. Jay Moore was particularly helpful in teaching me about imaging physics, and he has collaborated with me on implementing various imaging protocols. Chris Cannistraci has been resourceful in assisting me with the 7T IRB, as well as the equipment in the scan room. Kristen Merkle has been exceptional at training our study participants and running the imaging paradigm for the functional studies. I also want to acknowledge Dr. Gregory Larkin who designed the task paradigm for the functional imaging studies. The VUIIS MR technologists have all assisted with screening participants and setting up participants in the scanner for data acquisition. Nancy Hagans has kindly aided me on numerous administrative fronts over the years.

I also want to thank my friends and family who have been a tremendous support network throughout this graduate school journey. My friends have walked closely with me through both the uplifting and difficult moments over the years, and I appreciate their constant encouragement through it all. I am deeply grateful to my parents, Eapen and Susan, for their love, support and prayers over the years. I know they have sacrificed a great deal to afford me the best academic opportunities. They have been my cheerleaders since the time I was born and have always believed in me and my potential. I also want to thank my brother, George, and sister-in-law, Rachel, who have been incredibly supportive, helping me stay on course. My sincerest gratitude goes to my husband, Scott. His love and encouragement has been a true blessing in my life, particularly this past year. I appreciate him very much.

TABLE OF CONTENTS

LIST OF FIGURES

LIST OF TABLES

CHAPTER I

INTRODUCTION

The studies described in this dissertation aimed at evaluating the role of ultra-high field magnetic resonance imaging (MRI) in advancing our understanding of the anatomical and functional architecture of subregions within the human ventral midbrain. The ventral tegmental area (VTA) and the substantia nigra pars compacta (SNc) are subcortical areas within the ventral midbrain that primarily synthesize the neurotransmitter, dopamine (DA). DA neurons from these two regions are known to have complex and widespread connections with many cortical and subcortical brain structures, and they have unique firing properties (Grace and Bunney 1984; Grace and Bunney 1984) known to be associated (in rodents and non-human primates) with reward related learning (Schultz and Romo 1990), motivation (Salamone 1996; Ikemoto and Panksepp 1999), attention (Redgrave, Prescott et al. 1999), novelty processing (Reed, Mitchell et al. 1996; Kakade and Dayan 2002), and other goal-directed behaviors (Schultz 1998). While these in vivo studies in rodents and non-human primates offer us a framework for understanding the role of the VTA and the SNc in brain function, the finer distinct and individual functions of these two nuclei in mediating such behaviors, particularly in humans and in disease states, are still to be elucidated. Non-invasive MRI is a technique that has been used to extensively study human brain structure and function in vivo. In particular, high resolution MRI performed in high field magnets (7 Tesla) can be especially beneficial in segmenting the anatomical substructure of brain areas, as well as for detecting functional changes in brain activity between regions that are close in proximity. In this work, we evaluate the potential for exploring the anatomical layout and functional significance of the midbrain VTA and SNc using MRI at 7 Tesla (7 T).

The Midbrain Dopamine System - Anatomical Overview

Anatomy of the VTA and SNc

A brief overview of the anatomy (size, cytoarchitecture and connectivity) of the midbrain is essential in order to understand the necessary parameters, constraints and optimization procedures that must be explored to perform MR imaging of the area.

Size and cytoarchitecture of the VTA and the SN

The VTA and SNc are located in the ventral portion of the midbrain brainstem area and vary both in size and cytoarchitecture. As measured from an atlas, the VTA is approximately 60 mm^3 (Paxinos and Huang 1995) and comprises of DA and GABA (gamma-aminobutyric acid) neurons that are part of the A10 dopaminergic system (Cameron, Wessendorf et al. 1997). These A10 DA fibers are small diameter (15-30 μm) and non-myelinated, ascending in the medial forebrain bundle (Takagi, Shiosaka et al. 1980; Nieuwenhuys, Geeraedts et al. 1982).

In contrast, the SNc is larger, approximately 340 mm^3 in size (Mai, Paxinos et al. 2008) and is part of the A9 dopaminergic system (Dahlstrom and Fuxe 1964; McRitchie, Hardman et al. 1996). The A9 DA fibers, vary in size (20-40 μm) and extend from the medial lemniscus to the lateral border of the cerebral peduncles (Poirier, Giguère et al. 1983). The SN is topographically divided into two subdivisions: the pars compacta and pars reticulata. The compacta cells (SNc) have larger cell bodies, thicker and longer dendrites, numerous dendritic segments and contain denser neuromelanin granules in comparison to the reticulata cells (Braak and Braak 1986; Francois, Yelnik et al. 1987; Yelnik, François et al. 1987). Neurons in the SN comprise dopaminergic cells that have iron containing neuromelanin as well as GABA-ergic cells.

Connections of the VTA and the SN

Directionality and density of interconnections between the VTA/SN and other areas of the brain provide clues regarding the strength and functional significance of their associations. The DA neurons in the VTA have widespread reciprocal connections with subcortical and cortical areas of the brain, making this region a major site of information integration (Phillipson 1979; Woolf and Butcher 1985; Oades and GM. 1987) (Figure1). Through the mesolimbic pathway, the VTA is connected with limbic regions, including the nucleus accumbens (NAc), amygdala, cingulate cortex, and the hippocampal complex. It has efferent and afferent connections with sensory, motor and association areas, the prefrontal cortex and the insular cortex through the mesocortical pathway, as well as with various nuclei of the thalamus and hypothalamus. Reciprocal associations have been shown to be evident between the VTA and dorsal raphe nuclei, locus coeruleus, other brainstem nuclei, the superior colliculus, reticular formation periaqueductal gray, and the spinal cord (Beckstead, Domesick et al. 1979; Simon, Moal et al. 1979; Adell and Artigas 2004). Mesocortical projections tend to have their origin dorso-rostrally in the VTA, and the mesolimbic projections originate in the ventro-caudal VTA (MacBrown and Goldman 1977; Levitt, Rakic et al. 1984). VTA is known to receive glutamatergic input from the laterodorsal tegmentum (in the mesopontine brainstem), and cholinergic input from the pedunculopontine tegmentum (Woolf 1991; Blaha, Allen et al. 1996).

A majority of the efferent-pathways from the SNc form the nigrostriatal circuitry, whereas the afferent pathways primarily comprise the striatonigral circuitry (Selemon and Goldman-Rakic 1990; Hedreen and DeLong 1991; Haber, Fudge et al. 2000) (Figure1). The SNc receives topographically organized input from different parts of the striatum in an inverse dorso-ventral fashion. Sensorimotor areas of the striatum project to the ventro-lateral pallidum and the ventro-lateral SNc. Projections from the central striatum terminate more centrally in both the pallidum and ventral denso-cellular SNc. The ventral striatum projects topographically into the ventral pallidum, VTA and denso-cellular SNc. Cortical projections (mesofrontal) from the SN

3

target dorsal frontal cortices including areas 46, 8B/6M, 4 as well as the anterior cingulate

(Williams and Goldman-Rakic 1998).
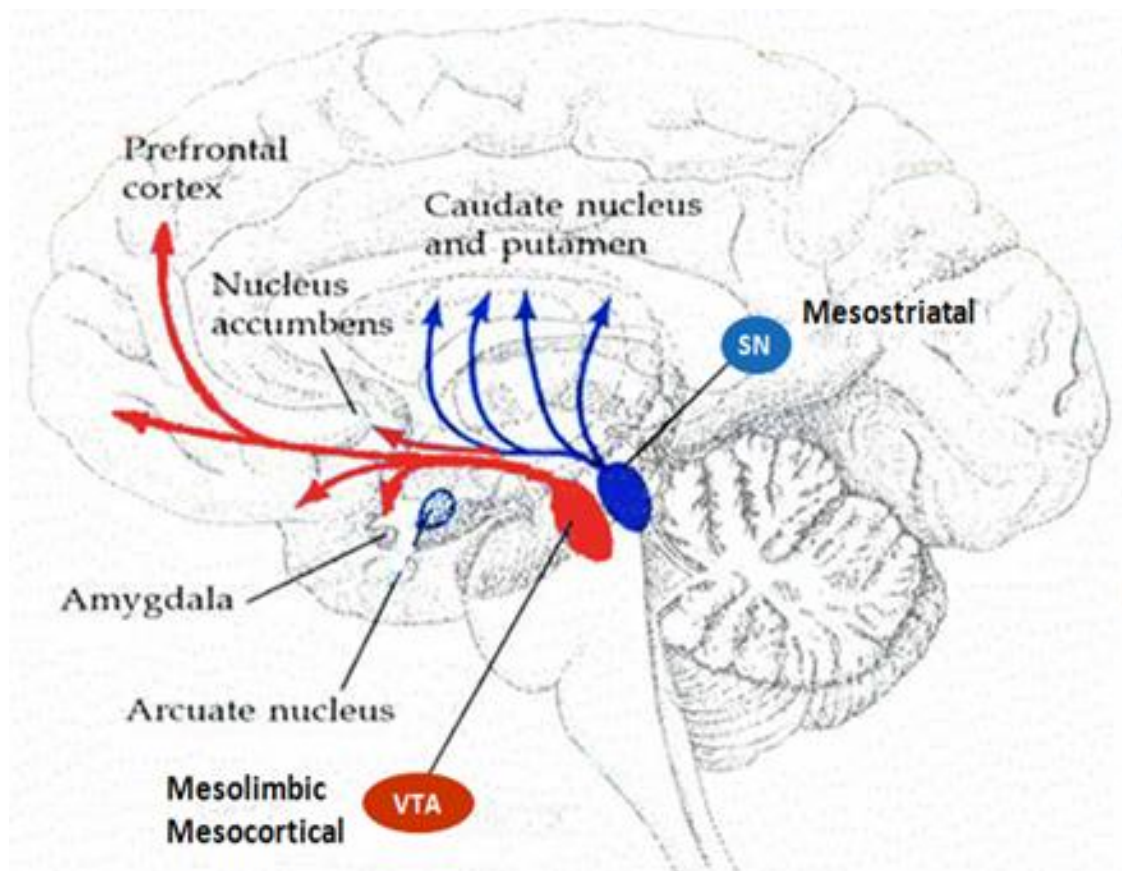
Figure 1: **Major interconnections between the SN and VTA in the human brain.** Blue section represents the mesostriatal pathways, and red sections represent the mesolimbic and mesocortical pathways.

Functional attributes of DA neurons in the VTA and SNc

A considerable number of studies investigating the functional characteristics of the midbrain DA neurons have been performed in non-human primates. Single unit recording studies in monkeys have shown that the phasic or burst firing pattern of midbrain DA neurons (primarily in the VTA and SNc) encodes a learning signal that predicts the error in the occurrence of a rewarding or aversive stimulus (Romo and Schultz 1990; Schultz and Romo 1990; Hollerman and Schultz 1998; Schultz and Dickinson 2000). These neurons responded robustly to primary food and liquid rewards, and conditioned cues predicting the reward. They respond much less, however, to aversive stimuli, such as air puffs, saline drops to the mouth and foot pinches (Mirenowicz and Schultz 1996; Ungless, Magill et al. 2004). Work by Schultz and colleagues also reported that the DA neurons in the VTA and SNc fired in a phasic pattern when the animals were exposed to unexpected or novel aspects of the reward (novel magnitude or reinforcing properties of the reward or novel time of reward delivery) (Ljungberg, Apicella et al. 1992; Hollerman and Schultz 1998).

In contrast, the slowly changing and low concentration tonic firing pattern of the DA neurons may be involved in setting up a motivational state, providing initial input to other neuronal systems subserving reward seeking or general goal-directed functions (Blackburn, Pfaus et al. 1992; Salamone 1996). Beyond reward processing and motivation, DA is also known to be involved in directing attention to salient stimuli in order to prepare an appropriate behavioral response (Schultz 1997; Redgrave, Prescott et al. 1999).

Most of the aforementioned studies thus suggest that midbrain DA neurons are associated with specific behaviors even though it is difficult to draw distinctions between the role of the VTA and SNc in these behaviors. Overall, we learn that the VTA DA neurons likely respond to motivational, rewarding, novel and salient aspects of the stimulus, while the SNc DA neurons are associated with preparing an appropriate behavioral response to the stimulus. These studies provide an important guide to what we may expect to find regarding function in the human

midbrain DA system. It also helps us ascertain the combination of parameters we should use during experimental design in order to robustly stimulate the midbrain dopaminergic regions.

Studying the Midbrain in Humans using MRI

In humans, the midbrain DA system has been extensively studied using Positron Emission Tomography (PET). In PET, radioactive tracer isotopes specifically targeting DA receptors are injected into the body to measure receptor availability (binding potential) at both basal levels and during alterations induced by test conditions. Isotopes commonly used for imaging the DA system include $[^{18}F]$ Fallypride (a D2/D3-selective ligand) and $[^{11}C]$ Raclopride (a selective dopamine D2/D3 antagonist), both of which label the striatal and extrastriatal receptors. Even though DA release can be directly imaged using PET, due to limitations in the accuracy of the detection technique, the available spatial resolution in PET is slightly under a centimeter. The low spatial resolution of this imaging technique thus makes it impractical to study adjacent brain regions, particularly within the midbrain.

MR imaging is a non-invasive technique by which high resolution images of the human brain can be visualized. In this technique, a detectable signal is produced by measuring the spin properties of the hydrogen protons in different tissues. Because the human body is primarily composed of water, organs (e.g., the brain) have a high concentration of hydrogen nuclei. When the human brain is placed in a static uniform magnetic field (B_0), the protons in the tissue tend to align their spins in the direction of the applied magnetic field causing a macroscopic nuclear magnetization. The static magnetic field is approximately 140,000 times the Earth's magnetic field at 7 T.

A radio frequency pulse is then applied at the resonant frequency of the protons (42.57 MHz/ Tesla) tipping its magnetization away from the equilibrium position. When the RF pulse is removed, the protons gradually relax back to align themselves with B_0 while energy is released to

the surrounding medium. During the relaxation process, the protons precess or rotate about the equilibrium axis inducing an electromagnetic signal in the conducting coil around the head. This precession is a vector quantity and has a longitudinal component (*z*) and a transverse component (*xy*). In order to encode spatial information, various gradient coils within the scanner alter the frequency and phase of the proton precession pattern inducing currents that enable localization of the signal. Based on the cellular profile of the area being imaged, different tissues can have varying relaxation rates, 1/T1 and 1/T2, which describe the rates at which the *z* and *xy* components recover towards equilibrium. Therefore, when an MR image is acquired, the visual contrast observed is a result of the relative contributions of T1 or T2 relaxations rates and the proton densities between the tissues. Some tissues can contain other magnetic susceptibility features (iron or the presence of deoxygenated hemoglobin in vasculature) that alter the rate of precession of the proton spins in the transverse direction (T2). Iron and deoxygenated hemoglobin are paramagnetic, causing the proton spins in tissues that contain them to dephase differently (faster) compared to the proton spins in the neighboring regions. Typically, the spins in a tissue with uniform magnetic susceptibility precess in phase (rotate together). However, in regions of local magnetic susceptibility changes (due to iron or deoxygenated hemoglobin), the magnetic field of the tissue becomes highly non-uniform and the proton spins precess out of phase. The decay rate of the transverse magnetization is then 1/T2*. T2 is always greater than T2*. Based on the imaging parameters used, different MR sequences are able to specifically detect T1, T2 or T2* contrast effects in tissues.

With increasing magnetic field strength, the T1 relaxation times get longer and the T2 relaxation times get shorter. Thus T2* effects become more apparent at higher field strengths as signal decays faster in regions that have greater magnetic susceptibility. Knowledge of tissue specific T1, T2 or T2* effects can thus influence the quality of the images acquired. Additionally, the overall signal to noise ratio also increases with MR field strength. Thus by acquiring data at

very high fields, the spatial resolution and sensitivity to small changes in contrast can be

improved, particularly in the midbrain areas (Figure 2).
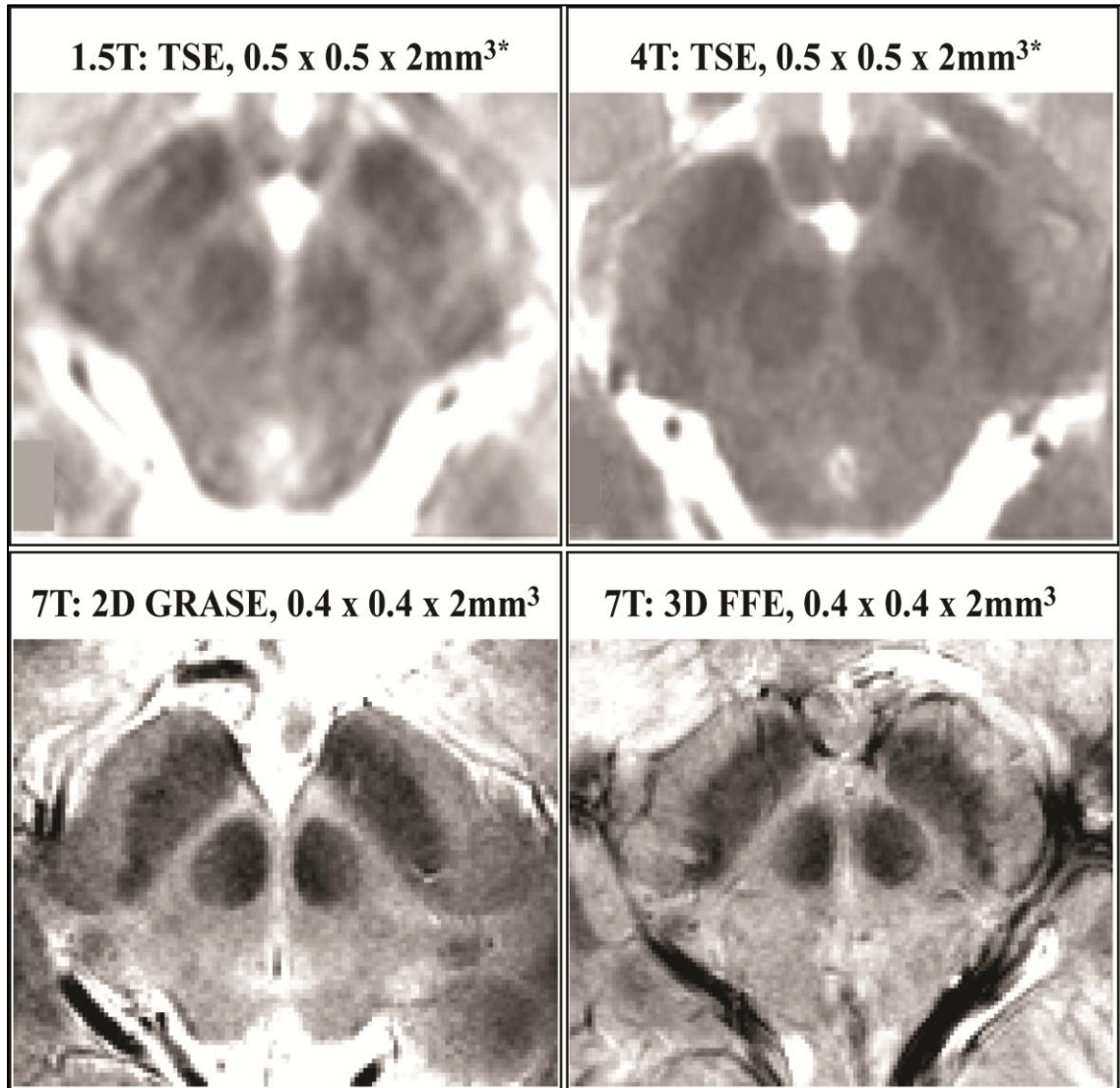
Figure 2: **MRI of the midbrain at different field strengths.** Comparable spatial resolutions at the level of the superior colliculus are presented here for 1.5 Tesla, 4 Tesla and 7 Tesla. **TSE**: Turbo Spin Echo sequence; **GRASE**: GRadient and Spin Echo sequence; **FFE**: Fast Field Echo. The 7 T images were taken at the VUIIS 7 T MR scanner. *(Manova, Habib et al. 2009).

The DA cells in the SNc (housing iron containing neuromelanin) have different magnetic susceptibility properties compared to cells in the adjacent regions. Variations in susceptibility can disturb the local magnetic fields within the midbrain and thereby provide enhanced contrast in pulse sequences that are sensitive to such effects. For example, the SN regions tend to appear darker in MRI images that are sensitive to transverse relaxation (T2, T2*) due to the loss in signal associated with the presence of iron. On the other hand, the VTA does not have cell-specific features with unique magnetic susceptibilities that can be easily distinguished in MR scans. The SN and VTA are adjacent structures, so the anatomy of the VTA can be localized in MR images with respect to the boundary of the SN, in combination with other local topographic landmarks. With the advent of high resolution MRI techniques, anatomy of midbrain areas can be clearly delineated, revealing details close to those seen in histological specimens (Novak, Novak et al. 2001; Thomas, Welch et al. 2008; Manova, Habib et al. 2009) (Figure 3).

Figure 3: Axial slice from a GRASE MRI sequence at 7 T. The image represents a section through the midbrain at the level of the superior colliculus. Inset represents a zoomed version of the image, highlighting the midbrain. Legend of structures include: **SN**: Substantia Nigra; **VTA**: Ventral Tegmental Area; **R**: Red Nucleus; **CP**: Cerebral Peduncles; **MB**: Mammillary Body and **PCA**: Posterior Cerebral Artery.

MRI based on the Blood Oxygen Level Dependent (BOLD) response is a potential way to study the functional significance of the VTA and the SNc brainstem areas. The local magnetic field experienced by the hydrogen protons in the brain can be influenced by changes in the oxygenation within neighboring blood vessels. During neural activity, blood rushes to an area of the brain increasing the local blood flow, blood volume and cerebral metabolism of oxygen in that area. Blood contains high levels of hemoglobin (Hb), an iron containing molecule that can bind to oxygen. At the site of neural activity, when oxygen is being metabolized, blood containing oxygenated Hb (oxy-Hb) gets exchanged for blood containing deoxygenated Hb (deoxy-Hb). Deoxy-Hb is paramagnetic due to unpaired electrons in the iron within the heme group (no longer bound to oxygen atoms) and this induces T2* effects, thereby decreasing the MR signal in an area of neural activity. This initial loss in MR signal is referred to as the initial dip in the BOLD response. In response to the increasing energy and oxygen demand at the site of neural activity, there is a temporary increase in the blood flow and blood volume to the area. This temporary increase in blood flow supplying glucose and oxygen over compensates the energy and oxygen demand in the area, resulting in a decrease in the ratio of deoxy-Hb to oxy-Hb. Thus at the site of neural activity, there is greater oxygen available than what is necessary for oxygen metabolism, thereby decreasing the amount of deoxy-Hb and ultimately increasing the detected MR signal. This effect is known as the Blood Oxygen Level Dependent effect or the BOLD effect (Ogawa, Lee et al. 1990; Kwong, Belliveau et al. 1992). The amplitude, onset and duration of this BOLD effect with respect to a stimulus can be measured using fMRI. Even though the precise relationship between neural activity and BOLD is still controversial, the effect is nonetheless robust and measurable.

The dense microvasculature in the midbrain areas contribute significantly to T2* shortening and may provide enhanced BOLD contrast in T2* sensitive scan sequences. Most fMRI studies involving the brainstem to date have been conducted in low field scanners (1.5 Tesla or 3 Tesla) with imaging protocols that have certain limitations on sensitivity and signal to

13

noise ratios (SNR). Similar to Schultz's finding in non-human primate studies, neuroimaging fMRI (functional MRI) studies in humans have shown that the VTA and ventral striatum are involved in processing positive prediction errors during conditional associative tasks using appetitive or monetary rewards (Berns, McClure et al. 2001; D'Ardenne, McClure et al. 2008; Buckholtz, Treadway et al. 2010). Additionally, the SNc/VTA region was reported, in another study, to preferentially respond to stimulus novelty over other forms of stimulus salience including target response and negative emotional arousal (Bunzeck and Duzel 2006). While these neuroimaging studies demonstrated the presence of task-related BOLD activity in the midbrain, due to limited spatial resolution and other imaging constraints, it was unclear if the BOLD related brain activity was localized to the VTA or the SN or both (Figure 4). At higher field strengths (7 Tesla or higher), some of these limitations can be ameliorated because of the ability to view smaller voxel dimensions from more localized regions, and because BOLD signals increase with increasing field strength (Turner, Jezzard et al. 1993; Bandettini, Wong et al. 1994; Gati, Menon et al. 1997; Triantafyllou, Hoge et al. 2005).
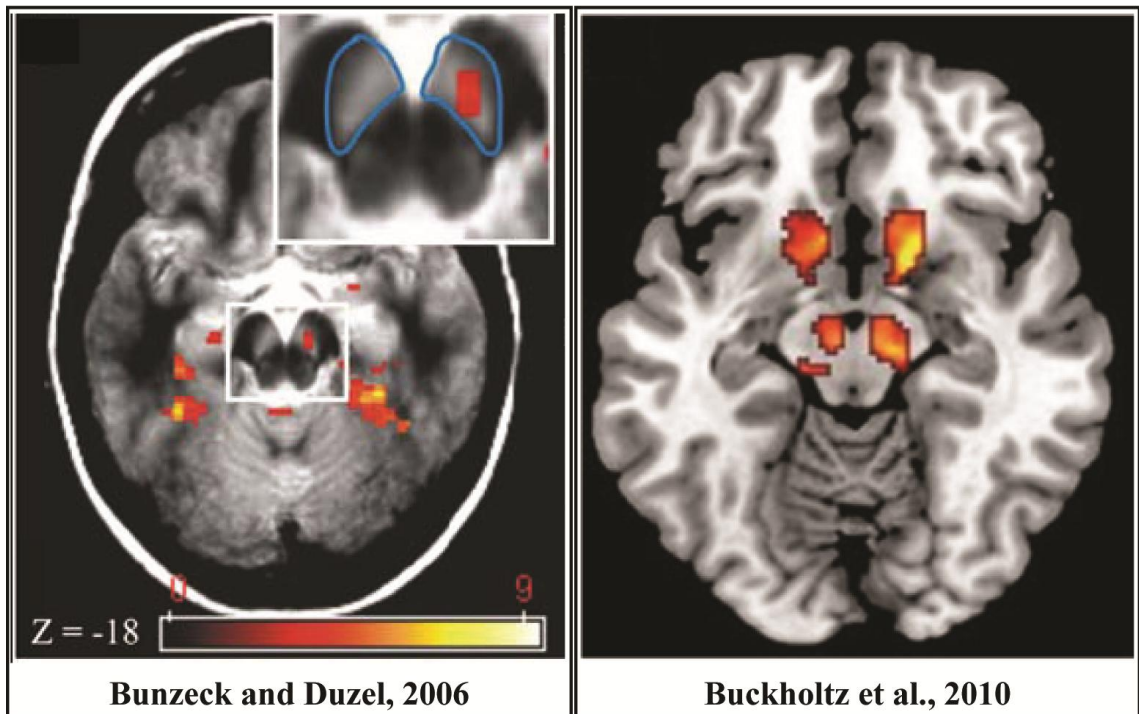
Figure 4: **fMRI neuroimaging studies in humans.** Studies show BOLD activation maps for novelty (Left) and reward related learning (Right) tasks. These maps are overlaid on anatomical image sections of the midbrain.

Challenges and limitations in using the 7 T for studying the midbrain

Higher field strength imaging has various technical challenges, especially in an area that is deep in the brainstem. These challenges include signal artifacts and distortions caused by macroscopic magnetic susceptibility variations in the brain, and the behavior of radio frequency coils at high fields. In addition, the B_0 field (static magnetic field) fluctuations caused by physiological motion associated with cardiac pulsatility and respiration cannot be easily mitigated.

The midbrain is located near the interpeduncular fossa, which is an area of CSF (Cerebral Spinal Fluid) flow. Magnetic susceptibility varies within and across this liquid-tissue boundary, thereby distorting the applied magnetic field. This results in signal artifacts which include geometric distortions (macroscopic spatial image distortion) and variations in signal intensity (microscopic, due to dephasing of the proton spins). Moreover, since the imaging plane covers the ear canal, signal drop out and various ghosting artifacts can also be observed near the midbrain. All these can affect the spatial and temporal stability of acquired images.

Noise also increases as you go to higher field strengths. The intrinsic noise (thermal noise in the body and from scanner electronics) increases with increasing signal bandwidth and object size, and the physiological noise caused by respiration and cardiac pulsations increases with increasing field strength (Triantafyllou, Hoge et al. 2005). In addition to the contribution of cardiac and respiratory cycles, physiologic noise is also known to include a BOLD component comprising hemodynamic and metabolic fluctuations in gray matter (Weisskoff 1996; Krüger, Kastrup et al. 2001). High noise can potentially reduce signal detectability and hinder the ability to observe reliable and reproducible changes in signal. Improved shimming techniques (Koch, McIntyre et al. 2006; Gelderen, Zwart et al. 2007), phase navigation algorithms (Barry, Klassen et al. 2008; Versluis, Peeters et al. 2010) and various post-processing steps have been shown to overcome these limitations. These post-processing algorithms include retrospectively correcting for physiologic noise sources (Le and Hu 1996; Glover, Li et al. 2000; Thomas, Harshman et al.

2002), regressing out phase modulations in large blood vessels (Menon 2002; Barry, Williams et al. 2010) and the use of a regressor of no interest in temporally, but not functionally correlated areas (Krebs, Woldorff et al. 2010). High resolution imaging at 7 T optimized with complementary imaging protocols tailored to the midbrain promises to improve localization of the BOLD signal from functionally significant SN and VTA regions.

Specific Aims

Non-human primate work reviewed in this chapter provided a foundation to understand the distinct anatomy and structural connections of the SN and VTA, as well as their functional relevance in various goal directed behaviors. In order to translate this knowledge base into the human realm and explore the fine grained anatomy and individual functions within the SN and VTA, we used high resolution MRI at ultra-high field strengths (7 T). The aims of this dissertation were, 1) to characterize the anatomy of the midbrain dopaminergic system using various 7 T imaging sequences that delineate structure, substructure as well as vasculature, 2) to demonstrate the feasibility of detecting functional BOLD contrast in the SN and VTA for individuals using a monetary incentive delay fMRI task and to establish the reproducibility of the functional results in multiple individuals, and 3) to quantify and evaluate specific acquisition and analysis strategies designed to overcome technical challenges of 7 T fMRI of the midbrain SN and VTA.

References

Adell, A. and F. Artigas (2004). "The somatodendritic release of dopamine in the ventral tegmental area and its regulation by afferent transmitter systems." Neurosci Biobehav Rev. 28(4): 415-431.

Bandettini, P., E. Wong, et al. (1994). "MRI of human brain activation at 0.5 T 1.5 T, and 3.0 T: comparison of delta R2 * and functional contrast to noise ratio." <u>Proceedings ISMRM</u> 434.

Barry, R. L., L. M. Klassen, et al. (2008). "Hybrid two-dimensional navigator correction: A new technique tosuppress respiratory-induced physiological noise in multi-shot echo-planar functional MRI." <u>NeuroImage</u> 39(3): 1142-1150.

Barry, R. L., J. M. Williams, et al. (2010). "Evaluation of preprocessing steps to compensate for magnetic field distortions due to body movements in BOLD fMRI." <u>Magn Reson Imaging</u> 28(2): 235-244.

Beckstead, R., V. Domesick, et al. (1979). "Efferent connections of the substantia nigra and ventral tegmental area in the rat." <u>Brain Res</u> 175(2): 191-217.

Berns, G. S., S. M. McClure, et al. (2001). "Predictability Modulates Human Brain Response to Reward." <u>The Journal of Neuroscience</u> 21(8): 2793-2798.

Blackburn, J., J. Pfaus, et al. (1992). "Dopamine functions in appetitive and defensive behaviours." <u>Prog Neurobiol.</u> 39(3): 247-279.

Blaha, C., L. Allen, et al. (1996). "Modulation of dopamine efflux in the nucleus accumbens after cholinergic stimulation of the ventral tegmental area in intact, pedunculopontine tegmental nucleus-lesioned, and laterodorsal tegmental nucleus-lesioned rats." <u>J Neurosci.</u> 16(2): 714-722.

Braak, H. and E. Braak (1986). "Nuclear configuration and neuronal types of the nucleus niger in the brain of the human adult." <u>Hum Neurobiol.</u> 5(2): 71-82.

Buckholtz, J. W., M. T. Treadway, et al. (2010). "Mesolimbic dopamine reward system hypersensitivity in individuals with psychopathic traits." <u>Nat Neurosci.</u> 13(4): 419-421.

Bunzeck, N. and E. Duzel (2006). "Absolute Coding of Stimulus Novelty in the Human Substantia Nigra/VTA." <u>Neuron</u> 51(3): 369-379.

Cameron, D. L., M. W. Wessendorf, et al. (1997). "A subset of ventral tegmental area neurons is inhibited by dopamine, 5-hydroxytryptamine and opioids." <u>Neuroscience</u> 77(1): 155-166.

D'Ardenne, K., S. M. McClure, et al. (2008). "BOLD Responses Reflecting Dopaminergic Signals in the Human Ventral Tegmental Area." <u>Science</u> 319(5867): 1264-1267.

Dahlstrom, A. and K. Fuxe (1964). "Evidence for the existence of monoamine-containing neurons in the central nervous system. I. Demonstration of monoamines in the cell bodies of brain stem neurons." Acta Physiol. Scand. 62: 1-80.

Francois, C., J. Yelnik, et al. (1987). "Golgi Study of the Primate Substantia Nigra II. Spatial Organization of Dendritic Arborizations in Relation to the Cytoarchitectonic Boundaries and to the Striatonigral Bundle." The Journal of Comparative Neurology 265(4): 473-493.

Gati, J., R. Menon, et al. (1997). "Experimental determination of the BOLD field strength dependence in vessels and tissue." Magn Reson Med. 38(2): 296-302.

Gelderen, P. v., J. A. d. Zwart, et al. (2007). "Real-Time Shimming to Compensate for Respiration-Induced B0 Fluctuations." Magn Reson Med 57(2): 362-368.

Glover, G. H., T.Q. Li, et al. (2000). "Image-based method for retrospective correction of physiological motion effects in fMRI: RETROICOR." Magn Reson Imaging **44**(1): 162-167.

Grace, A. A. and B. S. Bunney (1984). "The Control of Firiing Pattern in Nigral Dopamine Neurons: Burst Firing." The Journal of Neuroscience 4(11): 2877-2890.

Grace, A. A. and B. S. Bunney (1984). "The Control of Firing Pattern in Nigral Dopmaine Neurons: Single Spiking Firing." The Journal of Neuroscience 4(11): 2866-2876.

Haber, S., J. Fudge, et al. (2000). "Striatonigrostriatal pathways in primates form an ascending spiral from the shell to the dorsolateral striatum." J Neurosci. 20(6): 2369-2382.

Hedreen, J. and M. DeLong (1991). "Organization of striatopallidal, striatonigral, and nigrostriatal projections in the macaque." J Comp Neurol. 304(4): 569-595.

Hollerman, J. and W. Schultz (1998). "Dopamine neurons report an error in the temporal prediction of reward during learning." Nat Neurosci. 1(4): 304-309.

Ikemoto, S. and J. Panksepp (1999). "The role of nucleus accumbens dopamine in motivated behavior: a unifying interpretation with special reference to reward-seeking." Brain Research Reviews 31(1): 6–41.

Kakade, S. and P. Dayan (2002). "Dopamine: generalization and bonuses." Neural Networks 15: 549-559.

Koch, K., S. McIntyre, et al. (2006). "Dynamic shim updating on the human brain." J Magn Reson. 180(2): 286-296.

Krebs, R. M., M. G. Woldorff, et al. (2010). "High-field FMRI reveals brain activation patterns underlying saccade execution in the human superior colliculus." PLoS One 5(1): e8691.

Krüger, G., A. Kastrup, et al. (2001). "Neuroimaging at 1.5 T and 3.0 T: comparison of oxygenation-sensitive magnetic resonance imaging." Magn Reson Med 45(4): 595-604.

Kwong, K., J. Belliveau, et al. (1992). "Dynamic magnetic resonance imaging of human brain activity during primary sensory stimulation." Proc Natl Acad Sci U S A. **89**(12): 5675-5679.

Le, T. and X. Hu (1996). "Retrospective estimation and correction of physiological artifacts in fMRI by direct extraction of physiological activity from MR data." Magn Reson Med. **35**(3): 290.

Levitt, P., P. Rakic, et al. (1984). "Region-specific distribution of catecholamine afferents in primate cerebral cortex: a fluorescence histochemical analysis." J Comp Neurol. 227(1): 23-36.

Ljungberg, T., P. Apicella, et al. (1992). "Responses of monkey dopamine neurons during learning of behavioral reactions." J Neurophysiol. 67(1): 145-163.

MacBrown, R. and P. Goldman (1977). "Catecholamines in neocortex of rhesus monkeys: regional distribution and ontogenetic development." Brain Res. 124(3): 576-580.

Mai, J. K., G. Paxinos, et al. (2008). Atlas of the Human Brain New York, Academic Press.

Manova, E. S., C. A. Habib, et al. (2009). "Characterizing the Mesencephalon Using Susceptibility-Weighted Imaging." American Journal of Neurobiology 30: 569-574.

McRitchie, D., C. Hardman, et al. (1996). "Cytoarchitectural distribution of calcium binding proteins in midbrain dopaminergic regions of rats and humans." J Comp Neurol. 364(1): 121-150.

Menon, R. S. (2002). "Postacquisition suppression of large-vessel BOLD signals in high-resolution fMRI." Magn Reson Imaging 47(1): 1-9.

Mirenowicz, J. and W. Schultz (1996). "Preferential activation of midbrain dopamine neurons by appetitive rather than aversive stimuli." <u>Nature</u> 379(6564): 449-451.

Nieuwenhuys, R., L. Geeraedts, et al. (1982). "The medial forebrain bundle of the rat. I. General introduction." <u>J Comp Neurol</u> 206(1): 49-81.

Novak, P., V. Novak, et al. (2001). "High resolution MRI of the brainstem at 8 T." <u>J Comput Assist Tomogr.</u> 25(2): 242-246.

Oades, R. and G. H. GM. (1987). "Ventral tegmental (A10) system: neurobiology. 1. Anatomy and connectivity." <u>Brain Research</u> 434(2): 117-165.

Ogawa, S., T. Lee, et al. (1990). "Oxygenation-sensitive contrast in magnetic resonance image of rodent brain at high magnetic fields." <u>Magn Reson Med.</u> **14**(1): 68-78.

Paxinos, G. and X.-F. Huang (1995). <u>Atlas of the Human Brainstem</u>. Sandiego, CA, Academic Press.

Phillipson, O. (1979). "Afferent projections to the ventral tegmental area of Tsai and interfascicular nucleus: a horseradish peroxidase study in the rat." <u>J Comp Neurol.</u> 187(1): 117-143.

Poirier, L., M. Giguère, et al. (1983). "Comparative morphology of the substantia nigra and ventral tegmental area in the monkey, cat and rat." <u>Brain Res Bull.</u> 11(3): 371-397.

Redgrave, P., T. J. Prescott, et al. (1999). "Is the short-latency dopamine response too short to signal reward error?" <u>Trends in Neurosciences</u> 22(4): 146-151.

Reed, P., C. Mitchell, et al. (1996). "Intrinsic reinforcing properties of putatively neutral stimuli in an instrumental two-lever discrimination task." <u>Animal Learning & Behavior</u> 24(1): 38-45.

Romo, R. and W. Schultz (1990). "Dopamine neurons of the monkey midbrain: contingencies of responses to active touch during self-initiated arm movements." <u>J Neurophysiol.</u> 63(3): 592-606.

Salamone, J. D. (1996). "The behavioral neurochemistry of motivation: methodological and conceptual issues in studies of the dynamic activity of nucleus accumbens dopamine." <u>Journal of Neuroscience Methods</u> 64(2): 137-149.

Schultz, W. (1997). "Dopamine neurons and their role in reward mechanisms." <u>Curr Opin Neurobiol.</u> 7(2): 191-197.

Schultz, W. (1998). "Predictive Reward Signal of Dopamine Neurons." <u>Journal of Neurophysiology</u> 80: 1-27.

Schultz, W. and A. Dickinson (2000). "Neuronal coding of prediction errors." <u>Annu Rev Neurosci.</u> 23: 473-500.

Schultz, W. and R. Romo (1990). "Dopamine Neurons of the Monkey Midbrain: Contingencies of Responses to Stimuli Eliciting Immediate Behavioral Reactions." <u>Journal of Neurophysiology</u> 63(3): 607-624.

Selemon, L. and P. Goldman-Rakic (1990). "Topographic intermingling of striatonigral and striatopallidal neurons in the rhesus monkey." <u>J Comp Neurol.</u> 297(3): 359-376.

Simon, H., M. L. Moal, et al. (1979). "Efferents and afferents of the ventral tegmental-A10 region studied after local injection of [3H]leucine and horseradish peroxidase." <u>Brain Res.</u> 178(1): 17-40.

Takagi, H., S. Shiosaka, et al. (1980). "Ascending components of the medial forebrain bundle from the lower brain stem in the rat, with special reference to raphe and catecholamine cell groups. A study by the HRP method." <u>Brain Research</u> 193(2): 315-337.

Thomas, B. P., E. B. Welch, et al. (2008). "High-Resolution 7 T MRI of the Human Hippocampus In Vivo." <u>Journal of Magnetic Resonance Imaging</u> 28: 1266-1272.

Thomas, C., R. Harshman, et al. (2002). "Noise reduction in BOLD-based fMRI using component analysis." <u>Neuroimage</u> **17**(3): 1521-1537.

Triantafyllou, C., R. D. Hoge, et al. (2005). "Comparison of physiological noise at 1.5 T, 3 T and 7 T and optimization of fMRI acquisition parameters." <u>NeuroImage</u> 26(1): 243-240.

Turner, R., P. Jezzard, et al. (1993). "Functional mapping of the human visual cortex at 4 and 1.5 tesla using deoxygenation contrast EPI." <u>Magn Reson Med.</u> 29(2): 277-279.

Ungless, M., P. Magill, et al. (2004). "Uniform inhibition of dopamine neurons in the ventral tegmental area by aversive stimuli." <u>Science</u> 303(5666): 2040-2042.

Versluis, M. J., J. M. Peeters, et al. (2010). "Origin and reduction of motion and f0 artifacts in high resolution T2*-weighted magnetic resonance imaging: application in Alzheimer's disease patients." NeuroImage 51(3): 1082-1088.

Weisskoff, R. (1996). "Simple measurement of scanner stability for functional NMR imaging of activation in the brain." Magn. Reson. Med 36(4): 643-645.

Williams, S. M. and P. S. Goldman-Rakic (1998). "Widespread origin of the primate mesofrontal dopamine system." Cerebral Cortex 8(4): 321-345.

Woolf, N. (1991). "Cholinergic systems in mammalian brain and spinal cord." Prog Neurobiol. 37(6): 475-524.

Woolf, N. and L. Butcher (1985). "Cholinergic systems in the rat brain: II. Projections to the interpeduncular nucleus." Brain Res Bull. 14(1): 63-83.

Yelnik, J., C. François, et al. (1987). "Golgi study of the primate substantia nigra. I. Quantitative morphology and typology of nigral neurons." J Comp Neurol 265(4): 455-472.

CHAPTER II

MR OPTIMIZATION FOR EVALUATING THE ANATOMY OF THE HUMAN MIDBRAIN DOPAMINE SYSTEM

Abstract

A number of optimization steps needed to be implemented in order to develop an MR imaging protocol that could accurately capture the anatomy of the midbrain dopaminergic (DA) ventral tegmental area (VTA) and substantia nigra (SN). The current study explored imaging parameters that included MR sequence selection, slice orientation and positioning, spatial voxel resolution, TE (Time to Echo) and CNR (Contrast to Noise Ratio) measurements. Our goal was to achieve superior quality images compared to previous studies, at very high resolution with distinguishable contrast between regions of interest (ROIs) in the midbrain. Two- and three-dimensional pulse sequences were explored because of their ability to provide high T2- and T2*-weighted contrast in the midbrain. Imaging slices were positioned in the axial orientation with an oblique angle tilted towards the occipital cortex. A TE value between 16 - 22 ms was concluded to be optimal based on the combined T2* values of the SN and the VTA. CNR was applied as a quantitative metric to show signal and noise differences between ROIs in the midbrain.

Introduction

Accurately characterizing the anatomical contours of the VTA and SN midbrain structures in humans can be useful for evaluating structural changes associated with neurodegenerative diseases and for localizing blood oxygen level dependent (BOLD) responses in functional magnetic resonance imaging (fMRI) studies. Loss of DA neurons in the SNc is

24

known to be associated with the development of Parkinsonian symptoms (Fearnley and Lees 1991). Moreover, neuroimaging studies in drug addiction (Tomasi, Goldstein et al. 2007), schizophrenia (Takahashi, Koeda et al. 2004) and psychosis (Murray, Corlett et al. 2008) have observed disease related differences in BOLD activity in the VTA/SNc DA region, consistent with models of midbrain DA circuitry dysregulation. Due to the magnetic susceptibility features associated with neuromelanin in mesencephalic structures, SN and the red nucleus (RN), structural changes can be easily visualized and quantified using MR techniques. Successful imaging of the midbrain structures, therefore, has potential application in the detection of specific damage to these areas, enabling a more accurate diagnosis for neurodegenerative disease states.

T1-, T2- and T2*- weighted pulse sequences have been typically employed to study brainstem anatomy, with T1 weighted sequences exhibiting detectable contrast for lower brainstem structures (Sasaki, Shibata et al. 2006). However, T1-weighted proton density pulse sequences were not successful at delineating regions with dense vasculature or for detecting subtle differences in the internal structures within the SN (pars compacta and pars reticulata). T2- and T2*- weighted imaging techniques at 3 T and 4 T have been able to accomplish high resolution anatomical images at 0.5 x 0.5 x 2 mm^3 with contrasts revealing some vascular definition (Semnic, Svetel et al. 2005; Manova, Habib et al. 2009). However, MR at these lower field strengths has not been able to clearly detail the boundaries of mesencephalic SN and VTA regions or detect substructure and microvasculature within these areas. Imaging at higher field strengths (7 T or higher) with higher resolution would enable a more accurate examination of the anatomy of the midbrain regions, given the small size of the SN and the VTA.

Among T2- and T2*- weighted sequences at 7 T, we tested a two-dimensional (2-D) Gradient and Spin Echo (GRASE) and a three-dimensional (3-D) gradient echo Fast Field Echo (FFE) pulse sequences. GRASE is a 2-D T2- and T2*- weighted multi-shot imaging sequence comprised of refocusing pulses coupled with trains of alternating polarity readout gradient lobes to form a series of interleaved spin and gradient echoes (Feinberg and Oshio 1991). This scan

acquires data in two dimensions, with phase encoding in one dimension, and SENSE acceleration (Pruessmann, Weiger et al. 1999) in one dimension. The FFE is a 3-D T2*- weighted multi-shot gradient echo scan, without EPI (echo planar imaging) readout. This scan acquires data in three dimensions, with two phase encoding directions, allowing for SENSE acceleration in two dimensions. The T2* weighting of a sequence makes it more sensitive to magnetic field inhomogeneities, particularly those contributed by iron containing neuromelanin as well as blood vessels dynamics. This is especially pertinent in the midbrain SN and VTA regions.

The present study explored various parameters required to develop an optimal anatomical imaging protocol for the midbrain.

Methods

All the optimization scans were performed on two male participants (mean age = 26.5 years) on a 7 T Achieva Scanner (Philips Healthcare, Cleveland, Ohio). The participants provided written informed consent for the study, which was approved by the Institutional Review board of Vanderbilt University Medical Center.

Slice positioning and orientation

The position of the slices in the brain and its orientation (axial or coronal) was tested to observe visual image quality (contrast sensitivity) and immunity to image distortions, as well as CNRs between structures (Figure 5). In order to achieve the primary goal of attaining very high spatial resolution, we had to image over a smaller area and accommodate reasonable imaging time constraints. The axial orientation was chosen over the coronal orientation so that every slice covering the midbrain would contain both the SN and VTA.
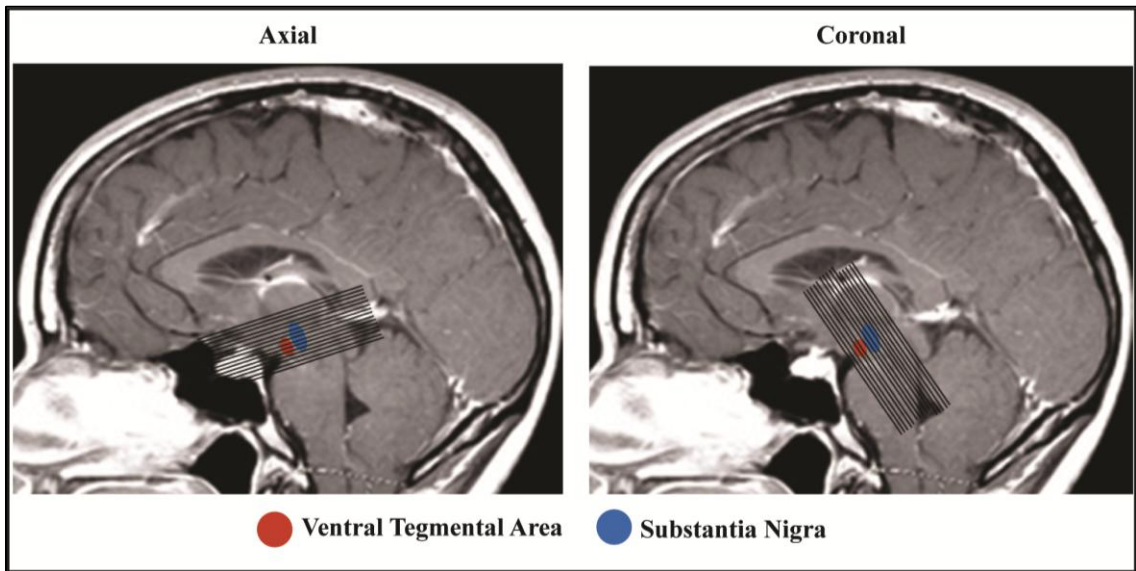
Figure 5: **Slice positioning for anatomical midbrain imaging overlaid on mid sagittal MR images.** The left panel shows slice coverage in the axial plane (horizontal slice slab) and the right panel shows the slice coverage in the coronal plane (vertical slice slab). The VTA and SN are represented as red and blue solid circles respectively underneath the slice stack. **A** denotes the anterior part of the brain.

Spatial voxel resolution

Since prior anatomical imaging studies of the midbrain had attempted sub-millimeter level in-plane spatial resolution, we initiated our study at a voxel resolution consistent with this previously reported level and progressed towards a voxel resolution that provided higher CNR. We began with a 0.4 mm x 0.4 mm in-plane resolution and changed the slice thickness between 2.2 mm, 2 mm and 1 mm. Axial orientations were acquired for all three slice thickness sections. The coronal orientation was only acquired for the 2.2 mm section in the FFE and 1 mm section in the GRASE.

2-D GRASE sequence imaging parameters

For a 0.4 x 0.4 x 2 mm axial section, the scanning parameters included the following: slice gap = 0 mm, number of slices = 14, FOV = 128 (AP) x 102.4 (RL) x 28 mm (FH) with fold-over suppression, reconstruction matrix size = 320 x 256, TR = 5000 ms, TE = 22 ms, FA = 90°, parallel imaging factor, SENSE = 2 in the RL direction, turbo spin-echo factor= 4, EPI factor = 3, and acquisition time = 11 min 20 s. Within this time, 2 volumes were reconstructed, each with NEX = 3.

For a 0.4 x 0.4 x 1 mm axial section, the scanning parameters included the following: slice gap = 0.1mm, number of slices = 20, FOV = 128 (AP) x 102.4 (RL) x 20 mm (FH) with fold-over suppression, reconstruction matrix size = 320 x 256, TR = 5000 ms, TE = 24 ms, FA = 90°, parallel imaging factor, SENSE = 2 in the RL direction, turbo spin-echo factor= 4, EPI factor = 3, and acquisition time = 11 min 20 s. Within this time, 2 volumes were reconstructed, each with NEX = 3.

3-D FFE sequence imaging parameters

For a 0.4 x 0.4 x 2 mm axial section, the scanning parameters included the following: number of slices = 14, FOV = 128 (AP) x 104 (RL) x 28 mm (FH) with fold-over suppression,

reconstruction matrix size = 320 x 260, TR = 25 ms, TE = 18 ms, FA = 15°, parallel imaging

factor, SENSE = 2 in the RL direction and parallel imaging factor, SENSE = 1 in the AP

direction, and acquisition time = 5 min 44.3 s. Within this time, 2 volumes were reconstructed,

each with NEX = 3.

For a 0.4 x 0.4 x 1 mm axial section, the scanning parameters included the following:

number of slices = 20, FOV = 128 (AP) x 104 (RL) x 20 mm (FH) with fold-over suppression,

reconstruction matrix size = 320 x 260, TR = 25 ms, TE = 18 ms, FA = 15°, parallel imaging

factor, SENSE = 2 in the RL direction and parallel imaging factor, SENSE = 1 in the FH

direction, and acquisition time = 8 min 18.1 s. Within this time, 2 volumes were reconstructed,

each with NEX = 3.

A pencil beam volume shim was implemented in all scan sequences (Gruetter and Boesch

1992; Gruetter 1993).

Optimum TE

The optimum TE was investigated using a multi-echo scan sequence and a T2* map of

the midbrain. This sequence acquired images of the midbrain at 6 ms intervals beginning at 4.6 s

and ending at 28.6 s. We plotted the CNR between the midbrain ROIs with respect to the

different TEs, and this plot displayed the range of TEs that provided the highest CNR. Using the

T2* map, we drew ROIs in the midbrain to determine the mean T2* values in the midbrain

structures of interest. The T2* value also provided an indication of the optimal TE range for the

scans (Menon, Ogawa et al. 1993).

For the multi-echo scan, the voxel resolution was 0.4 x 0.4 x 2.2 mm, axial orientation

and the scanning parameters included the following: number of slices = 12, FOV = 128 (AP) x

104 (RL) x 26.4 mm (FH) with fold-over suppression, reconstruction matrix size = 320 x 260, TR

= 39 ms, TE1 = 4.6 ms, delta TE = 6 s, 5 echoes, FA = 10°, parallel imaging factor, SENSE = 2 in

the RL direction and SENSE factor = 1 in the FH direction, and acquisition time = 5 min and 5 s. Within this time, 2 volumes were reconstructed, each with NEX = 2.

CNR calculations

For GRASE and FFE scans, contrast measurements were calculated by taking the average of 2 volumes and measuring the signal intensity for a given structure by manually tracing out the volume of the structure in 2 dimensions within the averaged image. This calculation was performed across all the imaging sections. CNR was calculated as the signal-intensity difference between 2 structures divided by the noise. Noise was calculated by subtracting 1 image volume from the other and computing the pooled SD of the signal intensity in the 2 structures within the difference image. This process helped control for SENSE reconstruction artifacts. The calculation of the average and difference images assumed no significant head movement by the participant between the acquisitions of each imaging volume.

Results

A representative group of scans performed are reported in this section. The signal and noise intensity measurements were made over two slices that covered the midbrain region. Both coronal and axial orientations exhibited similar visual contrast sensitivity for the midbrain areas, however, only the axial scans are reported in this study. The GRASE scans displayed a distinct outline of the entire midbrain, and more specifically the iron containing SN and RN (Figure 6).

	ROI	Mean	SD
🔵	RN	2.8 0e+03	182.51
🔴	SN	3.05e+03	155.98
🟠	VTA	5.26e+03	221.13
🟢	WM	4.38e+03	143.53

CNR Measurements	SN/VTA	SN/RN	SN/WM		VTA/RN	VTA/WM		RN/WM
GRASE Slice8	11.25	1.35	7.01		13.75	4.65		9.06
GRASE Slice9	11.58	1.15	7.44		13.14	4.29		7.82

A = Anterior, P = Posterior
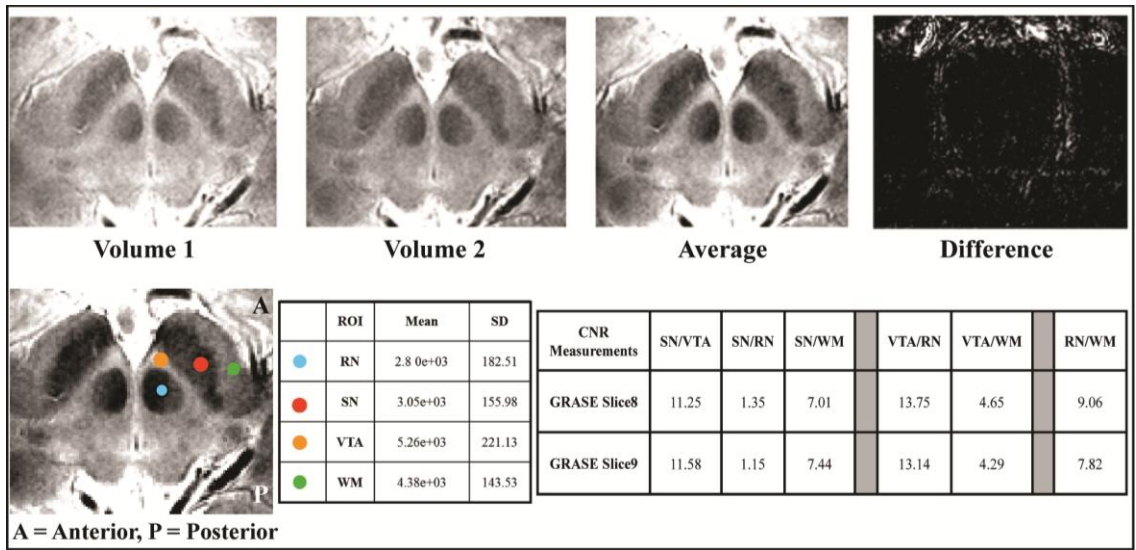
Figure 6: **Axial view of a 2-D GRASE scan at 0.4 x 0.4 x 2 mm^3.** Panel **A** shows the different imaging volumes acquired and the average and difference images created from those volumes. In panel **B**, section a) shows the location where the regions of interest (ROIs) were drawn on the average image, section b) shows the mean signal and standard deviation (SD) in the ROIs, and section c) shows the CNR measurements between different ROIs in the midbrain.

31

The 0.4 x 0.4 x 1 mm voxel resolution in the GRASE scans also displayed contrast sensitivity, however the image exhibited greater noise relative to the scan with the greater slice thickness (Figure 7). The CNR of this scan between midbrain regions was also lower compared to the 0.4 x 0.4 x 2 mm scan.
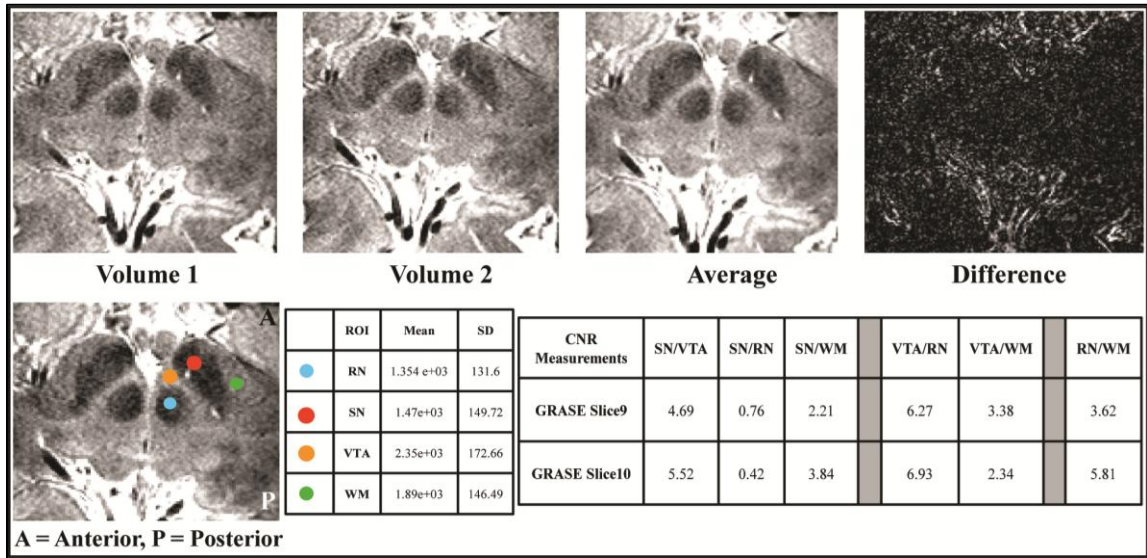
Figure 7: **Axial view of a 2-D GRASE scan at 0.4 x 0.4 x 1 mm³.** Panel **A** shows the different imaging volumes acquired and the average and difference images created from those volumes. In panel **B**, section a) shows the location where the regions of interest (ROIs) were drawn on the average image, section b) shows the mean signal and standard deviation (SD) in the ROIs, and section c) shows the CNR measurements between different ROIs in the midbrain.

Similar to GRASE scans, the FFE scans highlighted remarkable contrast in the midbrain areas, and demonstrated higher sensitivity towards vasculature surrounding the midbrain (Figure 8).
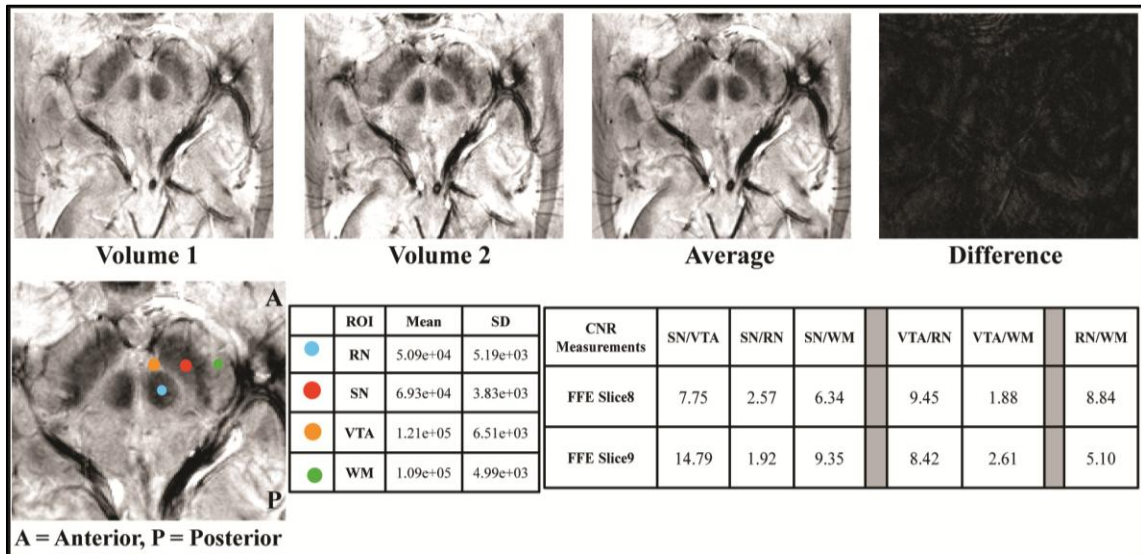
Figure 8: **Axial view of a 3-D FFE scan at 0.4 x 0.4 x 2 mm^3.** Panel **A** shows the different imaging volumes acquired and the average and difference images created from those volumes. In panel **B**, section a) shows the location where the regions of interest (ROIs) were drawn on the average image, section b) shows the mean signal and standard deviation (SD) in the ROIs, and section c) shows the CNR measurements between different ROIs in the midbrain.

The visual quality of the images in the higher resolution (0.4 x 0.4 x 1 mm) FFE scans appeared noisier and had lower CNR compared to the 0.4 x 0.4 x 2 mm voxel scans (Figure 9).
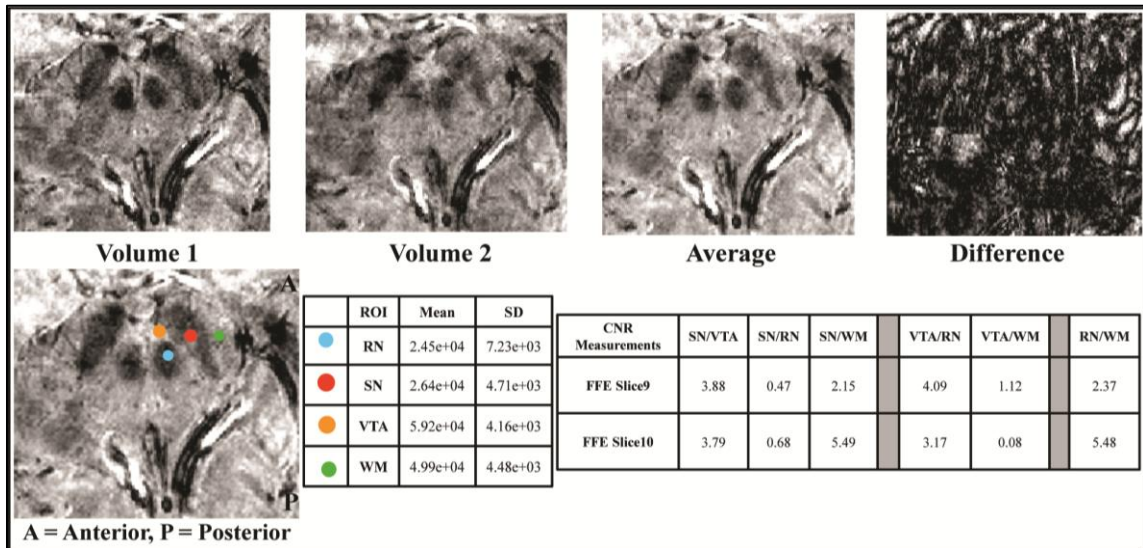
Figure 9: **Axial view of a 3-D FFE scan at 0.4 x 0.4 x 1 mm^3.** Panel **A** shows the different imaging volumes acquired and the average and difference images created from those volumes. In panel **B**, section a) shows the location where the regions of interest (ROIs) were drawn on the average image, section b) shows the mean signal and standard deviation (SD) in the ROIs, and section c) shows the CNR measurements between different ROIs in the midbrain.

Based on the multi-echo scan, the optimal TE range for imaging the midbrain area was determined to be between 16-22 ms (Figure 10). The multi-echo scan also generated a T2* map of the imaging volume. The T2* map was used to draw ROIs in the midbrain and calculate the mean T2* for the SN, VTA and other brain areas. The mean and standard deviation (SD) T2* values in one participant were: SN = 14.0 ms, SD = 2.2 ms; VTA = 28.9 ms SD = 5.3 ms; red nucleus = 16.3 ms SD = 1.6 ms; cortical gray matter = 41.8, SD = 5.3 ms; cortical white matter = 25.3 ms, SD = 2.2 ms.
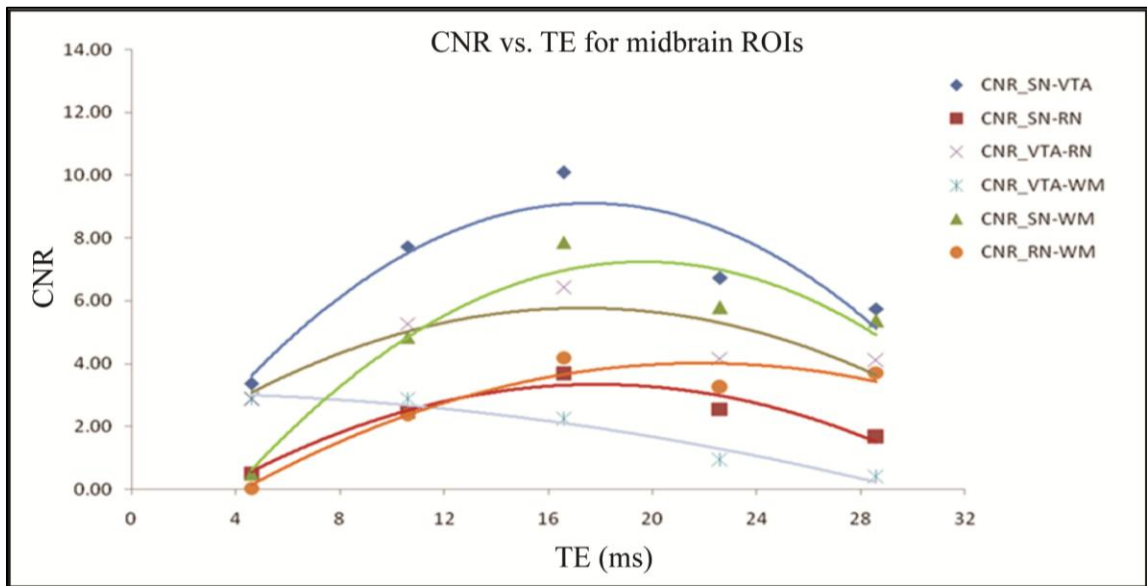
Figure 10: **CNR vs. TE for various midbrain regions of interest.** Peak TE for imaging the SN and VTA is between 16-22 ms. Legend indicates CNR between different midbrain regions. These regions include: **SN** (substantia nigra), **VTA** (ventral tegmental area), **RN** (red nucleus) and **WM** (white matter, cerebral peduncles). Lines represent the line of best fit for each CNR combination.

Discussion

This study aimed to explore the effects of various MR parameters on the quality of anatomical images obtained for the midbrain. The main criteria for choosing these parameters included the visual quality of the images (minimal distortions), contrast sensitivity between ROIs (SN, VTA and neighboring landmarks), the level of anatomical detail that could be clearly visualized, and the signal intensity and the noise levels as measured by the CNR between ROIs. These criteria were achieved by experimenting with two different pulse sequences that provided T2 and T2* contrast. In these two sequences, we assessed the optimum slice positioning and orientation of the imaging slab, established an optimal voxel resolution and TE, and measured signal intensity and noise levels in the midbrain regions.

Since T1 images did not provide a strong contrast between midbrain ROIs, we explored two T2- and T2*- weighted pulse sequences for our imaging purpose. Both GRASE and FFE scans revealed noticeable contrast sensitivity for the midbrain areas. The GRASE sequence, because of its T2 and T2* weighting, exhibited excellent detail outlining the midbrain as well as the iron rich SN and RN. The FFE scan, though not ideal for outlining the overall midbrain, displayed particular sensitivity to vasculature within the midbrain, as well as in areas surrounding the midbrain (because of its T2* weighting).

In both scans, we could clearly delineate the boundaries of midbrain SN and RN and this information was important for identifying the location of the adjacent VTA. Tracing the boundaries of the SN and VTA will aid in the calculation of accurate volume measurements and in obtaining more reliable size estimates of these areas, supplementing the use of a standard atlas. Moreover, segmenting these anatomical regions will be beneficial in future functional MRI studies for precisely localizing task-related BOLD activations in the midbrain.

Only the axial scans were reported in this study because we could see the SN and the VTA in every imaging slice. In the coronal sections, we noticed that some anterior slices did not

40

contain the SN, and some posterior slices did not contain the VTA. Therefore, if there was any imaging variation between slices, it would not be observed equally in both the SN and VTA. Imaging variations could affect the signal intensity calculations, resulting in inaccurate CNR measurements between the SN and VTA. In the axial orientation, on the other hand, both the SN and the VTA could be visualized in the same slice, thereby reducing differences in imaging variations between these regions.

A voxel resolution of 0.4 x 0.4 x 2 mm proved to be the most reliable and stable in terms of visualization quality, contrast sensitivity and CNR measurements for the scan time selected. The higher voxel resolution of 0.4 x 0.4 x 1 mm was qualitatively noisier and had lower CNR measurements between the SN and the VTA, as expected.

As mentioned in the introduction, the CNR measurements were performed by drawing ROIs in the average image (to calculate the mean signal) and in the difference image (to calculate the noise). The calculation of the average and difference images assumed no significant head movement by the participant between the acquisitions of each volume. In drawing these ROIs, our goal was to choose areas that had homogeneous signal intensity throughout the imaging volume. In the relevant literature, noise measurements are made by drawing an ROI in an area of least signal inhomogeneity. Typically, this area is the background of the image (outside the skull) or a region within the white matter. Homogeneity of the signal intensity is affected by spatial variation of signal intensity associated with SENSE image reconstruction. This means that signal intensity toward the outside of the brain may differ from that detected inside the brain. This spatial variation is more evident at higher SENSE factors, thereby influencing overall noise measurements. In our study, which used SENSE reconstruction in the imaging protocol, the signal intensity also varied across the image. Although we tested noise measurements in the background image, as well as in the white matter in both GRASE and FFE scans (results not shown here), we decided against using those methods in the CNR calculations. We instead used

41

the pooled standard deviation within the midbrain ROIs as our noise calculation in order to avoid complications with signal intensity differences within the image.

The T2* values of the midbrain demonstrated almost a factor of two difference between the SN and the VTA. Thus choosing an optimal TE value was difficult because the TE is shown to be optimal if it is chosen to be similar to the T2* value of the structure of interest (Menon, Ogawa et al. 1993). According to the CNR vs. TE map, an optimum TE range for the midbrain SN and VTA fell between 16-22 ms. A TE of 22 ms was chosen for the GRASE scans in order to meet all the other imaging criteria and reach a spatial resolution of 0.4 x 0.4 x 2 mm. On the other hand, a TE of 18 ms was chosen for the FFE scan in order to achieve the 0.4 x 0.4 x 2 mm voxel resolution. Both these scans with their respective imaging parameters provided the best results in terms of visual image quality, contrast sensitivity and measureable CNR.

Conclusion

In conclusion, our study successfully isolated key imaging parameters necessary to optimally image the anatomical midbrain dopaminergic system. The T2 and T2* weighting of the GRASE and FFE scans were particularly enhanced in the midbrain region due to the magnetic susceptibility associated with the iron rich SN and RN. An oblique axial slice slab with an optimal spatial resolution of 0.4 x 0.4 x 2 mm along with a TE range between 16- 22 ms was established as a reliable standard for anatomical imaging of the midbrain at 7 T. Future studies can confirm these findings by reproducing them in multiple participants.

References

Fearnley, J. M. and A. J. Lees (1991). "Ageing and Parkinson's disease: substantia nigra regional selectivity." Brain **114**: 2283-2301.

Feinberg, D. A. and K. Oshio (1991). "GRASE (gradient- and spin-echo) MR imaging: a new fast clinical imaging technique." Radiology **181**(2): 597-602.

Gruetter, R. (1993). "Automatic, localized in vivo adjustment of all first- and second-order shim coils." Magn Reson Med. **29**(6): 804-811.

Gruetter, R. and C. Boesch (1992). "Fast, Noniterative Shimming of Spatially Localized Signals. In Vivo Analysis of the Magnetic Field along Axes." Journal of Magnetic Resonance **96**(323-334): 323.

Manova, E. S., C. A. Habib, et al. (2009). "Characterizing the Mesencephalon Using Susceptibility-Weighted Imaging." American Journal of Neurobiology **30**: 569-574.

Menon, R. S., S. Ogawa, et al. (1993). "4 Tesla Gradient Recalled Echo Characteristics of Photic S timulation-Induced Signal Changes in the HumanPrimary Visual Cortex." Magn Reson Med **30**(3): 380-386.

Murray, G., P. Corlett, et al. (2008). "Substantia nigra/ventral tegmental reward prediction error disruption in psychosis." Molecular Psychiatry **13**: 267-276.

Pruessmann, K., M. Weiger, et al. (1999). "SENSE: sensitivity encoding for fast MRI." Magn Reson Med. **42**(5): 952-962.

Sasaki, M., E. Shibata, et al. (2006). "Neuromelanin magnetic resonance imaging of locus ceruleus and substantia nigra in Parkinson's disease." Neuroreport **17**(11): 1215-1218.

Semnic, R., M. Svetel, et al. (2005). "Magnetic resonance imaging morphometry of the midbrain in patients with Wilson disease." J Comput Assist Tomogr. **29**(6): 880-883.

Takahashi, H., M. Koeda, et al. (2004). "An fMRI study of differential neural response to affective pictures in schizophrenia." NeuroImage **22**(3): 1247-1254.

Tomasi, D., R. Z. Goldstein, et al. (2007). "Widespread disruption in brain activation patterns to a working memory task during cocaine abstinence." Brain Research **1171**: 83-92.

CHAPTER III

ANATOMICAL IMAGING OF THE HUMAN MIDBRAIN DOPAMINE SYSTEM

Abstract

Dysfunction of dopamine (DA) neurotransmission from the midbrain substantia nigra (SN) and ventral tegmental area (VTA) has been implicated in various neuropsychiatric illnesses, including Parkinson disease and schizophrenia. Unfortunately, most clinical MR imaging protocols cannot identify or define these midbrain DA structures accurately. To more precisely evaluate the anatomic architecture of the DA midbrain, we scanned ten healthy participants on two different MRI pulse sequences at 7 T. We contrasted the performance of high-resolution 2-D T2- and T2*-weighted GRadient and Spin Echo (GRASE) with 3-D T2*- weighted Fast Field Echo (FFE) MR imaging scans across participants. Contrast to noise ratios (CNR) were calculated among the SN, VTA, and the red nucleus (RN). Volumetric assessments of these midbrain regions were estimated by using a segmentation algorithm. Both GRASE and FFE sequences revealed visible contrast between midbrain DA regions. The GRASE scan revealed higher CNRs compared to the FFE scan. The T2* contrast of the FFE scan further delineated substructures and microvasculature within the midbrain SN and RN. Segmentation and volume estimation of the midbrain SN, RN, and VTA revealed individual differences in the size and volume of these structures across participants. GRASE and FFE were both reliable MR sequences that provided sufficient CNR to evaluate the anatomy of the midbrain DA system. The FFE in particular revealed vascular details and additional substructure information within the midbrain regions that could be potentially useful for examining structural changes in midbrain pathologies.

Introduction

The midbrain DA neurotransmitter system is primarily housed within the substantia nigra pars compacta (SNc) and the VTA and DA neurons from these two areas are known to project to a broad range of cortical and subcortical brain regions (Oades and GM. 1987; Yelnik, François et al. 1987; Williams and Goldman-Rakic 1998). Additionally, these neurons have unique firing properties (Grace and Bunney 1984) known to be associated with a variety of behaviors (in rodents and non-human primates) including reward related learning (Schultz and Romo 1990), motivation (Salamone 1996; Ikemoto and Panksepp 1999), attention (Redgrave, Prescott et al. 1999), novelty processing (Kakade and Dayan 2002), and other goal-directed functions (Schultz 1998). While these in vivo studies in rodents and non-human primates provide a framework for understanding the role of the VTA and the SNc, the finer, distinct, and individual functions of these midbrain nuclei in mediating behavior, especially in humans and in disease states, are still to be fully understood. Accurately identifying the anatomy of midbrain DA regions in humans can be important for isolating structural changes associated with midbrain pathologies. Loss of DA neurons in the SNc is known to play a causal role in the development of Parkinsonian symptoms (Fearnley and Lees 1991). Furthermore, neuroimaging studies in drug addiction (Tomasi, Goldstein et al. 2007), schizophrenia (Takahashi, Koeda et al. 2004), and psychosis (Murray, Corlett et al. 2008) have reported disease-related differences in blood oxygen level dependent (BOLD) activity in the VTA/SNc DA region, consistent with models of midbrain DA circuitry dysregulation.

Most MR imaging studies involving the brainstem to date have been conducted in scanners operating at 1.5 T (Duguid, Paz et al. 1986), 3 T (Shibata, Sasaki et al. 2008; Snyder and Connor 2008), or 4 T (Manova, Habib et al. 2009) with imaging protocols that have limited resolution, contrast sensitivity, and signal to noise ratios (SNRs). However, at higher field strengths (7 T), some of these limitations can be addressed because higher SNR allows the use of

smaller voxel dimensions, and susceptibility contrast effects increase with increasing field strengths. To the extent that the midbrain SN and VTA areas can be delineated, it is also possible to measure volumetric changes in these regions in normal and disease states. Moreover, the magnetic susceptibility associated with neuromelanin, ferritin, and other iron bearing compounds (Zecca, Berg et al. 2005) in mesencephalic structures (e.g., the SN), allows changes in iron deposits of these structures to be visualized and quantified. Such a finding would be specifically relevant for clinical studies since levels of neuromelanin, iron, and ferritin all change during aging and Parkinson disease (Sofic, Riederer et al. 1988; Connor and Menzies 1995; Zecca, Gallorini et al. 2001). Successfully imaging the midbrain structures may thus be useful for the detection and accurate diagnoses of neurodegenerative disease pertaining to these regions.

T1-, T2-, and T2*-weighted pulse sequences have each been used to study midbrain anatomy, with T1-weighted sequences exhibiting detectable contrast for lower midbrain structures (Sasaki, Shibata et al. 2006). However, neither T1-weighted nor proton density weighted imaging sequences have been able to delineate areas with different levels of vascularization within the RN or detect subregions of the SN (pars compacta and pars reticulata). T2- andT2*-weighted imaging techniques at 3 T and 4 T have been able to obtain high resolution anatomic images at 0.5 x 0.5 x 2 mm^3 in reasonable imaging times with contrast revealing some vascular definition (Semnic, Svetel et al. 2005; Manova, Habib et al. 2009). However, MR imaging at these lower field strengths has typically been limited in its ability to accurately detail boundaries or detect the substructure and microvasculature of mesencephalic regions.

The current study aimed at evaluating the ability of high field (7 T) MR imaging to scan the anatomic architecture of the midbrain DA regions across multiple participants. This was accomplished by using T2- and T2*-weighted pulse sequences, including GRASE and FFE. GRASE (Feinberg and Oshio 1991) is a T2- and T2*-weighted multi-shot imaging sequence comprising refocusing pulses coupled with trains of alternating polarity readout gradient lobes to form a series of interleaved spin and gradient echoes. This scan acquires data in 2 dimensions,

with phase-encoding in one direction, allowing for SENSE acceleration (Pruessmann, Weiger et al. 1999) in one dimension. The FFE (Bernstein, King et al. 2004) is a T2*-weighted multi-shot gradient-echo scan that acquires data in 3 dimensions. These sequences were chosen on the basis of considerations of imaging time, contrast sensitivity, and relative immunity to image distortions that can arise at high fields (as elaborated in Chapter II). Using GRASE and FFE sequences, we obtained high-resolution images of the midbrain to detect visible susceptibility differences in the SN, VTA, and RN across participants. Additionally, we evaluated the ability of these sequences to observe substructure anatomy and vascular detail in the midbrain. Quantitative assessments of CNR between different midbrain regions were also computed. Additionally, a segmentation algorithm (Li, Kao et al. 2008) was used to segment the SN, VTA, and RN in order to create labeled volume maps and to estimate volumes of these midbrain regions across participants.

Methods

Ten healthy volunteers, 20–40 years of age (7 men), were imaged on a 7 T Achieva Scanner (Philips Healthcare, Cleveland, Ohio) by using both GRASE and FFE pulse sequences. All participants provided written informed consent for the study, which was approved by the institutional review board of Vanderbilt University Medical Center. Images were acquired in an oblique axial orientation with 14 sections positioned to cover the dorso-ventral extent of the midbrain from the inferior edge of the basal ganglia to the dorsal border of the pons. The axial sections were tilted to make them parallel to a plane bisecting the mammillary body and the superior colliculi (Figure 11).
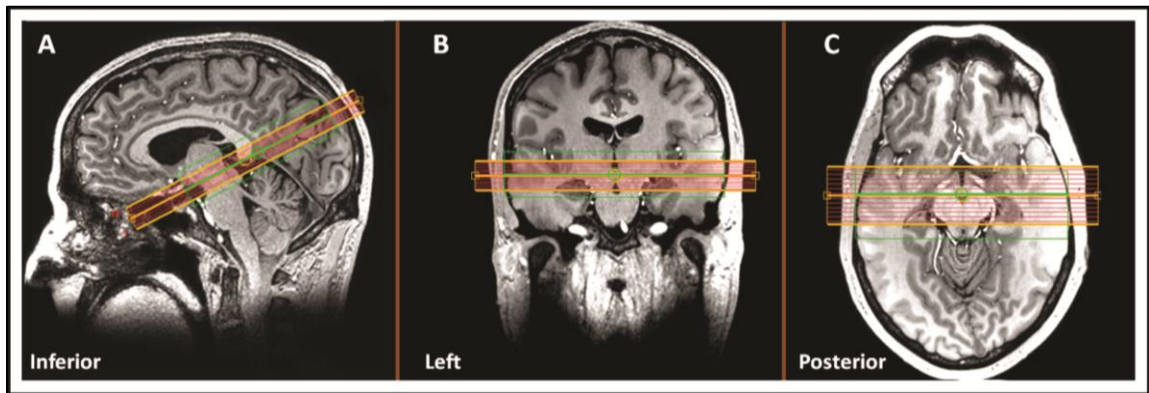
Figure 11: **Section geometry for anatomic imaging of the midbrain region.** Fourteen oblique axial sections are positioned to cover the dorso-ventral extent of the midbrain; they were parallel to a plane bisecting the mammillary body and the superior colliculi. **A**, The sagittal plane. **B**, The coronal plane. **C**, The axial plane. The yellow-orange bounding box represents the slice slab and the smaller green box represents the shim volume.

Imaging Protocol at 7 T

After initial exploration of different sequence parameters (detailed in Chapter II), two different pulse sequences were employed to image the anatomy of the midbrain. A flow-compensated 2-D GRASE sequence was performed with a 0.4 x 0.4 mm in-plane resolution, a 2-mm section thickness, and a 0-mm section gap. Other scanning parameters included the following: FOV = 128 (AP) x 102 (RL) x 28 mm (FH) with fold-over suppression, reconstruction matrix size = 320 x 256, TR = 5000 ms, TE =22 ms, FA = 79°, parallel imaging factor, SENSE = 2 in the RL direction, turbo spin-echo factor = 4, EPI factor =3, and scan duration = 11 min 12 s. Within this time, 2 volumes were reconstructed, each with NEX = 3.

The FFE sequence was also flow-compensated, obtained at a resolution of 0.4 x 0.4mmin-plane with 2-mm section thickness. Other scanning parameters included the following: FOV = 128 (AP) x 102 (RL) x 28 mm (FH) with fold-over suppression, reconstruction matrix size = 320 x 256, TR = 25 ms, TE = 18 ms, FA = 15°, parallel imaging factor, SENSE = 2 in the RL direction, and scan duration = 5 min 26 s. Again, 2 complete volumes, each with NEX = 3, were obtained. A pencil beam volume shim was used in both scan sequences (Gruetter and Boesch 1992; Gruetter 1993).

Data Analysis

The data were processed by using Matlab (version R2010a, MathWorks, Natick, Massachusetts), and statistical tests were performed by using the Statistical Package for the Social Sciences, Version 18.0 (SPSS, Chicago, Illinois). Window-level-setting adjustments were made to view the best image contrast within the midbrain. To clearly visualize the different midbrain structures and improve image quality, we averaged the 2 volumes for each scan type together.

CNR Measurements

For GRASE and FFE scans, contrast measurements were calculated by taking the average of 2 volumes and measuring the signal intensity for a given structure by manually tracing out the volume of the structure in 2 dimensions. This calculation was performed across all the imaging sections. CNR was calculated as the signal-intensity difference between 2 structures divided by the noise. Noise was calculated by subtracting 1 image volume from the other and computing the pooled standard deviation (SD) of the signal intensity in the 2 structures within the difference image. This process helped control for SENSE reconstruction artifacts. The calculation of the average and difference images assumes that the participants did not move their heads between the acquisitions of each volume.

Segmentation

A region-growing segmentation algorithm (Li, Kao et al. 2008) was used to trace out the boundaries of the midbrain structures. This algorithm used the average image (produced from the 2 volumes) for every section, normalized the signal intensity values to account for magnetic field inhomogeneities, and traced the contours of the tissue/structure by comparing the signal-intensity changes from one voxel to the next. All voxels above a certain intensity threshold were counted as part of one structure, and after 300 iterations of such intensity-threshold comparisons, the boundary of the structure is traced. This method worked very effectively for the SN and the RN, both of which had a sharp contrast between their boundaries and neighboring regions, presumably due to the signal-intensity loss associated with the magnetic susceptibility produced by iron products within their cells.

The SN was chosen from the inferior axial section, just above the pons where the interpeduncular fossa opens up to the interpeduncular cistern. The most superior axial section containing the SN includes a small portion of the posterior commissure, with the posterior boundary marked by the cerebral aqueduct and the anterior boundary defined by the mammillary

50

bodies. The SN runs into the subthalamic nucleus in its dorsal boundary, so we used an atlas

(Naidich, Duvernoy et al. 2009) to visually guide the contours of the SN in the superior sections.

We marked the SN in every section going in the superior direction until the axial sections did not

include the superior colliculi or the cerebral aqueduct. The subthalamic nucleus becomes

prominent when viewed in the axial plane that includes the third ventricle, RN, and posterior

commissure with no superior colliculi.

The area of the VTA was manually traced and approximated in each section by localizing

its boundaries with respect to neighboring regions as guided by atlases (Paxinos and Huang 1995;

Naidich, Duvernoy et al. 2009). Similar to the SN, the VTA was chosen from inferior axial

sections, just above the pons, where the interpeduncular fossa opens up to the interpeduncular

cistern. In these inferior sections, the boundaries of the VTA were defined with the lateral portion

adjacent to the SN, and the medial portion adjacent to the interpeduncular fossa, abutting the

ventral part of the superior cerebellar decussation and the interpeduncular nucleus. More

superiorly, the VTA becomes a contiguous structure, with its lateral boundary still adjacent to the

SN, and its medial boundary approaching the midline, apposing the interpeduncular fossa and

extending in the posterior direction half way up the medial edge of the RN. This posterior

boundary is a topographic landmark because the VTA lacks clear demarcation along the midline.

The superior most axial section that contains the VTA includes a small portion of the posterior

commissure, with the posterior boundary defined by the cerebral aqueduct and the anterior

boundary defined by the mammillary bodies. The RN was chosen in all the sections that exhibited

a visible contrast for this structure through the inferior-superior plane of axis. This region was

traced as a control region to clearly distinguish and highlight the boundaries of the SN and VTA.

The segmentation algorithm was implemented across every section to produce a 3-D-labeled

volume map of the SN, VTA, and RN. The lateral sides of each structure were traced, resulting in

a total of six structures for every participant (left SN, left VTA, left RN, right SN, right VTA, and

the right RN), and this provided an estimate of the variation in the structure across the left and

right sides. All the sections were visually inspected by overlaying the segmented maps onto the original anatomic image to ensure accuracy of overlap and successful segmentation.

Volume Measurement

Once the segmentation procedure was completed, the algorithm computed the number of voxels included within the segmented area in every section for every region of interest (ROI). The number of voxels was then multiplied by the size of each voxel (0.4 x 0.4 x 2 mm) to compute the volume of each structure in cubic millimeters.

Volume Normalization

To control for inter-subject variability in midbrain size, we normalized each participant's volume of interest (SN, VTA, RN) to the entire midbrain volume. The midbrain volume was estimated by segmenting the entire midbrain in the GRASE scan for every section that included the segmented SN, VTA, or RN. We used this midbrain normalization rather than whole-brain normalization because it allowed specific consideration of the extent to which the three structures of interest make up the midbrain region.

<center>**Results**</center>

Visible Contrast in Midbrain Regions

GRASE and FFE scans both revealed visible contrast in the midbrain, with anatomic detail exhibiting close concordance to that observed in histology (Figure 12). The densely and poorly vascularized regions of the RN were distinctly visible in both the GRASE and FFE scans (Figures 12B, 12C and Figure 13). Additionally, minute vascular contrast was evident in the FFE scan for small blood vessels within the SN (Figure 12C). The FFE scan also displayed distinct

<center>52</center>

contrast for internal divisions within the SN (pars compacta versus reticulata) exhibiting

sensitivity to iron-related magnetic susceptibilities (Figure 13).

A= Anterior, P = Posterior, PCA = Posterior Cerebral Artery
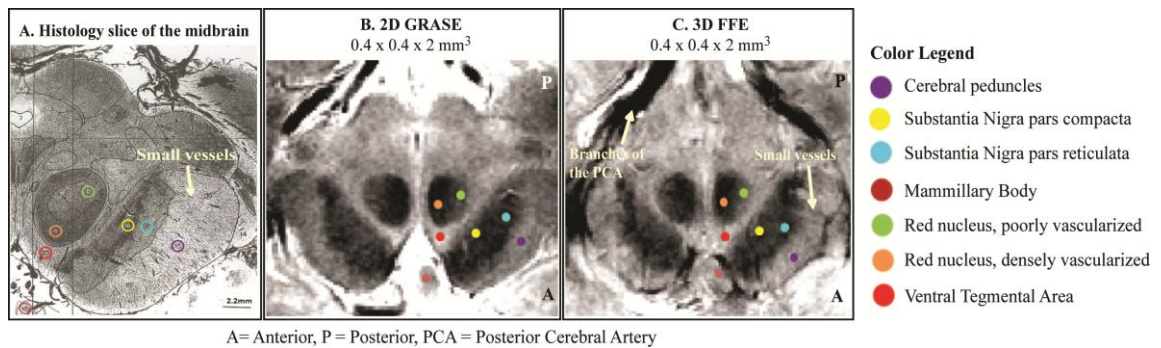
Figure 12: **GRASE and FFE scans in a single participant next to a histology slice of the midbrain.** The sections are chosen at the level of the superior colliculus. **A)** Histology slice of the midbrain (stained using India ink to highlight vasculature), reprinted with kind permission from Springer Science+Business Media: *Human Brain Stem Vessels*, from chapter, Mesencephelon, 2nd ed. Berlin, Germany: Springer-Verlag; 1999, page 207, Duvernoy HM, Figure 149 (Duvernoy 1999). **B)** GRASE image of the midbrain. **C)** FFE image of the midbrain. The slices are oriented so that the anterior part of the midbrain appears at the bottom of the slices. Legend indicates the location of the midbrain structures marked with respect to a brain atlas (Duvernoy 1999). **A** denotes the anterior part of the brain and **P** denotes the posterior part of the brain.
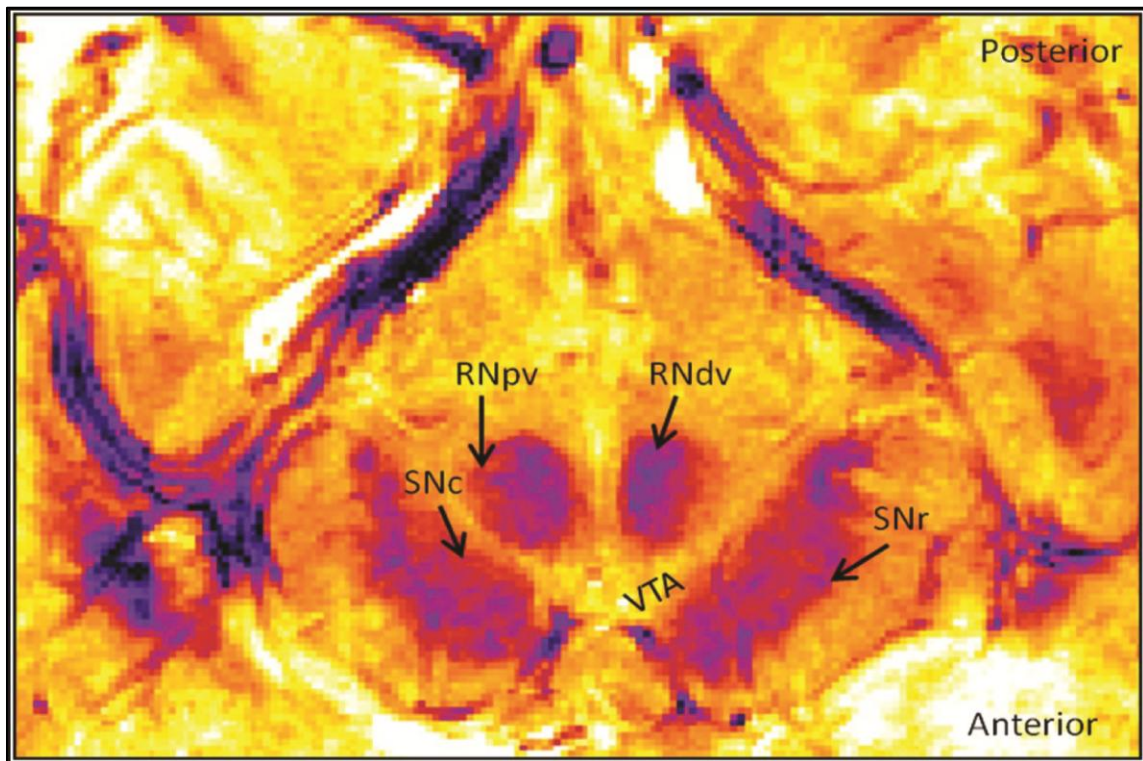
Figure 13: **FFE image in one slice of the midbrain highlighting substructure detail.** The image from a single participant was passed through a look-up table filter to produce a color contrast scale. Different parts of the red nucleus and the substantia nigra are revealed. **SNc** = Substantia Nigra pars compacta, **SNr** = Substantia Nigra pars reticulata, **VTA** = Ventral Tegmental Area, **RNdv** = Red Nucleus densely vascularized section and **RNpv** = Red Nucleus poorly vascularized section.

CNR Measurements

CNR is a standard way to quantify signal intensity values between tissues and we wanted to verify how these values compared to those previously reported in lower field strength studies (Manova, Habib et al. 2009). Across the 10 subjects, GRASE and FFE scans displayed detectable contrast between midbrain regions (Table 1). When we compared across subjects, the CNRs from the 2 scan types were not strongly correlated. The Pearson correlation coefficient of CNR values between the 2 different scan types was $r = 0.47$ for SN/VTA, $r = -0.46$ for the SN/RN, and $r = 0.21$ for the RN/VTA (all $p > 0.10$).

Table 1: **Mean CNR values for GRASE and FFE scans in different midbrain regions.** Values averaged across 10 participants.

Scan Type	GRASE	GRASE	GRASE	FFE	FFE	FFE
Region	SN/VTA	SN/RN	RN/VTA	SN/VTA	SN/RN	RN/VTA
Mean	5.250	0.830	7.854	4.251	0.995	4.800
Standard Deviation	1.010	0.540	1.040	2.231	1.191	1.873

CNR differences between the 2 scans varied depending on the specific ratio in question. No differences were observed across the GRASE and FFE scans between the SN and VTA, and the SN and the RN (both, Wilcoxon signed rank test, $p > 0.1$). However the CNR difference in the RN/VTA was significant across the 2 scans (Wilcoxon signed rank test, $z = -2.70$, $p = 0.007$). Additionally, a section-by-section comparison of the CNR values revealed inter-section variability across subjects (Figure 14).
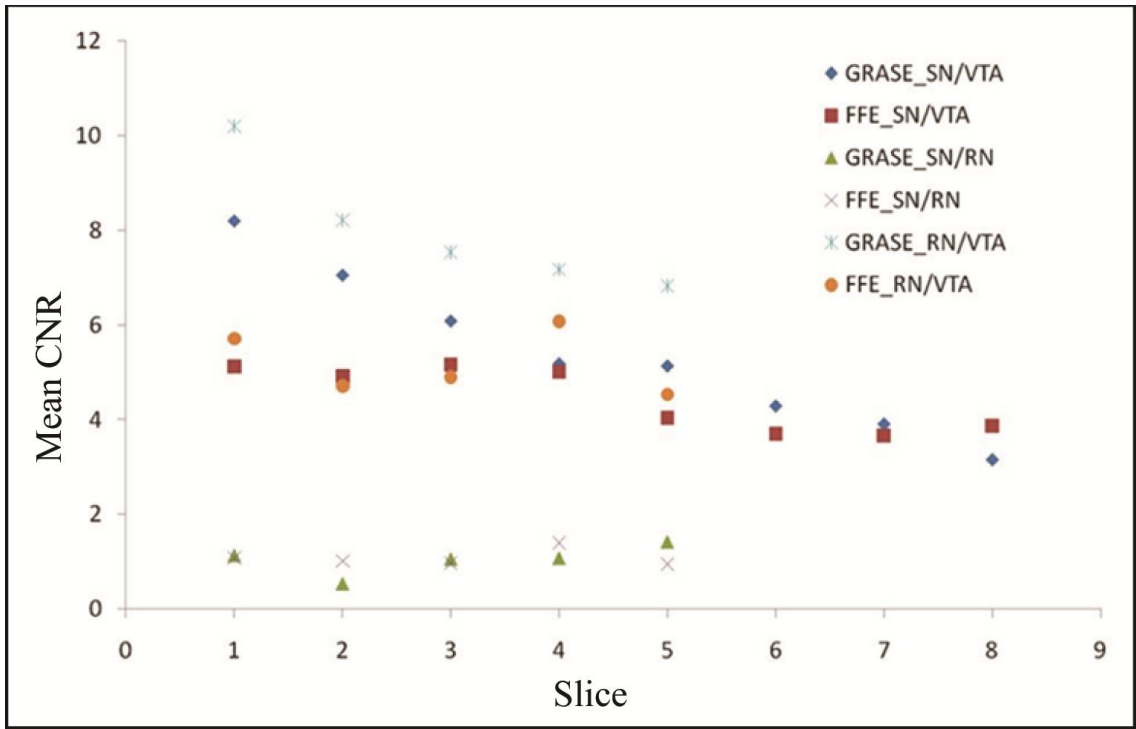
Figure 14: **Section-by-section representation of the mean CNR values for different midbrain regions of interest for GRASE and FFE scans.** Only 8 slice sections are shown here because they best represent the midbrain regions considered in this study. Midbrain regions of interest shown here include: SN = substantia nigra, VTA = ventral tegmental area and RN = red nucleus. N = 10.

Segmentation and Volume Measurements

The segmentation algorithm traced the midbrain regions in both the GRASE and FFE scans (Figures 15 and 16). The area identified by the algorithm corresponded to all visually observable boundaries.
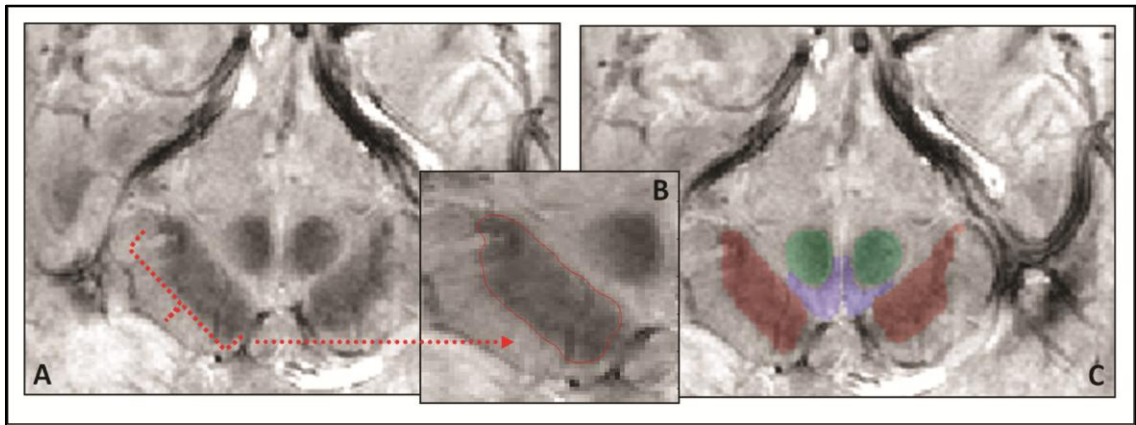
Figure 15: **Segmentation process using a region-growing segmentation algorithm.** The FFE scan of one individual is shown here. **A**, Sample section in the midbrain at the level of the mammillary bodies in which the segmentation algorithm was implemented. **B**, Segmented region of the SN traced in red within the midbrain. **C**, Segmented structures (SN is red; VTA, blue; and RN, green) overlaid on the anatomic FFE image.
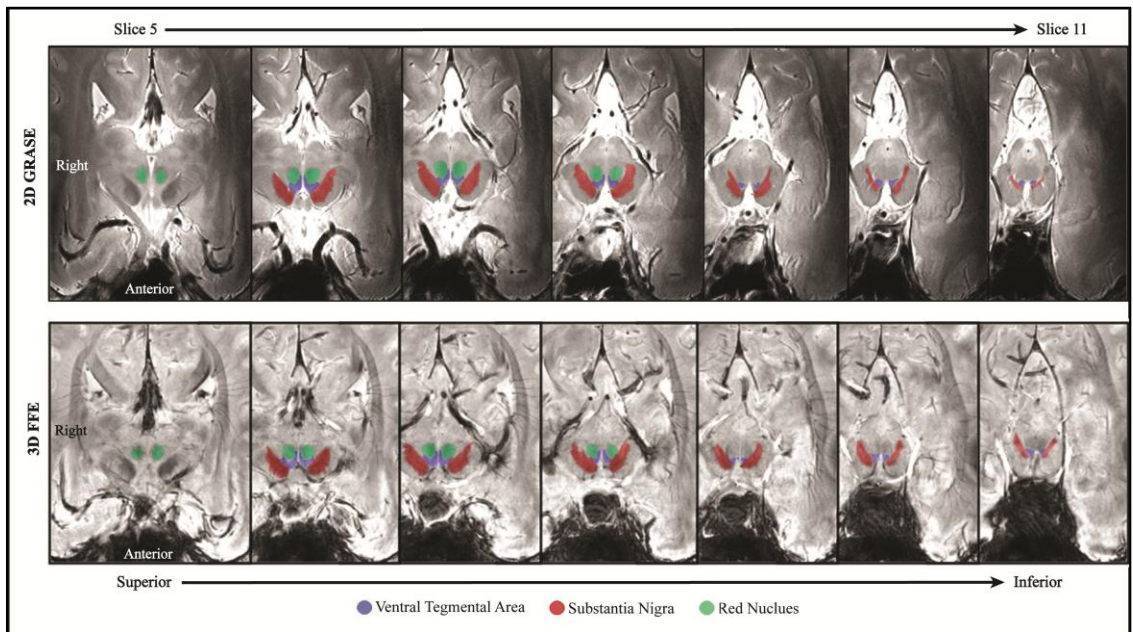
Figure 16: **Segmentation results across midbrain sections.** Results for GRASE (**A**) and FFE (**B**) scans in a single participant. Segmented volumes are shown from the superior through inferior axial planes.

From the segmented images, the volumes of different midbrain regions were computed (Table 2 and Fig 17). The GRASE and FFE scans revealed high correlation between the volumes of the midbrain regions (Pearson correlation coefficient for GRASE and FFE scans of the SN, $r = 0.93$; VTA, $r = 0.87$; and RN, $r = 0.96$ (all $p < 0.001$). Additionally, the GRASE and FFE volume results were not significantly different from each other (Wilcoxon signed rank test for the VTA, $z = -0.97$, $p = 0.33$; for the RN, $z = -1.07$, $p = 0.29$), though there was a modest trend for higher volumes by using the FFE over the GRASE sequence for the SN ($z = -1.68$, $p = 0.09$).

Table 2: **Mean absolute and normalized volume estimates from GRASE and FFE scans in the SN, VTA and RN.** Values averaged across 10 participants.

Scan Type	GRASE	GRASE	GRASE		FFE	FFE	FFE
Location	SN	VTA	RN		SN	VTA	RN
Mean Absolute Volume (in mm³)	725.7	154.4	215.6		753.1	159.9	213.0
Standard Deviation of Absolute Volume (in mm³)	98.37	23.81	43.23		106.5	29.72	40.16
Mean Normalized Volume	0.085	0.018	0.048		0.089	0.019	0.047
Standard Deviation of Normalized Volume	0.009	0.002	0.004		0.012	0.003	0.007
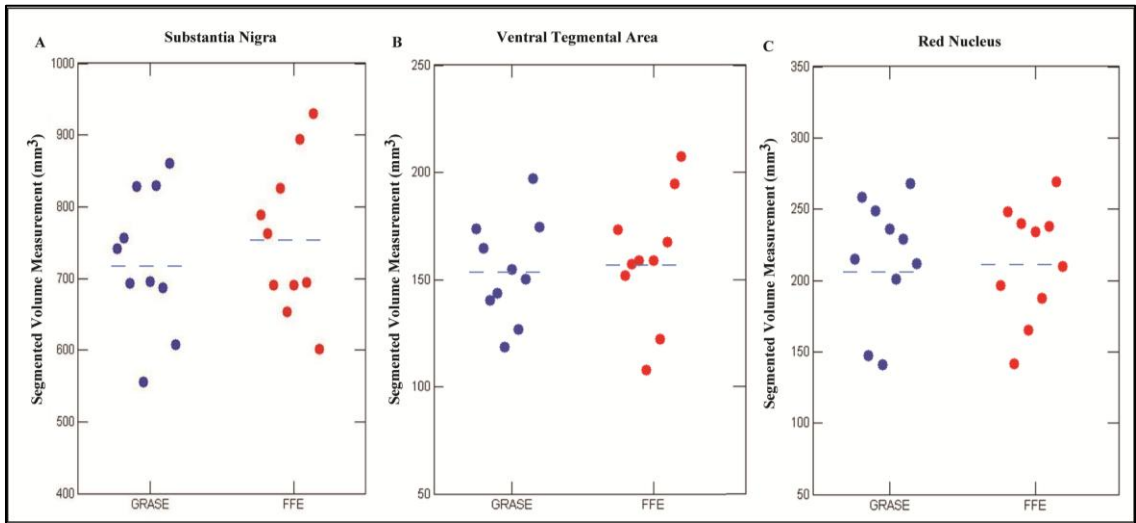
Figure 17: **Individual participant absolute volume measurements in the midbrain.** ROIs represent the Substantia Nigra (Panel A), Ventral Tegmental Area (Panel B) and the Red Nucleus (Panel C). Volume measurements for ten participants are shown here; blue dots represent the GRASE scan and red dots represent the FFE scan. Dashed line represents mean volume.

The volumes of the RN, SN, and VTA were normalized with respect to the midbrain volume to control for variability in the dimensions of structures in the midbrain across participants (Table 2 and Figure 18). The GRASE and FFE scans again revealed high correlation between the volumes of the midbrain regions (SN, r = 0.92; VTA, r = 0.81; and RN, r = 0.89; all, $p \leq 0.005$). Additionally, the GRASE and FFE volume results were not significantly different from each other (all Wilcoxon signed rank test, $p > 0.10$).

Volume results described above were averaged across the 2 sides to control for laterality differences. When laterality was taken into consideration, the SN and RN did not show a significant difference between volumes in the left and right sides (all Wilcoxon signed rank test, $p > 0.10$). In contrast, the VTA volume revealed a significant difference between the left and right sides in both the GRASE and FFE scans (GRASE, Wilcoxon signed rank test, z = -2.70, p = 0.007; FFE, Wilcoxon signed rank test, z = -1.99, p = 0.047).
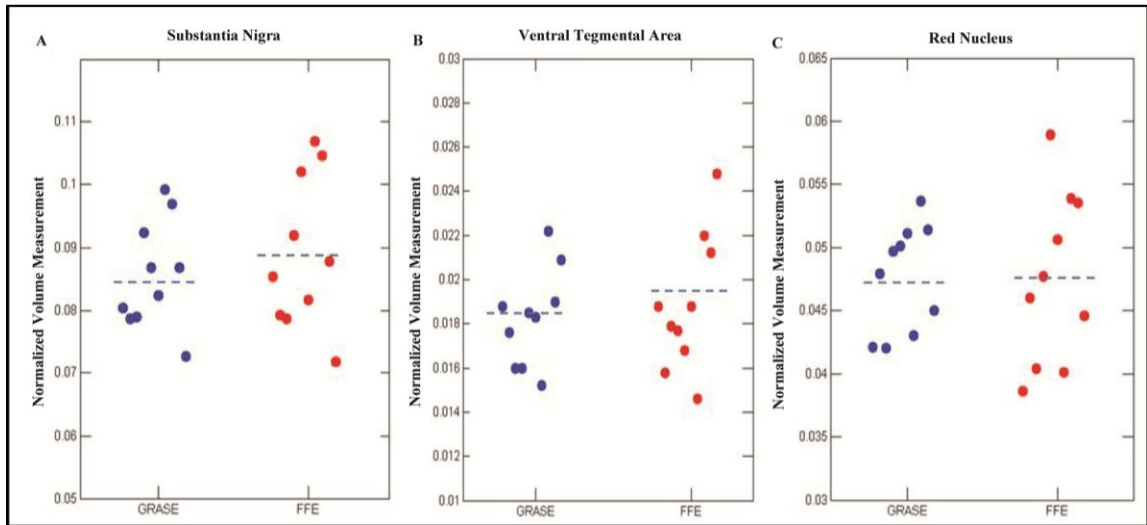
Figure 18: **Individual participant normalized volume measurements in the midbrain.** ROIs represent the Substantia Nigra (**A**), Ventral Tegmental Area (**B**), and the Red Nucleus (**C**). Volume measurements for 10 participants are shown here. Blue dots represent the GRASE scan; red dots represent the FFE scan. The dashed line represents mean volume.

<center>**Discussion**</center>

Anatomic Delineation Achieved at 7 T

Our present study results indicated that both GRASE and FFE scans provided excellent anatomic detail in the midbrain, revealing close concordance to known histology of the midbrain (Figure 12). The mixed T2- and T2*-weighting of the GRASE scan distinctly delineated the boundaries of the midbrain area, highlighting iron-rich areas within the SN and RN. The T2*-weighting of the FFE scan was also comparable with the GRASE scan for detecting visible contrast among structures within the midbrain.

Vessel- related contrast was observed in both scans. This was markedly visible within the RN, where differing MR signal intensities were evidenced between the medial and lateral areas, corresponding to the densely and poorly vascularized portions respectively. These subregions of the RN observed in our study match similar areas in the midbrain histologic section stained for vasculature (Figure 12, B). Additionally, the vascular contrasts observed within the RN corroborate previous work shown using susceptibility weighted imaging (SWI) in the midbrain at 4 T (Manova, Habib et al. 2009). The T2*-weighting of the FFE scan additionally detected subtle microvascular details, particularly small blood vessels emanating from the SN complex and traveling perpendicular toward the cerebral peduncles (Figure 12,C). These comprise multiple arteries and veins belonging to the internal anterolateral group of mesencephalic vessels, crossing through the cerebral peduncles at right angles to the peduncles (Duvernoy 1999). This degree of vascular definition can useful in clinical settings for the diagnoses of vascular infarcts or ischemia in the midbrain or other brain areas connected to the midbrain.

The T2*-weighting in both the GRASE and FFE scans, in particular the latter, enabled the detection of signal-intensity variations within different parts of the SN, namely the SN pars compacta, SNc, and the SN pars reticulata, SNr (Figure 13). The SNr is known to have higher iron content compared with the SNc, which has been shown to correlate with decreased signal

<center>65</center>

intensity (associated with decreased T2 relaxation times) (Drayer, Burger et al. 1986). The SNc contains more neuromelanin than the SNr (Braak and Braak 1986; Yelnik, François et al. 1987), and iron can be stored in neuromelanin by the iron-storage protein ferritin (Zecca, Pietra et al. 1994; Double, Gerlach et al. 2003). Iron perturbs the magnetic field uniformity in tissues and causes MR signal intensity within tissues to decrease (Drayer, Burger et al. 1986; Rutledge, Hilal et al. 1987; Tosk, Holshouser et al. 1992). Hence, the MR imaging related signal intensity effects observed in the SN could be attributed to the paramagnetic neuromelanin or intracellular iron stores. Within the FFE scans, we observed a characteristic signal-intensity demarcation in the SN complex, with a relatively hyper-intense band framing the SNc and a relatively hypo-intense band framing the SNr (Figure 12, C). Attempting to achieve this level of delineation in the SN has only been previously reported with T2-weighted imaging sequences at 1.5 T (Duguid, Paz et al. 1986) and even in that study, the resolution was not sufficient to explain clear differences between the SN subdivisions.

The color-coded image of the midbrain in the FFE scan (Figure 13) displayed visible signal-intensity effects in the SN. This visual distinction in signal intensity, observed across sections in multiple individuals may represent the boundary of the SNc and SNr. However, the reliability of the divide and its relation to the actual boundaries of the SNc remains uncertain. Identifying a clear delineation of the boundary between these two SN structures in humans through the use of MR remains a controversial matter. Manova and colleagues (Manova, Habib et al. 2009) point to a possible divide in the SN by using SWI without articulating the specific susceptibility difference in the two structures or providing details on the criteria for defining this divide. T1-weighted neuromelanin-sensitive scans (Sasaki, Shibata et al. 2006; Shibata, Sasaki et al. 2008) have also been used to localize the SNc, without describing the boundary between the SNc and the SNr or discussing how the iron in the SNr may contribute to T1 shortening or lengthening effects (Tosk, Holshouser et al. 1992).

Other studies reported decreased signal intensity in their T2-weighted images, making reference only to the reticulata in their identification of the SN (Drayer, Burger et al. 1986). On the basis of signal intensity, a report attributed the medial hypo-intense region to the SNr and the lateral higher signal intensity area to the SNc (Drayer, Olanow et al. 1986). Additional studies used an approach that appeared to capture the intermediate area between the nigra and RN, rather than merely the nigra (Duguid, Paz et al. 1986; Braffman, Grossman et al. 1989; Martin, Wieler et al. 2008). These findings collectively imply that establishing clearly defined, reliable boundaries between the SN compacta and reticulata has yet to be demonstrated in the literature. Comparison of postmortem samples and establishment of inter-rater reliability of the SNc and SNr volumes would be useful for verifying the boundaries of these substructures in future research.

Clinical Implications of Understanding the Anatomy of the Midbrain

Characterizing the anatomic architecture of the SN has important clinical implications. This understanding is of particular relevance in diagnosing Parkinson's disease, in which there is a known loss of DA neurons in the SNc (Fearnley and Lees 1991) and an increase in iron deposition within the SN (Dexter, Carayon et al. 1991). The source of MR imaging signal-intensity changes in Parkinson disease is not fully understood. Studies have shown a reduction in the width of the SNc, arising from an increase in iron content within the SNr or loss of DA neurons in the SNc (Duguid, Paz et al. 1986). In MR imaging, these structural changes have been associated with a "smudging" of the SNr hypo-intensity along with decreased distance between the RN and the SN (Drayer 1988). Other studies have shown T2-weighted hyper-intense signal intensity within the SNr or a loss of the hypo-intense signal intensity within this area (Braffman, Grossman et al. 1989; Stern, Braffman et al. 1989).

The region-based segmentation algorithm used in the present study provides a means of quantifying the dimensions and distance between various midbrain brain structures, especially at

high voxel resolutions. This technique can be further used to trace tissue-related structural changes occurring longitudinally in midbrain pathologies. T2 relaxation time provides another marker for measuring disease-related structural changes within the SN (Ordidge, Gorell et al. 1994). R2' measurements in the SN at 3 T have been shown to correlate with simple motor scores in Parkinson disease (Gorell, Ordidge et al. 1995). Susceptibility contrast effects increase with increasing field strengths. Therefore, MR images taken using FFE and GRASE sequences, as seen in the present study at 7 T, should be particularly sensitive to the subtle T2- and T2*-weighted changes observed within the SN anatomy in neurodegenerative diseases.

Quantitative measurements using CNR and volume segmentation

The CNR measurements taken between different regions of the midbrain revealed that the CNR of the GRASE scans was slightly higher than that of the FFE scans (Table 1), though the scanning time was also longer. The CNR values achieved in the present study are higher than those reported by previous imaging studies of the mesencephalon at 4 T (Manova, Habib et al. 2009), demonstrating greater sensitivity to detecting variations in tissues at higher field strengths. Variability in the mean CNR values across subjects for various sections was also observed, suggesting region-specific differences in signal intensity and noise measurements. Volume measurements of the SN, VTA, and RN revealed individual differences, indicating variability based on the size of the structure, even after correcting for the overall size of the participant's midbrain.

While we did not observe laterality differences for the SN and RN, volume differences were observed across the left and right VTA in both the GRASE and FFE scans. Unlike the SN and the RN, the VTA does not have any MR imaging- specific contrast that would aid in its detection. Thus, the boundaries of the VTA were manually defined by using anatomic reference points based on existing atlases (Paxinos and Huang 1995; Naidich, Duvernoy et al. 2009). The positions of some of these reference points (e.g., the interpeduncular fossa) were estimated on the

basis of the detectability of boundaries arising in the specific scan sequence. While the GRASE sequence clearly delineated the overall boundaries of the midbrain, these boundaries were less apparent in the FFE scan, contributing to the variation of volumes when defining the VTA region. Within neuroimaging research, knowledge of midbrain boundaries can be beneficial for localizing BOLD responses in fMRI experiments of the midbrain. Due to imaging resolution limitations, most prior fMRI studies have not shown distinct and reliable BOLD activity in the SN and VTA for tasks thought to invoke DA release (Bunzeck and Duzel 2006; D'Ardenne, McClure et al. 2008). Defining the precise boundaries of different midbrain regions can also be useful for localizing seed regions in functional connectivity maps within the brainstem.

Higher field strength imaging has various technical challenges, especially when imaging the midbrain. These challenges include signal-intensity artifacts and distortions caused by large-scale magnetic susceptibility variations in the brain as well as the behavior of radio frequency coils at high fields. The scan sequences described in the current work handle some of these technical challenges. In the future, developing more uniform B1 magnetic fields, increasing the sensitivity of parallel imaging by using a higher number of coil elements, and optimizing scan sequences specifically for the brainstem may prove to be beneficial for imaging the midbrain. High-pass filtered phase images taken using SWI appear particularly promising at 4 T, exhibiting susceptibility contrast that may be capable of distinguishing different parts of the SN (Manova, Habib et al. 2009). In preliminary studies with SWI at 7 T, we have observed some evidence of enhanced distinction between the SNc and SNr. We also discovered, however, phase-related aliasing at the boundary of the midbrain and the interpeduncular fossa (tissue-CSF interface). In addition, CNR values in the high pass filtered phase images were lower for the SN in comparison to those observed in the magnitude images of FFE and GRASE scans. Future studies at 7 T in which optimized SWI data are combined with GRASE or FFE scans may provide further improvements in accurately delineating midbrain substructures.

Conclusion

We successfully imaged the midbrain SN and VTA in ten healthy humans, and were able to delineate detailed anatomy to a degree otherwise not achievable at lower MR field strengths. The signal-intensity sensitivity was calculated using CNRs, and volume was estimated by segmenting individual midbrain structures. The results from this study not only further our understanding of the fine-grained anatomic architecture of the midbrain, but also point to potential clinical applications for neuropsychiatric diseases in which there are known structural changes related to this area of the brain.

References

Bernstein, M., K. King, et al., Eds. (2004). Handbook of MRI Pulse Sequences. San Diego, California, Elsevier Academic Press.

Braak, H. and E. Braak (1986). "Nuclear configuration and neuronal types of the nucleus niger in the brain of the human adult." Hum Neurobiol. 5(2): 71-82.

Braffman, B. H., R. I. Grossman, et al. (1989). "MR imaging of Parkinson disease with spin-echo and gradient-echo sequences." American Journal of Roentgenology 152(1): 159-165.

Bunzeck, N. and E. Duzel (2006). "Absolute Coding of Stimulus Novelty in the Human Substantia Nigra/VTA." Neuron 51(3): 369-379.

Connor, J. R. and S. L. Menzies (1995). "Cellular management of iron in the brain." J Neurol Sci 134: 33-44.

D'Ardenne, K., S. M. McClure, et al. (2008). "BOLD Responses Reflecting Dopaminergic Signals in the Human Ventral Tegmental Area." Science 319(5867): 1264-1267.

Dexter, D. T., A. Carayon, et al. (1991). "Alterations in the levels of iron, ferritin and other trace metals in Parkinson's disease and other neurodegenerative diseases affecting the basal ganglia." Brain 114(4): 1953-1975.

Double, K., M. Gerlach, et al. (2003). "Iron-binding characteristics of neuromelanin of the human substantia nigra." Biochem Pharmacol. 66(3): 489-494.

Drayer, B., P. Burger, et al. (1986). "MRI of brain iron." American Journal of Roentgenology 147(1): 103-110.

Drayer, B., W. Olanow, et al. (1986). "Parkinson plus syndrome: diagnosis using high field MR imaging of brain iron." Radiology 159(2): 493-498.

Drayer, B. P. (1988). "Imaging of the aging brain. Part II. Pathologic conditions." Radiology 166(3): 797-806.

Duguid, J., R. D. L. Paz, et al. (1986). "Magnetic resonance imaging of the midbrain in Parkinson's disease." Annals of Neurology 20(6): 744-747.

Duvernoy, H. M. (1999). Human Brain Stem Vessels: Including the Pineal Gland and Information on Brain Stem Infarction. Berlin, Springer-Verlag.

Fearnley, J. M. and A. J. Lees (1991). "Ageing and Parkinson's disease: substantia nigra regional selectivity." Brain 114: 2283-2301.

Feinberg, D. A. and K. Oshio (1991). "GRASE (gradient- and spin-echo) MR imaging: a new fast clinical imaging technique." Radiology 181(2): 597-602.

Gorell, J., R. Ordidge, et al. (1995). "Increased iron-related MRI contrast in the substantia nigra in Parkinson's disease." Neurology 45(6): 1138-1143.

Grace, A. A. and B. S. Bunney (1984). "The Control of Firiing Pattern in Nigral Dopamine Neurons: Burst Firing." The Journal of Neuroscience 4(11): 2877-2890.

Gruetter, R. (1993). "Automatic, localized in vivo adjustment of all first- and second-order shim coils." Magn Reson Med. **29**(6): 804-811.

Gruetter, R. and C. Boesch (1992). "Fast, Noniterative Shimming of Spatially Localized Signals. In Vivo Analysis of the Magnetic Field along Axes." Journal of Magnetic Resonance **96**(323-334): 323.

Ikemoto, S. and J. Panksepp (1999). "The role of nucleus accumbens dopamine in motivated behavior: a unifying interpretation with special reference to reward-seeking." Brain Research Reviews 31(1): 6–41.

Kakade, S. and P. Dayan (2002). "Dopamine: generalization and bonuses." <u>Neural Networks</u> 15: 549-559.

Li, C., C.-Y. Kao, et al. (2008). "Minimization of Region-Scalable Fitting Energy for Image Segmentation." <u>IEEE Transactions On Image Processing</u> 17(10): 1940-1949.

Manova, E. S., C. A. Habib, et al. (2009). "Characterizing the Mesencephalon Using Susceptibility-Weighted Imaging." <u>American Journal of Neurobiology</u> 30: 569-574.

Martin, W., M. Wieler, et al. (2008). "Midbrain iron content in early Parkinson disease: a potential biomarker of disease status." <u>Neurology</u> 70(16 Pt2): 1411-1417.

Murray, G., P. Corlett, et al. (2008). "Substantia nigra/ventral tegmental reward prediction error disruption in psychosis." <u>Molecular Psychiatry</u> 13: 267-276.

Naidich, T. P., H. M. Duvernoy, et al. (2009). <u>Duvernoy's Atlas of the Human Brain Stem and Cerebellum: High-Field MRI, Surface Anatomy, Internal Structure, Vascularization and 3 D Sectional Anatomy.</u> New York, Springer-Verlag Wien.

Oades, R. and G. H. GM. (1987). "Ventral tegmental (A10) system: neurobiology. 1. Anatomy and connectivity." <u>Brain Research</u> 434(2): 117-165.

Ordidge, R., J. Gorell, et al. (1994). "Assessment of relative brain iron concentrations using T2-weighted and T2*-weighted MRI at 3 Tesla." <u>Magnetic Resonance in Medicine</u> 32(3): 335-341.

Paxinos, G. and X.-F. Huang, Eds. (1995). <u>Atlas of the Human Brainstem</u>. San Diego, Academic Press.

Pruessmann, K., M. Weiger, et al. (1999). "SENSE: sensitivity encoding for fast MRI." <u>Magn Reson Med.</u> **42**(5): 952-962.

Redgrave, P., T. J. Prescott, et al. (1999). "Is the short-latency dopamine response too short to signal reward error?" <u>Trends in Neurosciences</u> 22(4): 146-151.

Rutledge, J. N., S. K. Hilal, et al. (1987). "Study of movement disorders and brain iron by MR." <u>American Journal of Roentgenology</u> 149(2): 365-379.

Salamone, J. D. (1996). "The behavioral neurochemistry of motivation: methodological and conceptual issues in studies of the dynamic activity of nucleus accumbens dopamine." Journal of Neuroscience Methods 64(2): 137-149.

Sasaki, M., E. Shibata, et al. (2006). "Neuromelanin magnetic resonance imaging of locus ceruleus and substantia nigra in Parkinson's disease." Neuroreport 17(11): 1215-1218.

Schultz, W. (1998). "Predictive Reward Signal of Dopamine Neurons." Journal of Neurophysiology 80: 1-27.

Schultz, W. and R. Romo (1990). "Dopamine Neurons of the Monkey Midbrain: Contingencies of Responses to Stimuli Eliciting Immediate Behavioral Reactions." Journal of Neurophysiology 63(3): 607-624.

Semnic, R., M. Svetel, et al. (2005). "Magnetic resonance imaging morphometry of the midbrain in patients with Wilson disease." J Comput Assist Tomogr. 29(6): 880-883.

Shibata, E., M. Sasaki, et al. (2008). "Use of Neuromelanin-Sensitive MRI to distinguish Schizophrenic and Depressive Patients and Healthy Individuals Based on Signal Alterations in the Substantia Nigra and Locus Ceruleus." Biological Psychiatry 64: 401-406.

Snyder, A. M. and J. R. Connor (2008). "Iron, the substantia nigra and related neurological disorders." Biochimica et Biophysica Acta 1790(7): 606-614.

Sofic, E., P. Riederer, et al. (1988). "Increased iron (III) and total iron content in post mortem substantia nigra of parkinsonian brain." J Neural Transm. 74(3): 199-205.

Stern, M., B. Braffman, et al. (1989). "Magnetic resonance imaging in Parkinson's disease and parkinsonian syndromes." Neurology 39(11): 1524-1526.

Takahashi, H., M. Koeda, et al. (2004). "An fMRI study of differential neural response to affective pictures in schizophrenia." NeuroImage 22(3): 1247-1254.

Tomasi, D., R. Z. Goldstein, et al. (2007). "Widespread disruption in brain activation patterns to a working memory task during cocaine abstinence." Brain Research 1171: 83-92.

Tosk, J., B. Holshouser, et al. (1992). "Effects of the interaction between ferric iron and L-dopa melanin on T1 and T2 relaxation times determined by magnetic resonance imaging." Magnetic Resonance in Medicine 26(1): 40-45.

Williams, S. M. and P. S. Goldman-Rakic (1998). "Widespread origin of the primate mesofrontal dopamine system." Cerebral Cortex 8(4): 321-345.

Yelnik, J., C. François, et al. (1987). "Golgi study of the primate substantia nigra. I. Quantitative morphology and typology of nigral neurons." J Comp Neurol 265(4): 455-472.

Zecca, L., D. Berg, et al. (2005). "In Vivo Detection of Iron and Neuromelanin by Transcranial Sonography: A New Approach for Early Detection of Substantia Nigra Damage." Movement Disorders 20(10): 1278-1285.

Zecca, L., M. Gallorini, et al. (2001). "Iron, neuromelanin and ferritin content in the substantia nigra of normal subjects at different ages: consequences for iron storage and neurodegenerative processes." Journal of Neurochemistry 76(6): 1766-1773.

Zecca, L., R. Pietra, et al. (1994). "Iron and other metals in neuromelanin, substantia nigra, and putamen of human brain." J Neurochem. 62(3): 1097-1101.

CHAPTER IV

MR OPTIMIZATION FOR EVALUATING FUNCTION IN THE HUMAN MIDBRIAN DOPAMINE SYSTEM

Abstract

In this study, various imaging parameters and post-processing steps were tested to create a standardized protocol for performing functional imaging of the midbrain dopamine (DA) system. The feasibility of different 7 T MR pulse sequences, including two-dimensional (2-D) single-shot echo planar imaging (EPI) and three-dimensional (3-D) multi-shot gradient echo Fast Field Echo (FFE) sequences were explored. We assessed differences in image quality by manipulating the voxel resolution, volume acquisition times and parallel imaging factor (or SENSE factor). Temporal signal to noise ratios (TSNR) were measured in the midbrain substantia nigra (SN) and ventral tegmental area (VTA) in an effort to quantify differences between the imaging variables used. A noise correction algorithm, RETROICOR, was employed as a post-processing step to determine the efficacy of regressing out variance associated with physiological noise sources (cardiac pulsatility and respiration). In addition, we performed a retrospective cardiac-gated scan to quantify the degree of bulk motion in the brainstem during a cardiac cycle. The 3-D FFE scans produced fewer distortions and higher TSNR in the midbrain than the 2-D EPI scans. A voxel resolution of 1.33 mm^3, volume acquisition time of 2.0 s and a SENSE factor between 3-4 (3.1 for FFE and 4 for EPI in the right-left plane) was determined to be optimum for imaging the midbrain in both sequences. RETROICOR was able to correct for noise related to physiological factors, however, its ability to effectively remove the influence of these noise sources in the midbrain was limited. From the retrospective cardiac gated scan, brainstem motion was determined to be most prominent in the inferior and anterior directions. However, the overall

displacement of the midbrain ROIs was less than 5% of a voxel volume, suggesting that motion associated with cardiac pulsatility did not significantly contribute to the noise in the midbrain.

Introduction

As described in Chapter I, due to likely limitations in imaging protocols, functional magnetic resonance imaging (fMRI) studies at lower field strengths have been unable to convincingly show distinct and differential blood oxygen level dependent (BOLD) responses in the midbrain SN and VTA region. Before exploring BOLD responses associated with a task, we first tested and developed a functional imaging protocol that would be capable of optimally imaging the midbrain at 7 T. Differences in visual contrast and TSNR measurements were estimated for different pulse sequences by manipulating the voxel resolution, volume acquisition times and SENSE factors.

MRI pulse sequences used for fMRI

Standard single-shot 2-D gradient echo Echo Planar Imaging (EPI) sequences have been conventionally used for acquiring fMRI data at 1.5 T and 3 T scanners (Mansfield, Coxon et al. 1994; Duyn, Yang et al. 1996). This fast imaging sequence allows for full brain coverage with an acquisition time of ~2 s and has been shown to produce reliable and reproducible signal both cortically and subcortically at lower field strengths. However, at higher field strengths (7 T and higher), there are drawbacks to using this approach, especially within the brainstem. EPI imaging sequences suffers from susceptibility artifacts, distortion and signal drop out at the interfaces of bone, tissue and air. Even with the use of parallel imaging techniques (SENSE (Pruessmann, Weiger et al. 1999)), 2-D EPI is unable to reliably acquire functional imaging data in areas with strong magnetic susceptibility gradients. Within the midbrain, magnetic field inhomogeneities can be severe due to the proximity of the VTA and SN to the interpeduncular fossa (IPF), an area

through which cerebrospinal fluid (CSF) flows. Additionally, the 2-D data acquisition allows SENSE to be implemented only in one phase encoding direction.

3-D gradient echo Fast Field Echo (FFE) MR sequences have been shown to reduce distortions produced as a result of global magnetic field changes and can therefore be an effective alternative for imaging the midbrain regions (vanderMeulen, Groen et al. 1985; vanderMeulen, Groen et al. 1988; Bernstein, King et al. 2004). This technique acquires data in 3-D, with two phase encoding directions that can both be accelerated with SENSE, allowing complete volumes to be acquired at high temporal resolutions (1-2 s per volume). SENSE implementation of parallel imaging uses the spatial sensitivity profiles of separate coils to unfold aliased images after reconstruction to image space. This type of scan produces images that are less distorted because the time to traverse k-space is reduced, and it is also less susceptible to physiological noise (Sexton, Gore et al. 2009).

Another 3-D pulse sequence that is also used for functional imaging is PRinciples of Echo Shifting using a Train of Observations, PRESTO (Liu, Sobering et al. 1993; Golay, Pruessmann et al. 2000). In this multi-shot 3-D echo volume acquisition, an echo shifting technique is implemented to make optimal use of the time between the radio frequency excitation pulse and the readout by applying the next excitation before signal readout (Gelderen, Ramsey et al. 1995; Ramsey, Brink et al. 1998). This 3-D T2*-weighted MR sequence has been reported to capture BOLD responses in a cortical study at 7 T (Barry, Strother et al. 2011). The spatial resolution in 3-D methods (FFE and PRESTO) can be higher (sub-millimeter) than in single-shot EPI methods because an increase in SENSE factor in either phase-encoding direction reduces image acquisition read out time. Some of the drawbacks of using multi-shot sequences include higher sensitivity to between-shot motion and phase errors (Neggers, Hermans et al. 2008). The use of phase correction algorithms with navigator echoes (Stenger, Noll et al. 1998; Versluis, Peeters et al. 2010) may help to mitigate some of these errors.

Optimizing scan parameters for imaging the midbrain

In addition to testing the feasibility of MR pulse sequences, we also examined various imaging parameters that could be optimized for functional imaging of the midbrain. Previous midbrain fMRI studies at lower field strengths (3 T) used spatial voxel resolutions of 1.5 x 1.5 x 1.9 mm^3 (D'Ardenne, McClure et al. 2008) or 3 x 3 x 3mm^3 (Bunzeck and Duzel 2006). The SN and VTA are adjacent brain structures and our goal was to distinctly localize BOLD activations in these regions. We, therefore, attempted to push the resolution envelope toward 1 mm^3. This is, however, not possible without weighing the trade-offs between slice coverage, temporal resolution (volume acquisition time), SENSE factors and overall scan duration. For the purposes of measuring BOLD responses in future fMRI studies, we desired a slice coverage that would span the entire dorso-ventral dimension of the SN and VTA and also include parts of the ventral striatum (a major projection site of the midbrain DA neurons).

Additionally, a volume acquisition time of 2 s has been previously used for implementing the monetary incentive delay task (Knutson, Westdorp et al. 2000; Knutson, Fong et al. 2003). This task has been shown to activate the midbrain reward circuitry and could be potentially used for task-related 7 T fMRI in the midbrain. We thus aimed to achieve a volume acquisition time that was close to 2 s. We also examined the effect of modifying SENSE factor. Sensitivity encoding makes use of the spatial sensitivity profiles of separate receive coils to under sample the data acquired thereby shortening acquisition time, reducing magnetic susceptibility artifacts and increasing spatial or temporal resolution (Pruessmann, Weiger et al. 1999; Weiger, Pruessmann et al. 2002; Wiesinger, Moortele et al. 2006). Finally, in designing an optimum imaging protocol, we ensured that the scan duration of each fMRI run was not too lengthy so as to minimize loss of attention in the participants during a task-related scan.

Sources of noise in the midbrain and its influence on image acquisition

There are various sources of noise in the midbrain. These sources include CSF flow in the IPF, motion of the brainstem due to cardiac pulsatility in the arteries within and surrounding the midbrain, chest movement associated with respiration and thermal noise associated with scanner electronics. In the realm of fMRI, an additional physiological noise component includes BOLD-related hemodynamic and metabolic fluctuations in gray matter (Weisskoff 1996; Krüger, Kastrup et al. 2001). While the ratio between physiologic noise and thermal noise is supposed to increase with increasing field strength, moving toward higher spatial resolution at high field strengths has been shown to reduce this ratio, especially when TE is near T2* (Triantafyllou, Hoge et al. 2005). Noise effects typically manifest as image artifacts (distortion, ghosting and multi-shot phase reconstruction errors) that vary within a slice, through the imaging volume and through time.

Cardiac and respiratory cycles can be monitored during fMRI scans, and the recordings can be used to retrospectively compensate for these sources of physiological noise using various correction algorithms (Le and Hu 1996; Glover, Li et al. 2000; Thomas, Harshman et al. 2002). RETROICOR has been shown to remove quasi-periodic respiration and cardiac cycles in 2-D single-shot EPI data, assuming that the cardiac and respiratory variances do not overlap with task-related variance.

Motion of the brainstem

The brainstem is surrounded by arteries and areas of CSF flow, so bulk motion associated with pulsatility in these regions can affect the detectable BOLD signal in the midbrain. Studies have reported an overall brainstem displacement in the inferior and anterior directions during cardiac systole (Greitz, Wirestam et al. 1992). Using different prospective and retrospective cardiac-gated MR scans, previous studies have shown a rostro-caudal displacement in the midbrain-pons region of 0.16 ± 0.2 mm with peak velocities of 1.1 - 1.5 mm/s (Enzmann and Pelc

79

1992; Soellinger, Ryf et al. 2007). Another report described brainstem motion as a single rostro-caudal displacement in systole followed by a slow return to the original position in diastole (Poncelet, Wedeen et al. 1992). Displacement according to this study involved the midbrain and brainstem descending towards the foramen magnum with velocities increasing with proximity to the foramen (< 2 mm/s) and an associated medial compression of the thalami on the third ventricle (< 1.5 mm/s). Depending on the voxel resolution chosen for the fMRI sequence, this may or may not be an issue in accurately localizing the spatial activation of the BOLD signal.

In this study, we tested the efficacy of 2-D EPI and 3-D FFE pulse sequences for performing fMRI in the midbrain. Various imaging parameters were modified in these two sequences, including voxel resolution, volume acquisition time, and SENSE factors. Qualitative assessments involved observing visual distortions in the images acquired in both sequences. TSNR was also measured in the midbrain structures of interest (SN and VTA) to quantify the signal intensity differences between the two imaging sequences. In addition, we examined the feasibility of using RETROCIOR as a post-processing step and brainstem motion was retrospectively measured to estimate the displacement of the midbrain over a cardiac cycle.

Methods

Participants

Single participant studies were performed for each of the following scans: a) comparing 2-D EPI and 3-D FFE sequences (male, 27 years of age) and b) measuring brainstem motion using a retrospective cardiac-gated scan (male, 26 years of age). The participants provided written informed consent for the study, which was approved by the institutional review board of Vanderbilt University Medical Center. They were compensated $40 for participation in resting state scans. When required to do a task, they were compensated $40 in addition to 20% of their total earnings in the PE-MID task.

Slice positioning and slab orientation

From our experience with anatomical imaging of the midbrain, we used an axial slice orientation in order to cover both the VTA and SN in the same slice. Previous imaging studies using the reward-based task had reported activations in the ventral striatum as well as the midbrain (D'Ardenne, McClure et al. 2008). This indicated that in order to capture the spatial extent of the reward circuitry, the slices should be positioned in an oblique axial fashion, covering the entire midbrain and ventral portions of the basal ganglia (just below the caudate head). The field of view (FOV) on the anterior edge covered portions of the inferior frontal lobe (just above the sinuses), and the posterior edge covered parts of the cerebellum and the inferior occipital cortex. Having this anterior-posterior (AP) dimension for the scans prevented wrap-around in the AP plane. The shim box was centered on the midbrain and the ventral striatum, ensuring appropriate B_0 shimming in the areas of interest.

fMRI data acquisition

Images were acquired using a 32 channel 7 T Achieva Scanner (Philips Healthcare, Cleveland, Ohio). Whole brain 3-D anatomical scans were acquired using a T1-weighted Turbo Field Echo pulse sequence for all scan sessions. Images were acquired in the sagittal orientation with field of view (FOV) = 256 (FH) x 256 (AP) x 172.5 (RL) mm, reconstruction matrix = 204 x 204, parallel imaging factor, SENSE = 2 in the AP direction, repetition time (TR) = 3.0 ms, echo time (TE) = 1.35 ms, voxel resolution =1.25 mm x 1.25 mm x 1.25 mm with zero gap, flip angle (FA) = 7°, slices =138 and acquisition time = 2 min and 12.2 s. This high resolution structural scan was used to determine the slice placement for the functional scans.

T2*-weighted BOLD images for all sequences described below were acquired in an oblique axial orientation with slices oriented to cover the dorso-ventral extent of the midbrain from the inferior edge of the caudate head to the dorsal border of the pons. The axial sections were tilted such that they were parallel to a plane bisecting the mammillary body and the inferior

frontal lobe. While it is known that optimal BOLD contrast is attained at a TE value close to the T2* value of the structure of interest (Gati, Menon et al. 1997), we could not follow that rule in this study. The SN has a T2* value of approximately 14 ms, and the VTA has a T2* value of approximately 28 ms. We were interested in observing a BOLD contrast in both of these structures, so we arbitrarily chose a value of 20 ms for the TE. A pencil beam volume shim was used for all scans (Gruetter and Boesch 1992; Gruetter 1993).

The 2-D single-shot EPI sequences had the following similar imaging parameters: FOV = 170 (AP) x 170 (RL), TE = 20 ms and 14 slices. Repetition times, TR (volume acquisition times) varied between $1 - 2$ s, SENSE factors ranged between 3- 4 in the RL direction, and FA varied between 50° and 60°. Three different voxel resolutions were tested including 1.06 mm x 1.06 mm x 1.10 mm , 1.18 mm x 1.18 mm x 1.18 mm and 1.33 mm x 1.33 mm x 1.33 mm. See Table 3 for full details of scan parameters.

The 3-D FFE sequences had the following similar imaging parameters: FOV = 170 (AP) x 170 (RL), TE = 20 ms and FA = 15°. Volume acquisition times varied between 2 -2.5 s, SENSE factors ranged between $2.7 - 3.4$ in the RL direction, and slice coverage varied between12- 14 slices. Three different voxel resolutions were tested including 0.97 mm x 0.97 mm x 1.10 mm, 1.18 mm x 1.18 mm x 1.18 mm and 1.33 mm x 1.33 mm x 1.33 mm. TR (time between shots) was 28 ms (for the 0.97 x 0.97 x 1.10 mm^3 voxel), 30 ms (for the 1.18 x 1.18 x 1.18 mm^3 voxel) and 33 ms (for the 1.33 x 1.33 x 1.33 mm^3 voxel). See Table 3 for full details of scan parameters.

Table 3: **Imaging parameters for 2-D EPI and 3-D FFE sequences.** TR is the repetition time, TE is the time to echo and RL refers to SENSE acceleration in the Right-Left plane.

Sequence	Voxel Resolution (mm³)	Reconstruction Matrix (mm)	Volume acquisition time (s)	TR (ms)	TE (ms)	# Slices	SENSE (RL)	Flip Angle (deg)	# Dynamics	Scan Time (min:sec)
2D EPI	1.06 x 1.06 x 1.10	156 x 160	1	1000	20	14	4	60	100	1:48
2D EPI	1.18 x 1.18 x 1.18	144 x 144	1	1000	20	14	4	60	100	1:48
2D EPI	1.33 x 1.33 x 1.33	128 x 128	1	1000	20	14	3	50	100	1:48
2D EPI	1.33 x 1.33 x 1.33	128 x 128	1	1000	20	14	4	50	200	3:28
2D EPI	1.33 x 1.33 x 1.33	128 x 128	2	2000	20	14	4	50	200	6:56
3D FFE	0.97 x 0.97 x 1.10	156 x 176	2.5	28	20	14	2.9	15	100	4:10
3D FFE	1.18 x 1.18 x 1.18	144 x 144	2	30	20	13	3.4	15	100	3:21
3D FFE	1.33 x 1.33 x 1.33	128 x 128	2.4	33	20	14	2.7	15	100	3:57
3D FFE	1.33 x 1.33 x 1.33	128 x 128	2	33	20	12	3.1	15	100	6:39

The participant's pulse rate was monitored using a peripheral pulse unit (PPU) that interfaced with the scanner. It was placed on the left middle or index finger of the participant. The participant's respiration was monitored using a respiratory belt placed around the abdomen or sternum area. The location was chosen based on the region that exhibited largest motion during normal breathing. This belt also interfaced with the scanner. Both the PPU and the respiration physiological component measurements were sampled at 500 Hz and stored in a log file during each scan session.

Retrospective cardiac gating for brainstem motion

A retrospective cardiac-gated scan was used to evaluate the extent of brainstem motion in the anterior-posterior (AP), right –left (RL) and superior-inferior directions (Head-Foot, HF). A finger PPU was used to synchronize the scans with the cardiac rate. Sixteen time points were collected through the cardiac cycle, each at an interval of 75 ms. The scan was thus cardiac gated since the sixteen time points were measured along a cardiac cycle. Over the course of the scan, 80-90 heart beats were acquired and each time point was retrospectively averaged over all the heart beats. During reconstruction the scanner produces a phase image that contains the average

velocity of each of the time points. The imaging parameters for this 2-D scan was: FOV = 220 mm (AP) x 180 mm (RL) x 5 mm (FH), SENSE factor = 2 in the RL direction, TR = 8 ms, TE = 13 ms, one slice with a voxel resolution = 1.00 mm x 0.99 mm x 5.00 mm, FA = 10° and number of signal averages (NEX) = 2. In this flow compensated scan, a quantitative phase contrast measurement was made with a velocity encoding factor of 1 cm/s. The phase shift varied over π degrees. The imaging volumes were acquired in the AP, RL & HF directions, each run lasting 1 min and 35 s.

fMRI data analysis

Functional images were corrected for participant head motion and analyzed using Statistical Parametric Mapping (SPM5; Wellcome Department of Imaging Neuroscience, University College, London, UK). The EPI scan sequences were slice time corrected, and a modified version of the original RETROICOR algorithm (Glover, Li et al. 2000) was implemented using Matlab (version R2010a, MathWorks, Natick, Massachusetts), courtesy of Dr. Rob Barry. In the 3-D multi-shot FFE scan, all lines of k-space are not acquired in a single-shot, so scan time correction is not an appropriate preprocessing step. Instead, after motion correction, the FFE scans were directly run through the RETROICOR algorithm.

Estimating TSNR:

For the fMRI scans, we calculated the mean signal in every voxel and the standard deviation (SD) in every voxel over time. TSNR was determined in every voxel by taking the calculated mean signal and dividing it by the calculated SD value for each time point. Region of interest (ROI) masks of the SN and VTA were drawn in the mean signal fMRI data. These masks were used to extract the TSNR in an ROI by taking the mean of the TSNR in the voxels falling within the ROI.

Power spectrum density curve

In order to view the improvement in the data observed after implementing RETROICOR, the data need to be transformed into the frequency domain. The frequency transformed data show power spectra within the entire frequency range that can be sampled with the given dynamic scan time (TR for EPI scans). For example, with a TR = 2 s, you can only sample up to 0.25 Hz (Nyquist sampling rate = $1/2 * TR^{-1}$). Along the frequency domain, we know the source of certain frequencies, particularly the cardiac (approximately 1 Hz) and respiratory signals (approximately 0.25 Hz). Moreover, if we used a task in which the trial length varied from 10 -14 s, the task-related frequency in the frequency domain would range between 0.07 – 0.1 Hz.

Evaluating motion of the brainstem using retrospective gating

Both magnitude and phase data were collected in the retrospective cardiac-gated scans. An arbitrary ROI outside the brain was chosen as the position expected to move the least over the cardiac cycle (e.g., fatty tissue surrounding the skull). The entire midbrain region, VTA and SN were drawn on the magnitude image. The phase data contained velocity information for the entire imaging volume and the masks of the midbrain ROIs (drawn on the magnitude data) were used to extract velocity information from the phase data. We used the difference in velocity between midbrain ROIs and the outside-brain ROI to estimate the relative velocity of the midbrain ROIs over a cardiac cycle. Using the velocity information and the time interval of each phase, we calculated the distance travelled in each phase. Net displacement from the original position, average and peak velocities were calculated from this information.

Results

The EPI and FFE scans exhibited visible contrast in the midbrain region. Distortion was observed in areas near the frontal sinus as well as around the ear canals for the EPI scans (Figure

19). While signal drop out is seen in both the EPI and FFE scans, the FFE image displayed more spatial stability. Higher TSNR was observed for the FFE scan in both the SN and VTA than for the EPI sequence (Table 4). As expected, the SN had lower signal compared to the VTA due to signal loss associated with the DA neurons containing neuromelanin rich iron. Voxel resolutions close to 1 mm^3 revealed low TSNR in the SN and VTA for both EPI and FFE sequences. A voxel resolution of 1.33 mm^3 enabled largest coverage with highest TSNR for the EPI sequence (Table 4). At this same voxel resolution, the FFE sequence had slightly smaller coverage, but higher TSNR compared to the EPI sequence. As a point of comparison, at the same resolution, the TSNR values in the visual cortex at 7 T was 40-50 for these two scan sequences (results not shown here).

Table 4: **Imaging parameters along with TSNR measurements in the SN and VTA for 2-D EPI and 3-D FFE sequences.** TR is the repetition time, TE is the time to echo and RL refers to SENSE acceleration in the Right-Left plane.

Sequence	Voxel Resolution (mm^3)	Volume acquisition time (s)	TR (ms)	TE (ms)	# Slices	SENSE (RL)	Flip Angle (deg)	# Dynamics	Scan Time (min:sec)	TSNR SN	TSNR VTA
2D EPI	1.06 x 1.06 x 1.10	1	1000	20	14	4	60	100	1:48	2.513	4.689
2D EPI	1.18 x 1.18 x 1.18	1	1000	20	14	4	60	100	1:48	3.891	6.771
2D EPI	1.33 x 1.33 x 1.33	1	1000	20	14	3	50	100	1:48	5.088	9.589
2D EPI	1.33 x 1.33 x 1.33	1	1000	20	14	4	50	200	3:28	3.616	5.953
2D EPI	1.33 x 1.33 x 1.33	2	2000	20	14	4	50	200	6:56	4.580	8.650
3D FFE	0.97 x 0.97 x 1.10	2.5	28	20	14	2.9	15	100	4:10	4.738	7.910
3D FFE	1.18 x 1.18 x 1.18	2	30	20	13	3.4	15	100	3:21	4.627	9.639
3D FFE	1.33 x 1.33 x 1.33	2.4	33	20	14	2.7	15	100	3:57	8.339	12.409
3D FFE	1.33 x 1.33 x 1.33	2	33	20	12	3.1	15	100	6:39	5.850	11.340
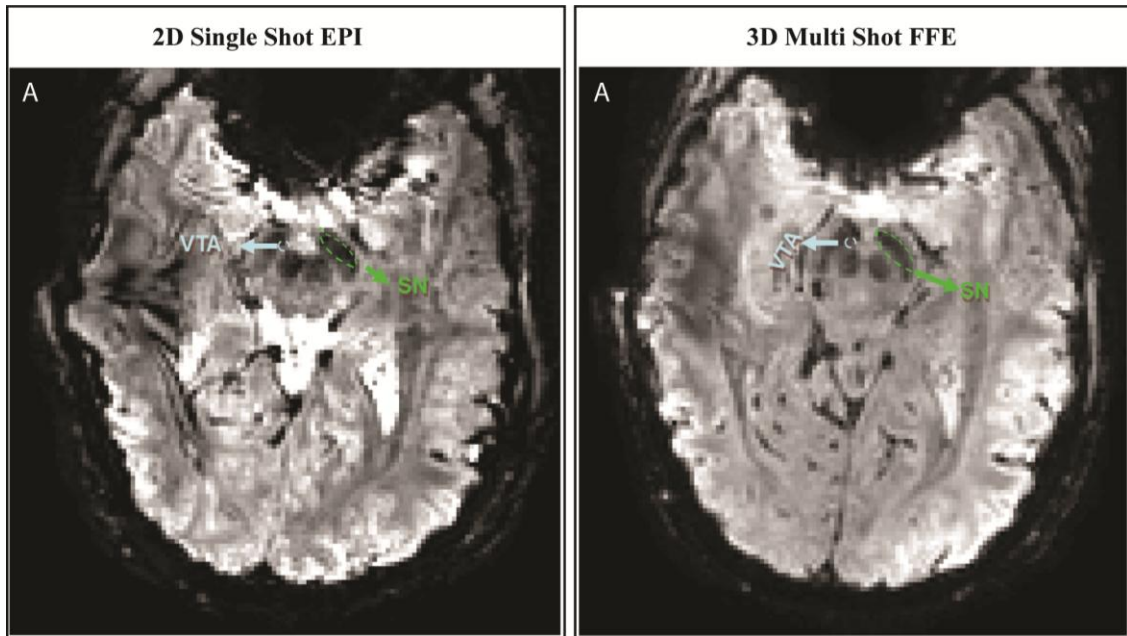
Figure 19: **functional MRI scans at 7 T using 2-D EPI and 3-D FFE.** 2-D single-shot gradient echo EPI sequence (left panel) and a 3-D multi-shot gradient echo FFE sequence (right panel) for a 1.33 mm^3 voxel volume is displayed here. The panel shows mean image with a section of the midbrain at the level of the superior colliculus. '**A**' denotes the anterior portion of the brain.

RETROICOR was used to regress out variance associated with cardiac and respiratory signals. This algorithm improved the signal within the SN and VTA by reducing the power in the pertinent frequency ranges (task and respiratory frequencies), assuming the task falls within the 0.07-0.1 Hz range (for trials that are 10-14 s in length). For example, in the left VTA, there was a 20% decrease in the power observed in the task frequency range and a 27% decrease in the power observed in the respiration frequency range (Figure 20). Similarly, in the left SN, there was a 16% decrease in the power observed in the task frequency range and a 44% decrease in the power observed in the respiration frequency range (Figure 20).
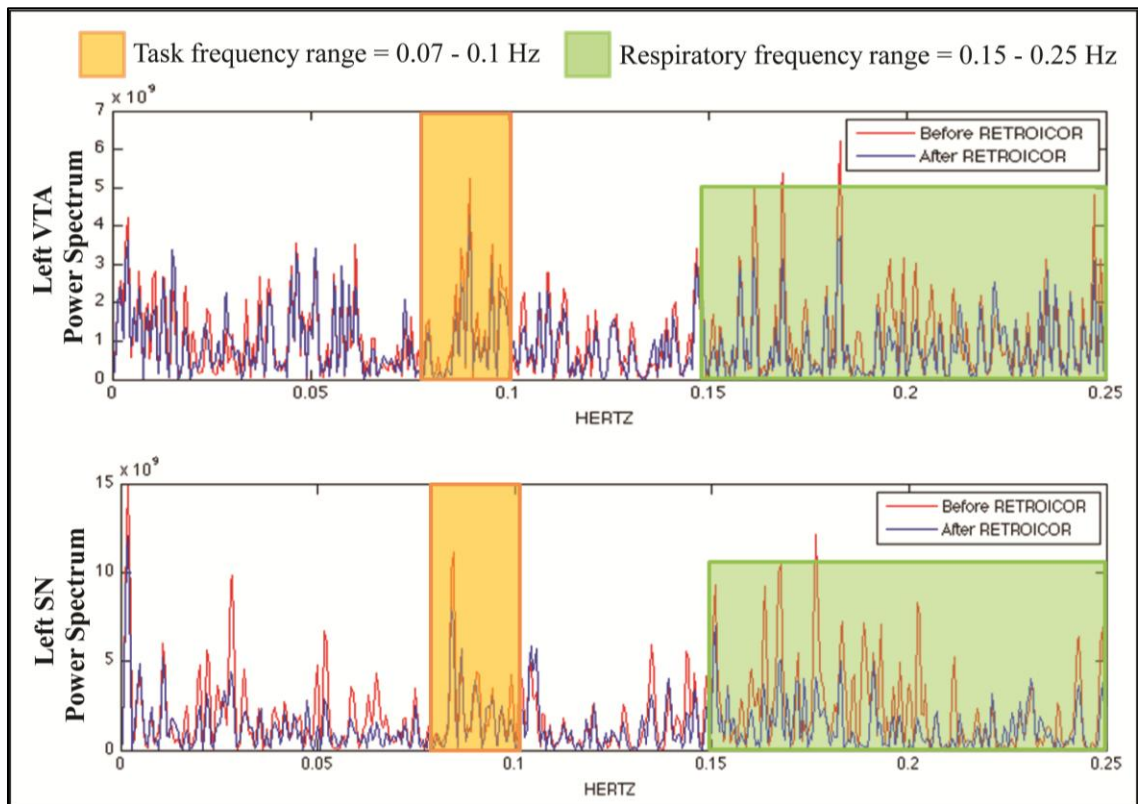
Figure 20: **Power spectrum density curves displaying the effect of RETROICOR.** Results are displayed as a power spectrum density function for the left VTA and left SN in a FFE scan. Red lines indicate data before RETROICOR was implemented and blue lines represent data after RETROICOR was implemented. The orange and green shaded regions represent the task and respiration frequencies, respectively, assuming task varies between 10-14 s.

Using retrospective cardiac-gating, the net displacements and velocities of midbrain nuclei (SN, VTA) and the entire midbrain region were estimated in one individual (Figure 21). The net displacement in a specific direction was highest in the foot direction (0.11 mm, Figure 21, middle panel) and second highest in the anterior direction (0.048 mm, Figure 21, left panel). Additionally, the average velocity did not go beyond 0.19 mm/s in the head-foot direction and 0.25 mm/s in the anterior-posterior direction (Figure 21, right panel).
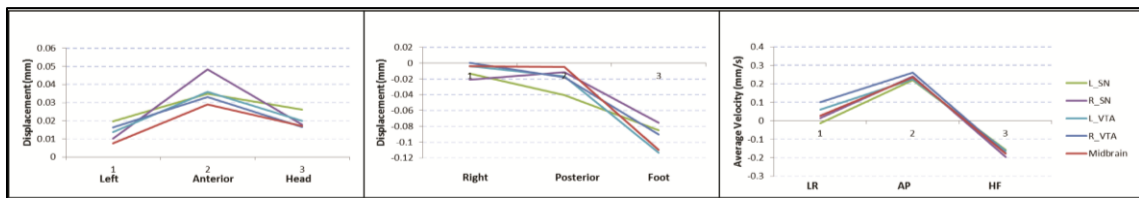
Figure 21: **Plots of brainstem motion using a retrospective cardiac gated scan.** Plots of the midbrain revealing net displacement and average velocity of a region from the original position. These measurements are calculated along the cardiac cycle. **LR** = Left-Right direction; **AP** = Anterior-Posterior direction; **HF** = Head-Foot direction; **SN** = Substantia nigra; **VTA** = Ventral Tegmental Area; L/R_SN = left/right Substantia Nigra; L/R_VTA = left/right Ventral Tegmental Area.

Discussion

The goals of this study were three fold: 1) to explore and optimize MR pulse sequences and imaging parameters for functional imaging of the midbrain, 2) to test the efficacy of a post-processing noise correction algorithm, RETROICOR, and 3) to quantify the motion in the brainstem resulting from cardiac pulsatility.

2-D and 3-D sequences were tested as candidate fMRI scans for imaging the midbrain area. While the EPI sequences demonstrated visual contrast sensitivity in the midbrain, slight distortion was observed in the anterior parts of the brain as well as around the ear canals (Figure 19). The FFE scans, conversely, were qualitatively clearer (no observable distortions) and provided excellent contrast in the midbrain. Comparing between voxel resolutions, the FFE scans had higher TSNR in the midbrain SN and VTA relative to the EPI scan (Table 4). Voxel resolutions close to 1 mm^3 revealed low TSNR in the SN and VTA in both EPI and FFE sequences, suggesting low signal sensitivity and possibly high noise sensitivity. At the chosen TE of 20 ms, a voxel resolution of 1.33 mm^3 with a volume acquisition time of 2 s proved to be optimum for imaging the midbrain with minimal distortion, maximum slice coverage (14 slices for EPI and 12 slices for FFE) and highest TSNR. SENSE factors of 3 for the EPI scans and 3.1 for the FFE scans were also determined to be optimal within the other imaging parameter constraints. Thus, both EPI and FFE sequences could be used for fMRI in the midbrain.

Implementing RETROICOR as a post-processing step primarily reduced the influence of the respiratory physiologic signal. This was observed in the power spectrum density curve (Figure 20), in which RETROICOR demonstrated a power reduction of 27% in the VTA and 44% in the SN for the respiratory frequency range. It is important to note here that with a 2 second dynamic scan time (TR for EPI scans), data sampling was limited to 0.25 Hz, which corresponds to the upper edge of the respiratory frequency range. Cardiac frequencies typically fall near 1Hz (assuming a heart rate with an average of 60 beats per minute), and since we were unable to

sample data at this frequency range, the cardiac frequencies were aliased into the lower frequency ranges (typically under 0.1Hz). Thus, while RETROICOR may effectively regress out variance associated with respiration, it may not be able to do the same with the cardiac component. In fact, RETROICOR has been shown to not remove slower (~0.03 Hz) signal changes induced by breath-to-breath variations with the depth and rate of breathing (Birn, Smith et al. 2008). Similarly, signal fluctuations less than 0.1 Hz also have been reported to not be effectively removed by RETROICOR (Shmueli, Gelderen et al. 2007). These low frequency fluctuations (< 0.1 Hz) can include breathing variability, resting state default mode network activity (~0.03 Hz), beat-to-beat variability in the cardiac rate and higher order harmonics of the cardiac frequencies aliased to very low frequencies. In our data, the task-related frequency ranged from 0.07 to 0.1 Hz, and the power spectrum density curve in our study (Figure 20) revealed that RETROICOR may remove some power in this task frequency window. Future studies with higher temporal resolutions (~ 450 ms) that can sample both the cardiac and respiratory frequency ranges may be able to evaluate the effectiveness of RETROICOR in removing variance in both these physiologic frequency ranges.

The original RETROICOR algorithm developed by Glover *et al*., (Glover, Li et al. 2000) was shown to work effectively for single-shot 2-D EPI sequences in which each image is collected at a discrete time and unique cardiac and respiratory phases can be assigned for these images. The same principle may not hold true for 3-D multi-shot acquisitions since one TR does not represent an entire image. In 3-D multi-shot sequences (as in FFE), images are acquired over multiple TRs before the entire image is combined into a full volume (different lines of k-space collected at different times). Consequently, one image may span several cardiac cycles (~2) and a substantial fraction of a respiratory cycle. Nonetheless, for the 3-D FFE scans in our study, RETROICOR mediated power reductions in the respiratory physiologic frequencies. However, its efficacy to reduce cardiac noise is uncertain at this point.

From the retrospective brainstem cardiac-gated scan, we know that the overall displacement of the midbrain was maximal in the anterior and inferior directions (0.05 mm in the anterior direction and 0.11 mm in the foot direction, Figure 21). When considering a spatial resolution of 1.33 mm x 1.33 mm x 1.33 mm (~ 2.35 mm^3 in volume), these displacements represent less than 5% of the voxel volume. This implies that bulk motion associated with cardiac pulsatility does not significantly contribute to the noise in this area of the brain.

Overall, in this study we were able to test multiple fMRI pulse sequences and manipulate various imaging parameters to establish a standardized protocol for optimally imaging the midbrain. Images from the FFE sequence exhibited more visual stability than those observed in the EPI scans. Moreover, higher TSNR was observed in the midbrain regions of interest for the FFE in comparison to the EPI sequence. Considering various imaging constraints, a voxel resolution of 1.33 m^3 with a volume acquisition time of 2 s was determined to be optimal for doing functional imaging in the midbrain. Implementing RETROICOR as a post-processing step primarily reduced noise variance in the respiratory frequencies. However, its effectiveness in regressing out cardiac noise is not fully understood. RETROICOR may need to be tested in studies that can sample both the respiratory and cardiac frequency ranges in order to assess its merit at successfully reducing physiological noise in the midbrain. Additionally, we demonstrated that brainstem motion from cardiac pulsatility was not substantial in the midbrain and hence would not be a significant source of noise in this area.

Conclusion

In conclusion, we established that both 2-D EPI and 3-D FFE can be used as MR sequences for functional imaging in the midbrain. The FFE sequence had minimal distortions and slightly higher TSNR compared to the EPI sequence, making it the more viable option for 7T fMRI of the midbrain. Voxel resolution, volume acquisition times and SENSE factors were

modified to develop a protocol for efficiently imaging the midbrain. RETROICOR successfully worked as post-processing technique for the respiration physiological component. However, its efficacy in reducing cardiac variance is still to be confirmed. Brainstem motion in the midbrain using a retrospective cardiac-gated scan was very small compared to the overall voxel imaging volume, implying that motion due to cardiac pulsatility is not a significant source of physiological noise in the midbrain.

References

Barry, R., S. Strother, et al. (2011). "Data-driven optimization and evaluation of 2-D EPI and 3-D PRESTO for BOLD fMRI at 7 Tesla: I. Focal coverage." NeuroImage **55**(3): 1034-1043.

Bernstein, M., K. King, et al., Eds. (2004). Handbook of MRI Pulse Sequences. San Diego, California, Elsevier Academic Press.

Birn, R. M., M. A. Smith, et al. (2008). "The respiration response function: the temporal dynamics of fMRI signal fluctuations related to changes in respiration." Neuroimage **40**(2): 644-654.

Bunzeck, N. and E. Duzel (2006). "Absolute Coding of Stimulus Novelty in the Human Substantia Nigra/VTA." Neuron **51**(3): 369-379.

D'Ardenne, K., S. M. McClure, et al. (2008). "BOLD Responses Reflecting Dopaminergic Signals in the Human Ventral Tegmental Area." Science **319**(5867): 1264-1267.

Duyn, J., Y. Yang, et al. (1996). "Functional magnetic resonance neuroimaging data acquisition techniques." Neuroimage **4**(3 Pt 3): S76-83.

Enzmann, D. R. and N. J. Pelc (1992). "Brain motion: measurement with phase-contrast MR imaging." Radiology **185**(3): 653-660.

Gati, J. S., R. S. Menon, et al. (1997). "Experimental Determination of the BOLD Field Strength Dependence in Vessels and Tissue." Magn Reson Med. **38**(2): 296-302.

Gelderen, P. v., N. Ramsey, et al. (1995). "Three-dimensional functional magnetic resonance imaging of human brain on a clinical 1.5-T scanner." Proc Natl Acad Sci U S A. **92**(15): 6906-6910.

Golay, X., K. Pruessmann, et al. (2000). "PRESTO-SENSE: an ultrafast whole-brain fMRI technique." Magn Reson Imaging **43**(6): 779-786.

Glover, G. H., T.Q. Li, et al. (2000). "Image-based method for retrospective correction of physiological motion effects in fMRI: RETROICOR." Magn Reson Imaging **44**(1): 162-167.

Greitz, D., R. Wirestam, et al. (1992). "Pulsatile brain movement and associated hydrodynamics studied by magnetic resonance phase imaging." Neuroradiology **34**(5): 370-380.

Gruetter, R. (1993). "Automatic, localized in vivo adjustment of all first- and second-order shim coils." Magn Reson Med. **29**(6): 804-811.

Gruetter, R. and C. Boesch (1992). "Fast, Noniterative Shimming of Spatially Localized Signals. In Vivo Analysis of the Magnetic Field along Axes." Journal of Magnetic Resonance **96**(323-334): 323.

Knutson, B., G. W. Fong, et al. (2003). "A region of mesial prefrontal cortex tracks monetarily rewarding outcomes: characterization with rapid event-related fMRI." NeuroImage **18**(2): 263-272.

Knutson, B., A. Westdorp, et al. (2000). "FMRI Visualization of Brain Activity during a Monetary Incentive Delay Task." NeuroImage **12**(1): 20-27.

Krüger, G., A. Kastrup, et al. (2001). "Neuroimaging at 1.5 T and 3.0 T: comparison of oxygenation-sensitive magnetic resonance imaging." Magn Reson Med **45**(4): 595-604.

Le, T. and X. Hu (1996). "Retrospective estimation and correction of physiological artifacts in fMRI by direct extraction of physiological activity from MR data." Magn Reson Med. **35**(3): 290.

Liu, G., G. Sobering, et al. (1993). "A functional MRI technique combining principles of echo-shifting with a train of observations (PRESTO)." Magn Reson Imaging **30**(6): 764-768.

Mansfield, P., R. Coxon, et al. (1994). "Echo-planar imaging of the brain at 3.0 T: first normal volunteer results." J Comput Assist Tomogr. **18**(3): 339-343.

Neggers, S., E. Hermans, et al. (2008). "Enhanced sensitivity with fast three-dimensional blood-oxygen-level-dependent functional MRI: comparison of SENSE-PRESTO and 2-D-EPI at 3 T." NMR Biomed **21**(7): 663-676.

Poncelet, B. P., V. J. Wedeen, et al. (1992). "Brain parenchyma motion: measurement with cine echo-planar MR imaging." Radiology **185**(3): 645-651.

Pruessmann, K., M. Weiger, et al. (1999). "SENSE: sensitivity encoding for fast MRI." Magn Reson Med. **42**(5): 952-962.

Ramsey, N. F., J. S. v. d. Brink, et al. (1998). "Phase Navigator Correction in 3-D fMRI Improves Detection of Brain Activation: Quantitative Assessment with a Graded Motor Activation Procedure." NeuroImage **8**(3): 240-248.

Sexton, J., J. Gore, et al. (2009). "Multi-Resolution Comparison of Single-Shot EPI, 3-DFFE, and PRESTO for fMRI at 7 T." ISMRM Abstract Proceedings.

Shmueli, K., P. v. Gelderen, et al. (2007). "Low-frequency fluctuations in the cardiac rate as a source of variance in the resting-state fMRI BOLD signal." NeuroImage **38**(2): 306-320.

Soellinger, M., S. Ryf, et al. (2007). "Assessment of Human Brain Motion Using CSPAMM." Journal Of Magnetic Resonance Imaging **25**: 709-714.

Stenger, V., D. Noll, et al. (1998). "Partial Fourier reconstruction for three-dimensional gradient echo functional MRI: comparison of phase correction methods." Magn Reson Med **40**(3): 481-490.

Thomas, C., R. Harshman, et al. (2002). "Noise reduction in BOLD-based fMRI using component analysis." Neuroimage **17**(3): 1521-1537.

Triantafyllou, C., R. D. Hoge, et al. (2005). "Comparison of physiological noise at 1.5 T, 3 T and 7 T and optimization of fMRI acquisition parameters." NeuroImage **26**(1): 243-240.

vanderMeulen, P., J. Groen, et al. (1985). "Very fast MR imaging by field echoes and small angle excitation." Magn Reson Imaging **3**(3): 297-299.

vanderMeulen, P., J. Groen, et al. (1988). "Fast Field Echo imaging: an overview and contrast calculations." Magn Reson Imaging **6**(4): 355-368.

Versluis, M. J., J. M. Peeters, et al. (2010). "Origin and reduction of motion and f0 artifacts in high resolution T2*-weighted magnetic resonance imaging: application in Alzheimer's disease patients." NeuroImage **51**(3): 1082-1088.

Weiger, M., K. Pruessmann, et al. (2002). "2-D SENSE for faster 3-D MRI." MAGMA. **14**(1): 10-19.

Weisskoff, R. (1996). "Simple measurement of scanner stability for functional NMR imaging of activation in the brain." Magn. Reson. Med **36**(4): 643-645.

Wiesinger, F., P. V. d. Moortele, et al. (2006). "Potential and feasibility of parallel MRI at high field." NMR Biomed. **19**(3): 368-378.

CHAPTER V

FUNCTIONAL IMAGING OF THE HUMAN MIDBRAIN DOPAMINE SYSTEM USING A REWARD TASK

Abstract

In order to observe distinct and differential blood oxygen level dependent (BOLD) responses in the midbrain substantia nigra (SN) and ventral tegmental area (VTA), we ran functional MRI (fMRI) scans in conjunction with a reward task, a modified version of the monetary incentive delay task. Following the imaging protocol guidelines developed in the previous chapter, we employed three different pulse sequences to assess the consistency of BOLD activation patterns in the midbrain SN and VTA across multiple individuals. These included a 2-D single-shot echo planar imaging (EPI) at 1.33 mm isotropic voxel resolution, a 3-D multi-shot fast field echo (FFE) at 1.33 mm isotropic voxel resolution and a 3-D multi-shot PRinciples of Echo Shifting using a Train of Observations (PRESTO) at 2.5 mm isotropic voxel resolution. All three sequences were implemented at a repetition time of 2 s to allow for task design constraints. The functional signal was evaluated using the following criteria: 1) exploring the qualitative BOLD activation maps at certain voxel level thresholds, 2) measuring BOLD percent signal changes for certain task-specific contrasts in the midbrain regions of interest (ROIs), 3) determining temporal signal to noise ratio (TSNR) values in midbrain ROIs, and 4) observing temporal correlations between homologous midbrain ROIs and non-homologous midbrain ROIs within task and resting state scans. Within each of the three pulse sequences, we observed that the pattern of functional activations were different, insignificant and irreproducible across individuals. Moreover, TSNR in the midbrain ROIs were low (8-16) indicating substantial temporal noise in these regions. The BOLD percent signal change was also low in the midbrain

for contrasts of interest shown in previous low field studies to robustly activate this area. Within a sequence, the homologous midbrain ROIs exhibited slightly higher temporal correlations compared to their non-homologous counterparts, suggesting the presence of intrinsic fluctuations that contribute to temporal variance but are not random noise.

Introduction

As elaborated in Chapter I, the DA neurons in the midbrain SN and VTA of rodents and non-human primates have been shown to be associated with various goal directed behaviors. Similar to animal model experiments, fMRI studies in humans to date have reported VTA and ventral striatum BOLD activations during conditional associative tasks using appetitive or monetary rewards (Berns, McClure et al. 2001; D'Ardenne, McClure et al. 2008; Buckholtz, Treadway et al. 2010). However, due to limitations in the neuroimaging protocols, the fMRI BOLD activation maps in these studies did not show distinct and differential responses in the midbrain SN and VTA (Chapter I, Figure 4). At higher field strengths (7 Tesla or higher), some of these limitations can be mitigated because of the ability to view smaller voxel dimensions from more localized regions, and because BOLD signals increase with increasing field strength. High SNR also confers the capability to parse out different parts of the hemodynamic response curve, revealing temporal dynamics between brain regions.

Particular to the midbrain, the dense microvasculature within and surrounding the DA areas can augment the local magnetic field inhomogeneities (T2* effects), thus providing enhanced BOLD contrast in T2* sensitive 7 T fMRI sequences. Moreover, the point-spread-function of the BOLD response in human gray matter is known to be narrow at high field, since the signal contribution is more localized in capillary beds than macro-vessels (Shmuel, Yacoub et al. 2007). The type of stimulus used to activate the midbrain DA system can also have an impact on the BOLD contrast and the resulting detectable TSNR. A monetary incentive delay task is

known to probe reward circuitry within the midbrain VTA and SNc. This task has been shown in several 3 T studies to activate the midbrain and the ventral striatum in response to reward anticipation and reward outcome (Knutson, Westdorp et al. 2000; Knutson, Fong et al. 2003). In particular, the DA neurons have been shown to be responsive to prediction errors in rewards (Schultz, Dayan et al. 1997; Berns, McClure et al. 2001; D'Ardenne, McClure et al. 2008). We therefore implemented a prediction error version of the monetary incentive delay task in the present study (PE-MID) in order to examine potential changes in the BOLD response associated with DA activity when the reward magnitude was increased or decreased from the expected amount. According to work performed in non-human primate experiments for prediction error of appetitive stimuli, we should expect a phasic firing of DA neurons when there is an increase in the magnitude of the reward and a cessation of DA firing in the absence of a reward. In our task-based fMRI studies, we expected to see BOLD responses with respect to anticipation after a cue onset, feedback following a reward outcome and related prediction error modulations.

From Chapter IV, we were able to establish certain imaging protocol guidelines to perform functional imaging of the midbrain at 7 T. In the present study, we used these guidelines in a standard single-shot 2-D EPI sequence and multi-shot 3-D FFE and 3-D PRESTO sequences to observe BOLD contrast in the PE-MID task. The PRESTO sequence has been previously shown to robustly activate cortical areas at 7 T (Barry, Strother et al. 2011). We therefore used a 3-D PRESTO sequence at low resolution (similar to those used in low field midbrain fMRI studies) to have another point of comparison relative to the higher resolution 2-D EPI and 3-D FFE sequences. These comparisons were performed across multiple individuals. Apart from viewing activation maps, BOLD percent signal change in various task-related contrasts of interest were assessed in the midbrain ROIs. Additionally, TSNR values were determined in the midbrain ROIs. Temporal correlations between midbrain ROIs were also investigated for task and resting state scans. These time course correlations in the fMRI data may provide an indication of the

temporal dynamics between different midbrain ROIs (homologous and non-homologous pairs) and offer some explanation for potential functional connectivity patterns in the midbrain.

Methods

Participants

Five healthy participants completed the FFE study with the task (5 males, mean age of participants = 26 years) and in this study only the magnitude data were recorded. For the following studies, both real and imaginary image data were retained after magnitude reconstruction. An additional five participants completed the FFE study with task (3 males, mean age of participants = 30.5 years). Five healthy participants completed the EPI study with task (3 males, mean age of participants = 31.2 years). Five healthy participants completed the PRESTO study with task (3 males, mean age of participants = 32 years). Six healthy participants completed the resting state fMRI scans that had EPI, FFE and PRESTO scans (4 males, mean age = 35.17 years). All participants provided written informed consent for the study, which was approved by the institutional review board of Vanderbilt University Medical Center. They were compensated $40 in addition to 20% of their total earnings in the PE-MID task. Participants who completed the resting state scans were compensated $40.

fMRI data acquisition

Images were acquired using a 32 channel 7 T Achieva Scanner (Philips Healthcare, Cleveland, Ohio). Whole brain 3-D anatomical scans were acquired using a T1-weighted Turbo Field Echo pulse sequence for all scan sessions. 138 slices were collected in sagittal orientation with field of view (FOV) = 256 (FH) x 256 (AP) x 172.5 (RL) mm, reconstruction matrix = 204 x 204, parallel imaging factor (SENSE, (Pruessmann, Weiger et al. 1999)) = 2 in the AP direction, repetition time (TR) = 3.0 ms, echo time (TE) = 1.35 ms, voxel resolution =1.25 mm x 1.25 mm x

1.25 mm with zero gap, flip angle (FA) = 7°, acquisition time = 2 min and 12.2 s. This high resolution structural scan was used to determine the slice placement for the functional scans.

T2*- weighted BOLD images for all sequences described below were acquired in an oblique axial orientation with slices positioned to cover the dorso-ventral extent of the midbrain from the inferior edge of the caudate head to the dorsal border of the pons (Figure 22). The axial sections were tilted to make them parallel to a plane bisecting the mammillary body and the inferior frontal lobe. In the T2*-weighted scans, real and imaginary data were retained after magnitude reconstruction. This allowed us to create phase and magnitude data separately in order to run various analysis techniques on the different image types. A volume shim was used for the 2-D EPI scans (Schneider and Glover 1991) and a pencil beam volume shim was used for the 3-D FFE and PRESTO scans (Gruetter and Boesch 1992; Gruetter 1993).
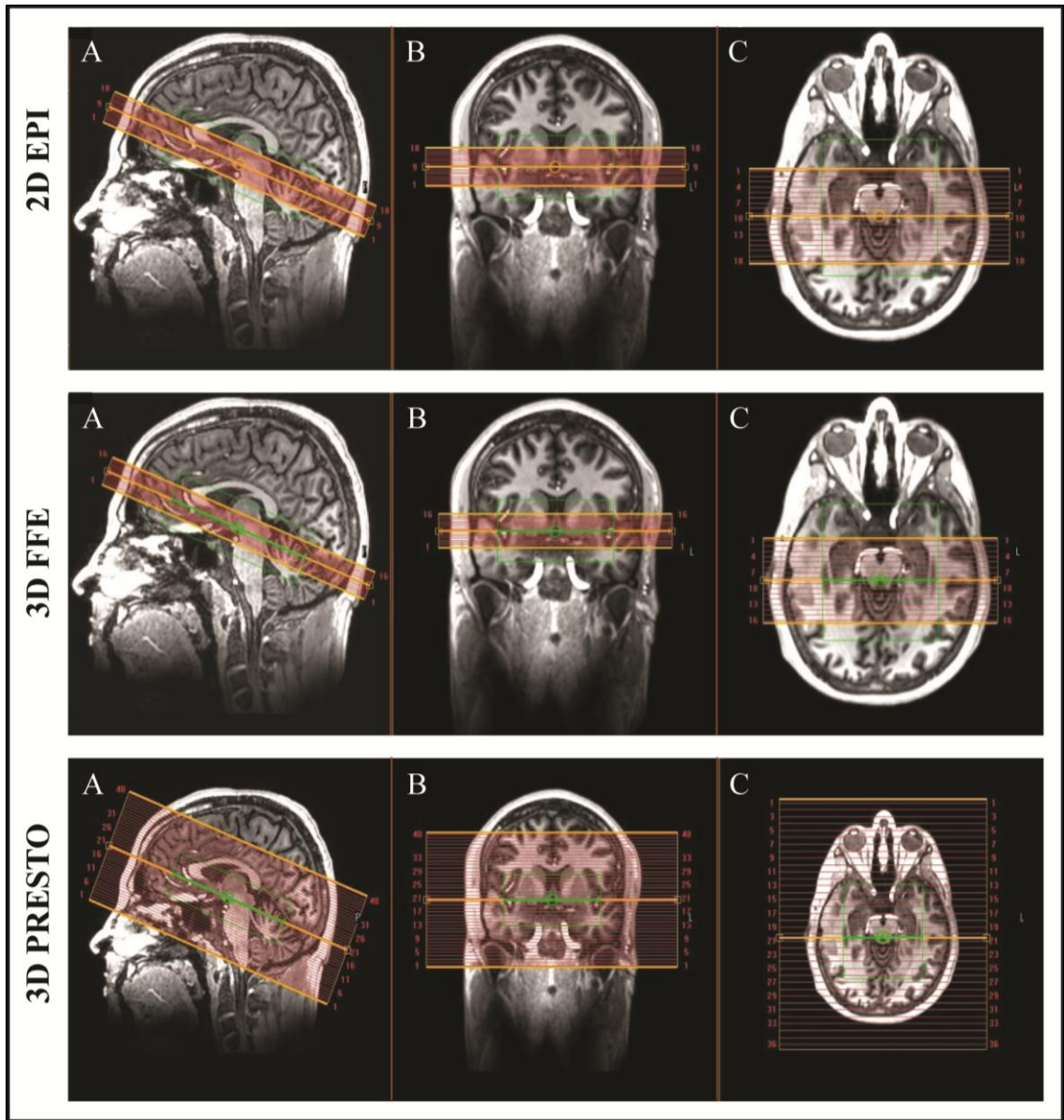
Figure 22: **Slice orientation and positioning for EPI, FFE and PRESTO fMRI sequences.** 2-D EPI (top row), 3-D FFE (middle row) and 3-D PRESTO (bottom row) are shown here. **A**, The sagittal plane. **B**, The coronal plane. **C**, The axial plane. The yellow-orange bounding box represents the slice slab and the smaller green box represents the shim volume.

For the initial set of five participants who were scanned using the FFE sequence, only the magnitude data were retained after image reconstruction. These FFE images had an FOV = 170 (AP) x 170 (RL) x 21.28 (FH) mm, reconstruction matrix = 128 x 128, SENSE factor = 3.1 in the RL direction, TR (time between shots) = 25 ms, TE = 17 ms, volume acquisition time or dynamic scan time = 2.0 s, voxel resolution =1.33 mm x 1.33 mm x 1.33 mm, with 16 slices and FA = 15°. Image volumes were acquired in runs of 12 min and 24.5 s duration, with 372 volumes per run. Each participant completed up to 3 runs of a slow event-related fMRI design. A task was administered during this scan, so the onset of each run was triggered from the scanner such that the fMRI data collection and the stimulus presentation were synchronized.

For the next set of scans reported, the real and imaginary data were retained after magnitude reconstruction to allow separate calculations of magnitude and phase images. An additional set of five participants were imaged on the FFE sequence. These FFE images had an FOV = 220 (AP) x 170 (RL) x 21.28 (FH) mm, reconstruction matrix = 164 x 127, SENSE factor = 3.1 in the RL direction, TR (time between shots) = 25 ms, TE = 17 ms, volume acquisition time or dynamic scan time = 2.0 s, voxel resolution =1.34 mm x 1.34 mm x 1.33 mm, 16 slices and FA = 15°. Image volumes were acquired in runs of 12 min and 50.4 s duration, with 372 volumes per run. Each participant completed up to 3 runs of a slow event-related fMRI design. A task was administered during this scan, so the onset of each run was triggered from the scanner such that the fMRI data collection and the stimulus presentation were synchronized.

The single-shot EPI sequence had the following imaging parameters: FOV = 220 (AP) x 190 (RL) x 23.94 (FH) mm, reconstruction matrix = 164 x 140, SENSE factor = 3 in the RL direction, TR (volume acquisition time or dynamic scan time) = 2.0 s, TE = 24 ms, voxel resolution = 1.34 mm x 1.34 mm x 1.33 mm with zero gap, 18 slices and FA = 75°. Image volumes were acquired in an oblique axial orientation in runs of 12 min and 48 s duration, with 372 volumes per run. The participant completed 3 runs of a slow event-related fMRI design in this sequence. A task was administered during this scan, so the onset of each run was triggered

from the scanner such that the fMRI data collection and the stimulus presentation were synchronized. A B_0 map was also acquired using two gradient echo sequences at different TEs to potentially correct for imaging distortions using an in house distortion correction algorithm.

The multi-shot PRESTO sequence had the following imaging parameters: FOV = 240 (AP) x 220 (RL) x 100 (FH) mm, reconstruction matrix = 96 x 85, SENSE factor = 2.4 in the RL direction and 1.5 in the FH direction, TR (time between shots) = 18 ms, TE = 26 ms, volume acquisition time or dynamic scan time = 2.0 s, voxel resolution = 2.50 mm x 2.56 mm x 2.50 mm, 40 slices and FA = 10°. Image volumes were acquired in an oblique axial orientation in runs of 12 min and 45 s duration, with 372 volumes per run. The participant completed 3 runs of a slow event-related fMRI design in this sequence. A task was administered during this scan, so the onset of each run was triggered from the scanner such that the fMRI data collection and the stimulus presentation were synchronized.

The resting state scans had the same parameters as the task scans, except with fewer dynamics (200 dynamics). Two runs were collected for each sequence type in every individual. The duration of the EPI scans was 7 min and 4 s, the duration of the FFE scans was 7 min and 1 s and the duration of the PRESTO scans was 7 min and 1 s.

Physiological monitoring equipment

The participant's pulse rate was monitored using a finger peripheral pulse unit (PPU) that interfaced with the scanner. It was placed on the left middle or index finger of each participant. The participant's respiration was monitored using a respiratory belt placed around the abdomen or sternum area. The location was chosen based on the region that exhibited largest motion during normal breathing. This belt also interfaced with the scanner. Both the PPU and the respiration physiological component measurements were sampled at 500 Hz and stored in a log file during each scan session.

PE-MID Experimental design

Details of the original MID task have been published previously (Knutson, Westdorp et al. 2000). In our version of the MID, participants had the opportunity to win or lose money by pressing a button during a very brief presentation of a visual target stimulus (Figure 23). Each PE-MID task run consisted of sixty 10-14 second trials. During each trial, participants were shown one of six cues (cue phase, 2 s), indicating that they had the potential to win money (WIN trials; amount = +$2 or +$5; n = 24), lose money (LOSE trials; amount = -$2 or -$5; n = 24), or neither win nor lose (NEUTRAL trials; +$0, -$0, n = 12). Participants then fixated on a cross-hair during a variable interval (anticipatory delay phase, 1000–2000 ms) and responded to a white star symbol target that appeared for a variable length of time (target phase, average of 328 ms) with a button press. For WIN trials, participants were told that if they successfully pressed the button while the target was onscreen (a "hit") they won the amount of money indicated by the cue, while there was no penalty for failing to press the button (a "miss"). For LOSE trials, participants were told that no money was won or lost for hits (pressed button while the target was on the screen), but misses led to a loss of the amount indicated by the cue for that trial.

Another delay period followed this target phase during which the participants again fixated on a cross-hair for a variable interval (outcome anticipatory phase, 1740-2840 ms). This was presented after the target disappeared and before the outcome screen appeared. A feedback screen (outcome phase, 2000 ms) then appeared notifying participants how much money they won or lost during that trial. In order to incorporate the prediction error into the task, the magnitude of the outcome varied such that the participants received the amount indicated on the cue screen with a probability of 66%. Thus, the overall outcome amount varied from $1-$3 and $4-$5 in the win and loss trials. Prediction error was not implemented for the $0 amount cues. This established a framework of manipulating prediction error, which the DA neurons are known to be sensitive to.

A variable inter-trial interval of 2 - 6 seconds separated each trial. Thus, each trial was between 5-7 TRs in length, facilitating a slow event-related jittered fMRI design. fMRI volume acquisitions were synchronized to the onset of each cue. Although no money was at stake during the NEUTRAL trials, participants were instructed to rapidly press the button during the display of the target stimulus. Before entering the scanner, participants completed a practice version of the task and were instructed that they would get to keep 20% total earnings by performing the task successfully. Based on reaction times obtained during the pre-scan practice session, target durations were adjusted such that each participant succeeded on approximately 66% of his or her responses. Each PE- MID task session was comprised of 3 functional runs, each approximately 12.41 min long.

The PE-MID was programmed in E-Prime Professional (version 2.0: Psychology Software Tools Inc.) and implemented from a dedicated Pentium computer in the scanner control room. The visual display was presented on an LCD panel and back-projected onto a screen positioned at the back of the magnet bore. Subjects lay supine in the scanner and viewed the display through reflective mirror lenses. Manual responses were recorded using a keypad (Rowland Institute of Science, Cambridge MA) secured to the right hand.
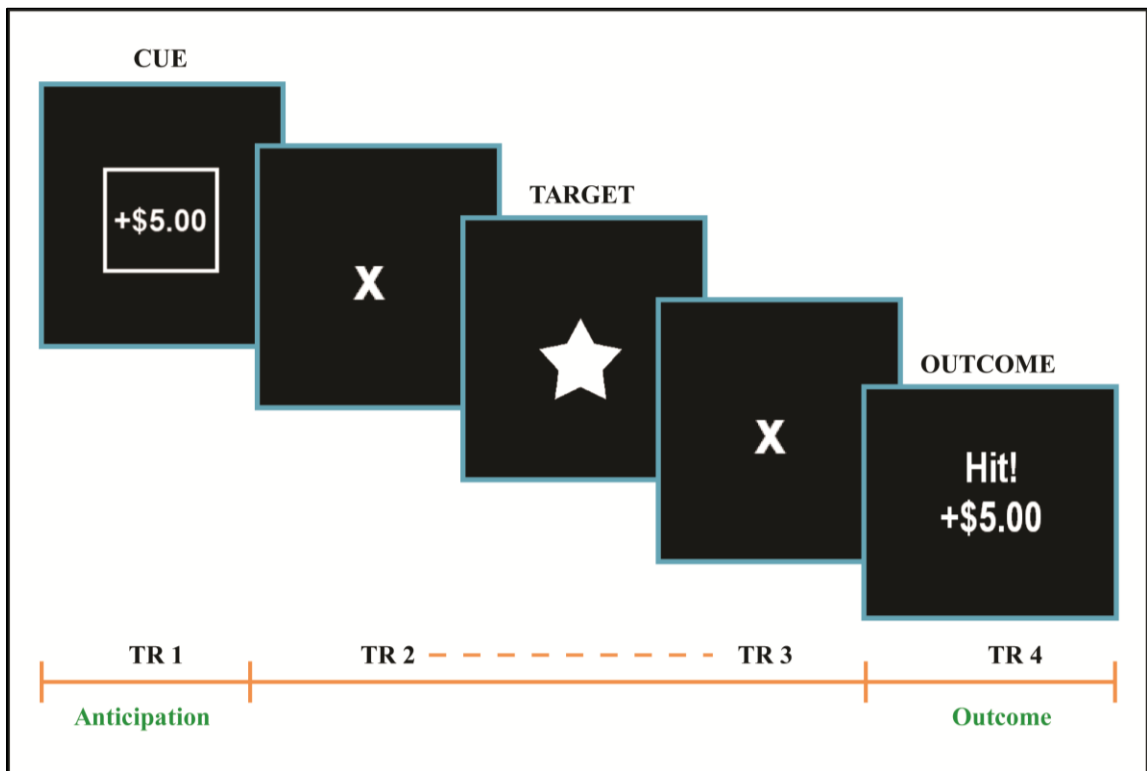
Figure 23: **Visual representation of the PE-MID task outlining different parts of a single trial.** Cue values changed between +$0,+ $2, +$5, -$0, -$2 and -$5. TR = 2 seconds. 'X' denotes the variable inter-stimulus delay. The star symbol denotes the target period during which the participants have to make a button response. TR refers to repletion time. The outcome interval was followed by 2- 6 seconds of delay. Every trial was 5-7 TRs in length.

fMRI data analysis

Functional images were corrected for participant head motion and analyzed using
Statistical Parametric Mapping (SPM5; Wellcome Department of Imaging Neuroscience,
University College, London, UK). All the EPI scan sequences were slice time corrected and put
through the RETROICOR algorithm (modified version of the algorithm (Glover, Li et al. 2000)).
The FFE and PRESTO scans are 3-D multi-shot sequences and all lines of k-space are not
acquired in a single-shot. Therefore, scan time correction is inappropriate as a pre-processing step
for these scans. Instead, after motion correction, the FFE and PRESTO sequences were directly
run through the RETROICOR algorithm. The RETROICOR technique was implemented in house
using Matlab (version R2010a, MathWorks, Natick, Massachusetts) and is based on Glover and
colleague's (Glover, Li et al. 2000) original algorithm (Courtesy of Dr. Rob Barry).

For the fMRI scans in which the PE-MID task was incorporated, a general linear
regression model (GLM) was used to analyze the data. For the data of the five participants, who
completed the initial FFE scans with the PE-MID task, a smoothing filter of 3 mm full-width-
half-maximum (FWHM) Gaussian kernel was applied followed by a high-pass filter (128 s
cutoff) to remove low-frequency signal drift. The 3 mm smoothing was applied on masked fMRI
data constrained to the basal ganglia and the midbrain. The GLM analysis in this approach was
also constrained to the basal ganglia and the midbrain areas. Therefore we assumed that it would
improve the individual subject fMRI statistics. Each participant's data were inspected for
excessive motion and only subjects with <1.5 mm motion in every direction across all runs were
included in the analyses.

Single-subject SPMs

All win, loss and neutral trials (across similar monetary values) were pooled. Onsets for
the following regressors were separately modeled using a canonical hemodynamic response
function (HRF). These ten regressors include: onsets of the cue phase of each trial type (+$0, +$2,

110

+$5, -$0, -$2, -$5), onsets of positive outcome, negative outcome, positive prediction error and

negative prediction error. For the task-related fMRI scan, we were primarily interested in

examining BOLD response in the midbrain during two intervals: the initial anticipatory period

(modeling anticipation to reward) and the interval after the outcome is presented (modeling

response to outcome and prediction error). Thus, we examined the BOLD response associated

with the following contrasts: gain anticipation (+$2, +$5 > +$0), loss anticipation (-$2, -$5 > -

$0), positive prediction error (outcome associated with +$2, +$5) and negative prediction error

(outcome associated with -$2, -$5). These contrasts have been previously reported to activate the

midbrain and ventral striatum in 3 T neuroimaging group studies (Knutson, Westdorp et al. 2000;

Buckholtz, Treadway et al. 2010). Each run was modeled separately. Each participant's data was

individually examined at an uncorrected voxel level threshold of $p < 0.05$.

Calculating percent signal change for task-related contrasts of interest

Region of interest (ROI) masks for the VTA and SN were drawn on the functional

dataset. After the single subject GLM analysis was performed, we extracted the average BOLD

response within midbrain structures for the various contrasts of interest (con images in SPM). The

SPM con images represent the overall BOLD response in the ROIs relative to a global mean

baseline for different contrasts of interest. The SPM GLM analysis also calculates the mean

signal for each run (constant beta term). The percent signal change was calculated by dividing

contrast of interest con images with the mean signal con image and multiplying the result by 100.

The midbrain structures included in this analysis were left SN, right SN, left VTA and the right

VTA.

Estimating TSNR

ROI masks for the VTA and SN were drawn on the functional dataset. Once the fMRI

analysis was completed, the SPM mean signal for each run and the residual mean square

(unexplained noise variance) were extracted from each of the ROI masks. Then to calculate the

TSNR in the ROI, the mean signal was divided by the square root of the noise variance. For the

resting state scans, we calculated the mean signal in every voxel and the standard deviation (SD)

in every voxel over time. TSNR was then determined in every voxel by taking the calculated

mean signal and dividing it by the calculated SD value across all time points. ROI masks of the

SN and VTA were drawn in the mean signal fMRI data. These masks were used to extract the

TSNR in an ROI by taking the mean of the TSNR in the voxels falling within the ROI.

Calculating time course correlations between ROIs

Three dimensional ROI masks were drawn on the functional dataset for the VTA, SN and

white matter (WM). The white matter in the midbrain refers to the cerebral peduncles adjacent to

the SN and this area can have a similar cardiac pulsatility profile to the midbrain DA regions

(therefore suggesting greater temporal correlation, but not functional correlation). The SN, VTA

and WM ROIs were drawn on the functional dataset for each sequence type in both the task-

related and resting state scans. The masks were then used to extract the time course in the ROI

from each functional dataset. Pearson correlations between the time courses of different ROI pairs

were then performed in SPSS (IBM SPSS Inc. release 19).

Additionally, partial correlations were performed for each functional dataset in which

temporal correlations between the SN and VTA were estimated by accounting for the shared

variance in the neighboring midbrain WM. This would offer us additional information of the

correlations only between the midbrain DA regions excluding global effects that also affected the

neighboring WM.

Results

In one participant, we observed task-related activation in the midbrain for the contrasts of interest at a low uncorrected voxel level threshold of $p < 0.02$ (Figure 24). There were voxels in the VTA and SN that showed a modest relationship to the stimulation paradigm, but failed to reach acceptable significance levels in their magnitude and extent. Additionally, there were activation voxels near the arterires surrounding the midbrian, most likely representing false positives (observed in Figure 24, panel B).
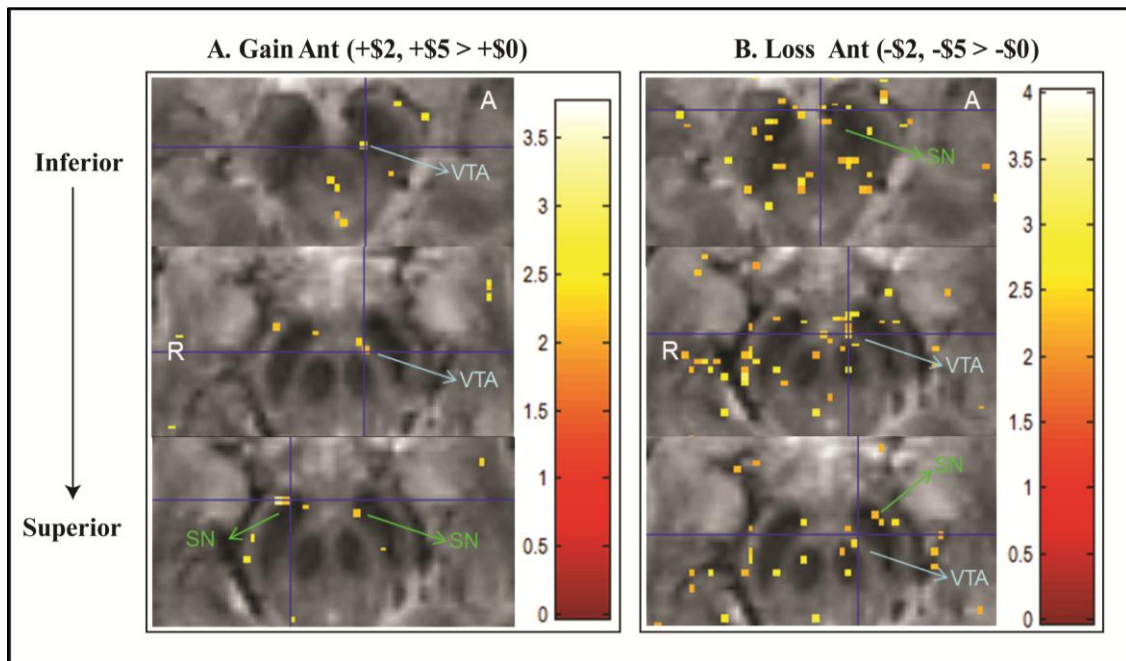
Figure 24: **Midbrain BOLD activation map in a single participant in the FFE sequence.** Two different contrasts of interest are represented here. Panel **A** shows the **Gain Anticipation** contrast (+$2, +$5 > +$0), and panel **B** shows the **Loss Anticipation** contrast (-$2, -$5 > -$0). Color bar represents a t-statistic. Voxel level threshold is set to an uncorrected $p < 0.02$. Within each panel, slices are ordered from inferior to superior. **A** = Anterior part of the brain; **R** = right part of the brain. Arrows point to the midbrain SN (substantia nigra) and VTA (ventral tegmental area). Results are shown for a single participant.

In the initial set of five FFE scans, the task-based BOLD response maps revealed only sparse activations in the midbrain DA areas. These activations were not consistent across individuals and we also observed activations outside the midbrain, possibly indicative of false positives (Figure 25). These results held true for the latter five FFE scans as well (results not shown here).
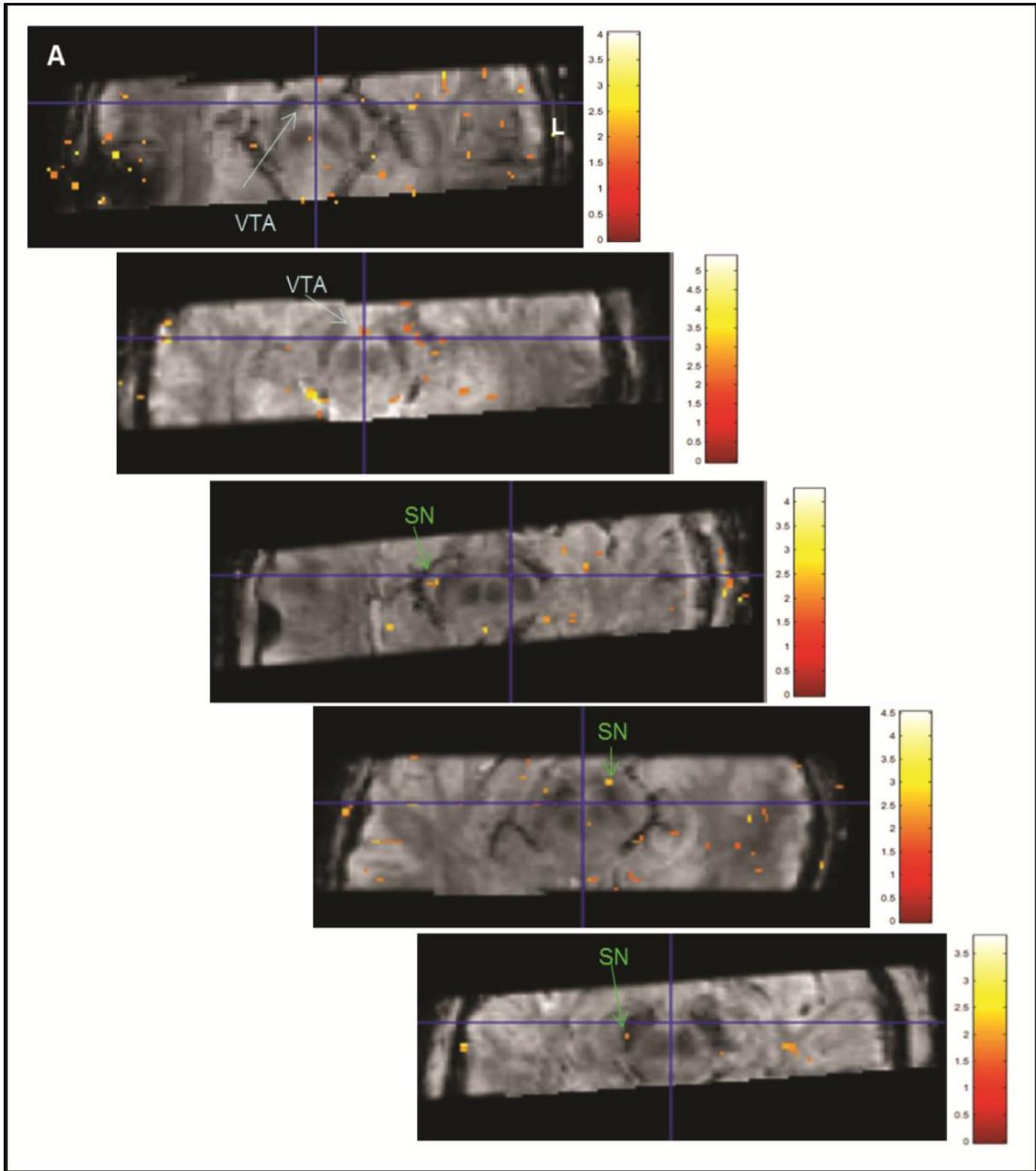
Figure 25: **Midbrain BOLD activation maps in five participants in the FFE sequence.**
Results are shown for the **Gain Anticipation** contrast (+\$2, +\$5 > +\$0). Color bar represents a t-statistic. Voxel level threshold is set to an uncorrected $p < 0.05$. **A** = Anterior part of the brain and **L** = left part of the brain. Arrows point to the midbrain SN (substantia nigra) and VTA (ventral tegmental area). Slices represented in axial orientation at the level of the red nuclei and the superior colliculi.

We smoothed this initial set of FFE scans using a 3 mm full-width-half-maximum (FWHM) Gaussian kernel and constrained the GLM analysis to a masked dataset covering only the midbrain and the basal ganglia. We hoped to observe reductions in false positives and an improvement in the strength of BOLD responses. However, we did not see any robust clusters stand out for the different contrasts of interest (Figure 26). The TSNR did improve though with average values in the SN approximately = 24 and that in the VTA approximately = 31 (results not shown here). These values were double what we observed without smoothing (see Figure 30 for comparison).
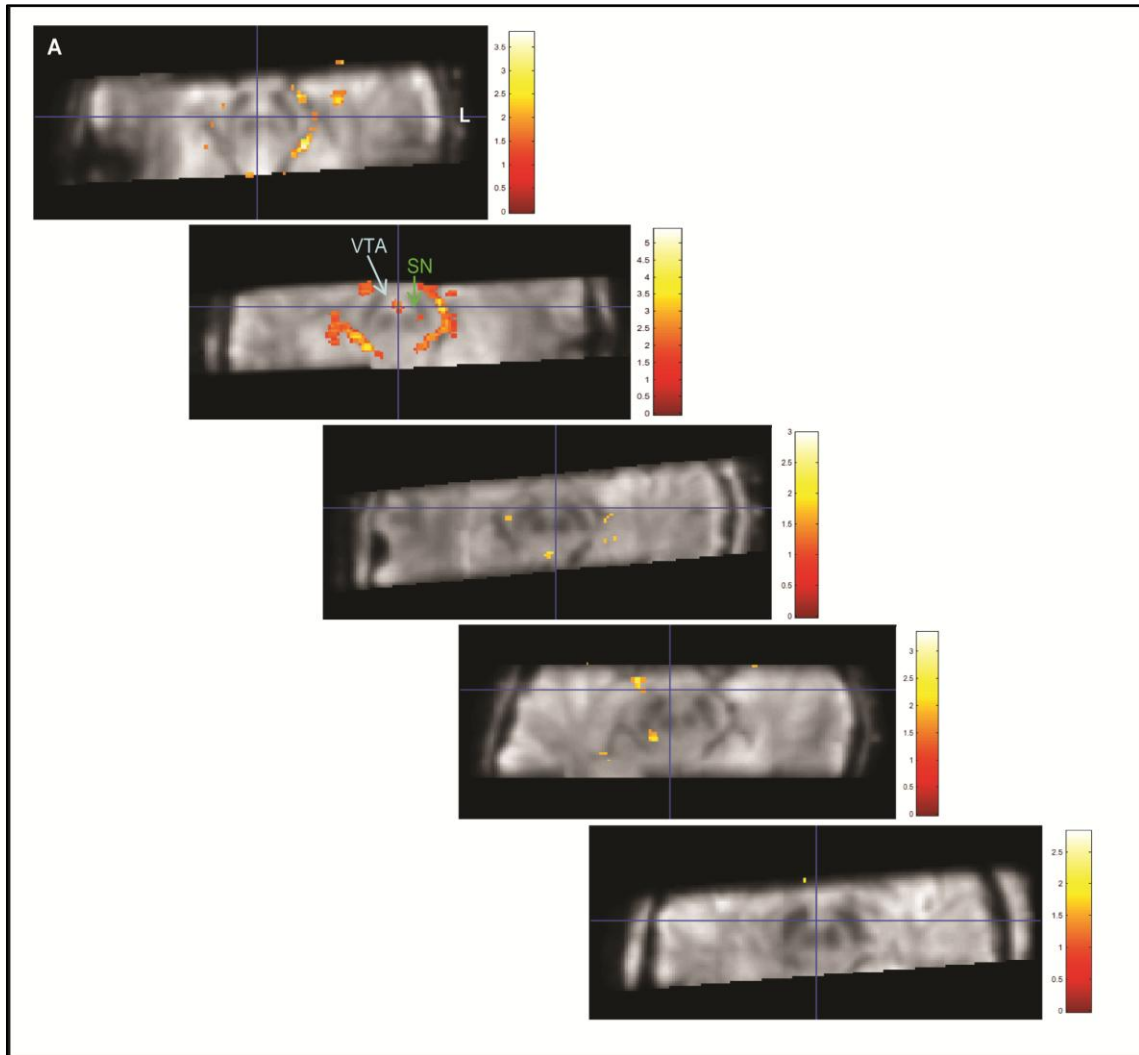
Figure 26: **Smoothed BOLD activation map in five participants in the FFE sequence.** 3 mm smoothed fMRI data are shown here for the **Gain Anticipation** contrast (+\$2, +\$5 > +\$0). Color bar represents a t-statistic. Voxel level threshold is set to an uncorrected $p < 0.05$. . **A** = Anterior part of the brain and **L** = left part of the brain. Arrows point to the midbrain SN (substantia nigra) and VTA (ventral tegmental area). Slices represented in axial orientation at the level of the red nuclei and the superior colliculi.

The activation maps for the EPI and the PRESTO data also demonstrated sparse activations in the midbrain that were inconsistent across individuals (EPI- Figure 27 and PRESTO – Figure 28).
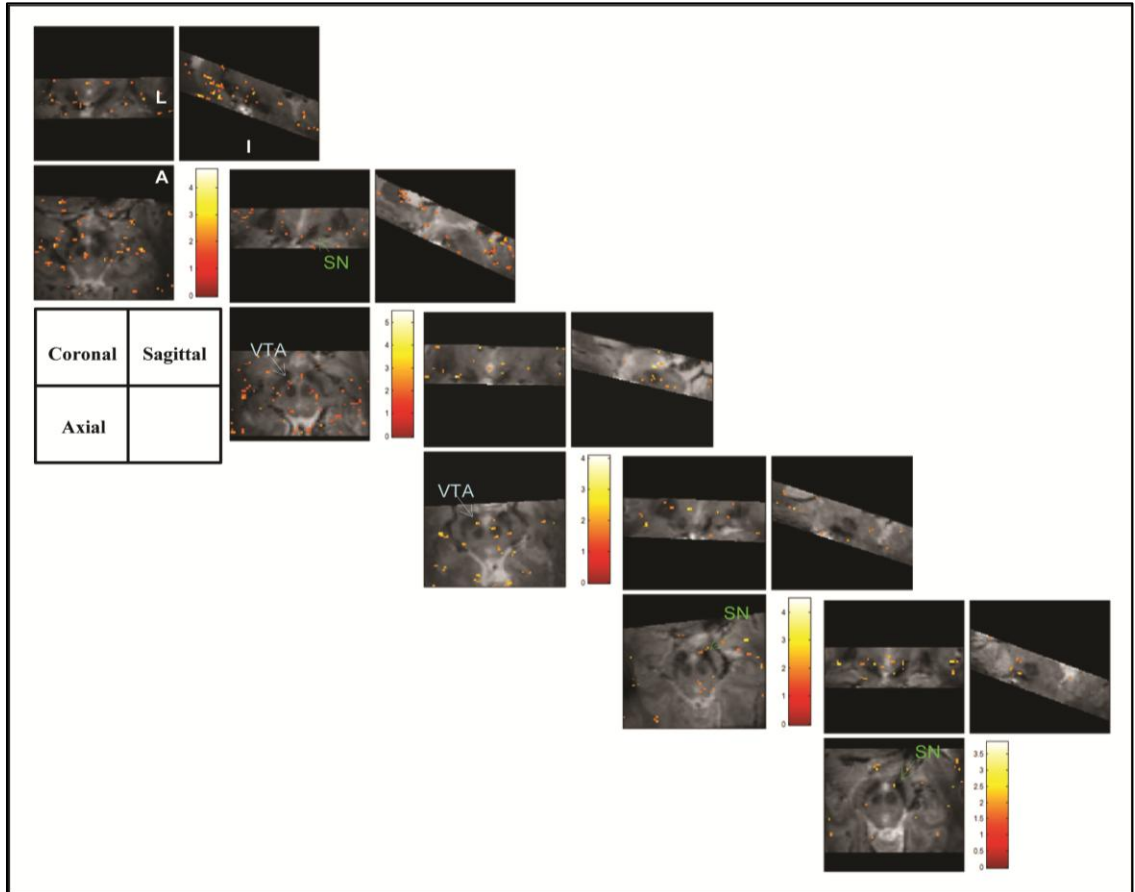
Figure 27: **Midbrain BOLD activation maps in five participants in the EPI sequence.** Results are shown for the **Gain Anticipation** contrast (+$2, +$5 > +$0). Color bar represents a t-statistic. Voxel level threshold is set to an uncorrected $p < 0.05$. **A** = Anterior part of the brain, **L** = left part of the brain and **I** = Inferior part of the brain. Arrows point to the midbrain SN (substantia nigra) and VTA (ventral tegmental area). Slices represent sections at the level of the red nuclei and the superior colliculi.
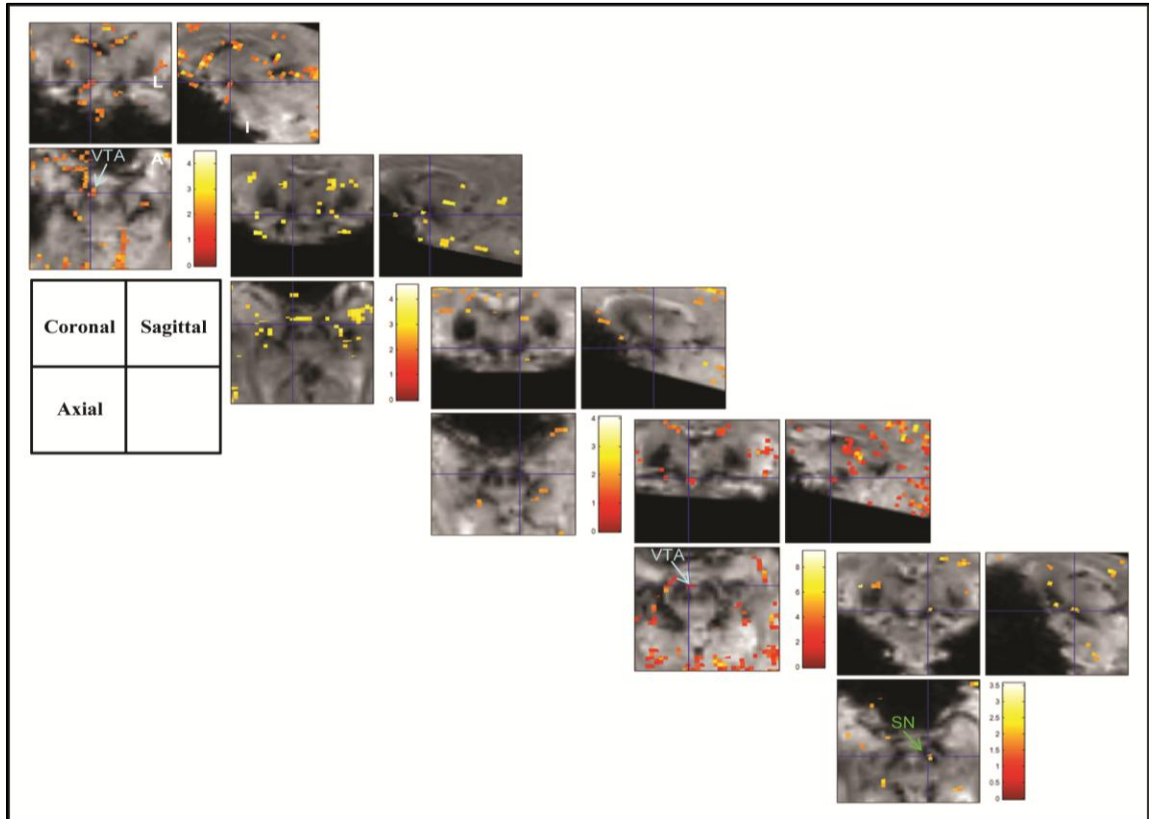
Figure 28: **Midbrain BOLD activation maps in five participants in the PRESTO sequence.**
Results are shown for the **Gain Anticipation** contrast (+$2, +$5 > +$0). Color bar represents a t-statistic. Voxel level threshold is set to an uncorrected $p < 0.05$. **A** = Anterior part of the brain, **L** = left part of the brain and **I** = Inferior part of the brain. Arrows point to the midbrain SN (substantia nigra) and VTA (ventral tegmental area). Slices represent sections at the level of the red nuclei and the superior colliculi.

We inspected the BOLD response to determine which contrasts were most sensitive in different midbrain regions. The percent signal BOLD responses for specific contrasts of interest measured potential activations without regard to noise levels. These were estimated for all datasets across the three different sequences, each with an N = 5 (Figure 29). The FFE data refers to the latter group of scans that had real and imaginary data retained after magnitude reconstruction. The contrast, anticipation > outcome, in the gain and loss conditions revealed the highest percent signal change across different sequences. Gain anticipation and loss anticipation demonstrated greatest percent signal change in the PRESTO sequence, particularly in the left and right SN. Across the EPI and FFE sequences (both of which had similar voxel resolutions), there was no consistency in the pattern of contrast responses within the SN and VTA. Positive and negative prediction error did not have a high percent signal change across all three sequences (< 0.5 %). When t-statistics were computed for different task-based contrasts of interest in the midbrain, the t-values were very low (< 1, results not shown here). These t-values account for noise variance in the data and they were consistently below 1 across participants, across contrasts of interest and across scan sequences.
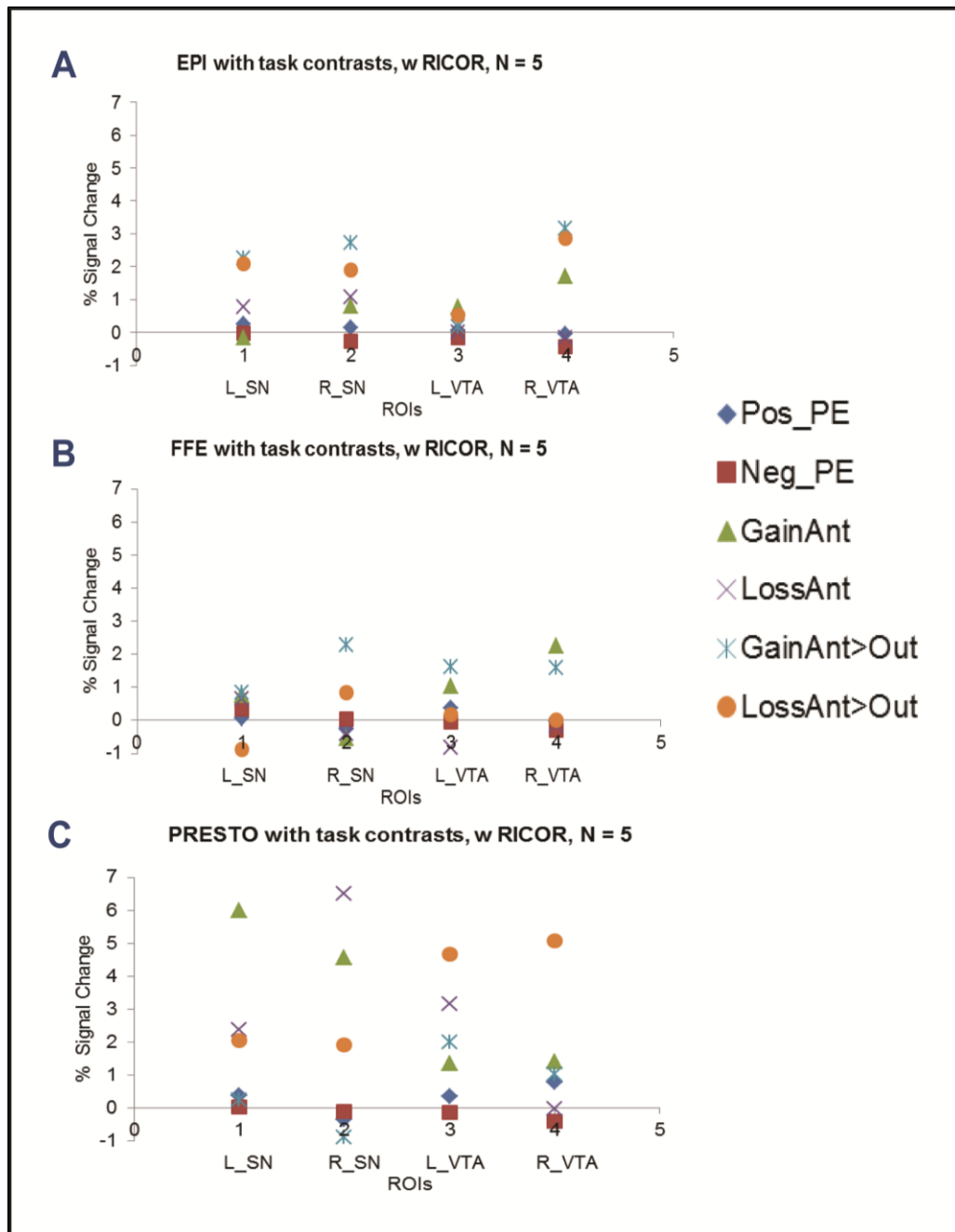
Figure 29: **Percent signal change for different contrasts of interest in the midbrain for EPI, FFE and PRESTO sequences.** Each sequence has N = 5. Panel **A** shows EPI data, panel **B** shows FFE data and Panel **C** shows PRESTO data. Contrasts refer to: Positive prediction error (Pos_PE), Negative prediction error (Neg_PE), Gain Anticipation (GainAnt), Loss Anticipation (LossAnt), Gain Anticipation > Gain Outcome (GainAnt>GainOut) and Loss Anticipation > Loss Outcome (LossAnt>LossOut). Regions of interest in the midbrain include left Substantia Nigra (L_SN), right Substantia Nigra (R_SN), left Ventral Tegmental Area (L_VTA) and right Ventral Tegmental Area (R_VTA). w RICOR denotes data with RETROICOR correction.

The TSNR in different sequences revealed a low signal in the midbrain SN across all sequences with task (Figure 30, panel A). Surprisingly, the VTA ROI in the EPI sequence had higher TSNR compared to the other sequences. Similar to the task-related fMRI scans, the resting state scans revealed a low TSNR pattern in the midbrain as well (Figure 30, Panel B).
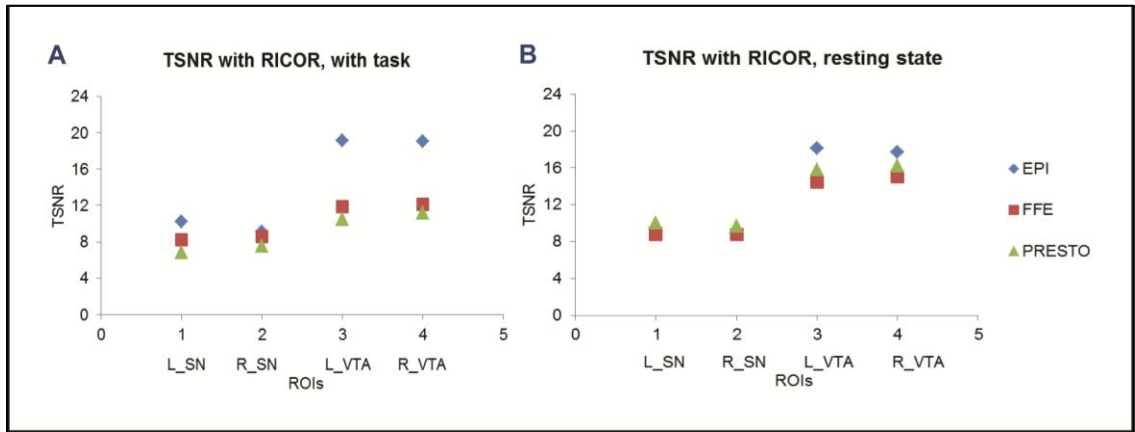
Figure 30: **TSNR in midbrain ROIs comparing EPI, FFE and PRESTO sequences in task and resting state scans.** Panel A indicates TSNR in the task-related scans across sequences with N = 5 in each sequence. Panel B indicates TSNR in the resting state scans across sequences with N = 6 in each sequence. Regions of interest in the midbrain include left Substantia Nigra (L_SN), right Substantia Nigra (R_SN), left Ventral Tegmental Area (L_VTA) and right Ventral Tegmental Area (R_VTA). RICOR refers to scans that have been analyzed with RETROICOR.

The Pearson correlation coefficients between fMRI data time courses for task-related scans revealed conflicting results across sequences (Table 5 and Figure 31). ROIs in the midbrain included the left Substantia Nigra (L_SN), right Substantia Nigra (R_SN), left Ventral Tegmental Area (L_VTA), right Ventral Tegmental Area (R_VTA), left White Matter (L_WM) and the right White Matter (R_WM). In the EPI scan, the mean correlation between the midbrain homologous ROI pairs were the following: L_SN: R_SN = 0.441, L_VTA:R_VTA = 0.372 and L_WM:R_WM = 0.045. In the FFE scan, the mean correlation between the midbrain homologous ROI pairs were the following: L_SN: R_SN = 0.273, L_VTA:R_VTA = 0.611 and L_WM:R_WM = -0.008. Finally, in the PRESTO scan, the mean correlation between the midbrain homologous ROI pairs were the following: L_SN: R_SN = 0.592, L_VTA:R_VTA = 0.686 and L_WM:R_WM = 0.486. These homologous pair correlations were higher than the non-homologous pairs for the 3-D FFE and PRESTO sequences. However, the non-homologous pair correlations were the same or higher compared to the homologous pairs for the EPI scan, suggesting an influence of temporal noise from the WM. The low statistical power (N = 5 in each sequence) prevented us from testing for significant differences in correlations.

Table 5: **Pearson correlations of temporal variance between midbrain ROIs.** Task and resting state scans are presented here. Correlations are between the average time courses in the respective ROIs. The homologous midbrain dopamine ROIs (SN and VTA) are highlighted in green. The homologous midbrain white matter ROI is highlighted in blue. ROIs denote SN, Substantia Nigra, VTA, Ventral Tegmental Area, and WM, White Matter.

Scan Type	Task	Rest		Task	Rest		Task	Rest
ROI pair	EPI	EPI		FFE	FFE		PRESTO	PRESTO
L_SN:R_SN	0.441	0.311		0.273	0.408		0.592	0.361
L_SN:L_VTA	0.506	0.263		0.023	0.131		0.401	0.135
L_SN:R_VTA	0.337	0.463		0.009	0.116		0.286	0.100
L_SN:L_WM	0.567	0.411		0.285	-0.061		0.502	0.251
R_SN:R_VTA	0.190	0.301		-0.224	-0.010		0.407	0.266
R_SN:L_VTA	0.281	0.376		-0.369	-0.049		0.333	0.128
R_SN:R_WM	0.119	0.286		0.075	0.142		0.464	0.379
L_VTA_R_VTA	0.372	0.371		0.611	0.599		0.686	0.614
L_VTA:L_WM	0.345	0.321		0.107	0.224		0.138	0.205
R_VTA:R_WM	0.505	0.275		0.139	-0.104		0.472	0.092
L_WM:R_WM	0.045	0.323		-0.008	0.352		0.486	0.470
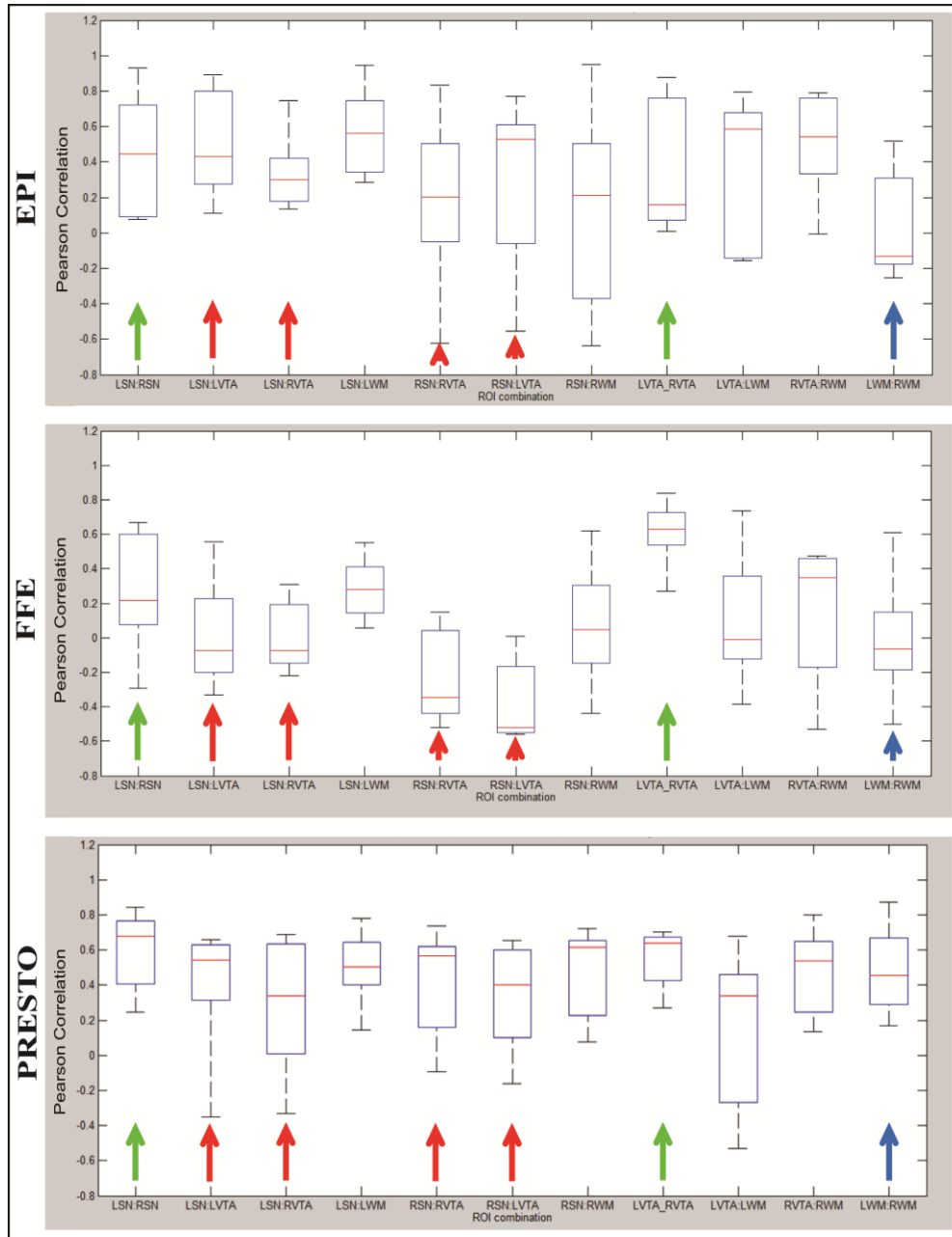
Figure 31: **Boxplot displaying Pearson correlations of temporal variance between midbrain nuclei for task-related scans.** The EPI (top row), FFE (middle row) and PRESTO (bottom row) are shown here. On each box, the central mark is the median, the edges of the box are the 25th and 75th percentiles, and the whiskers extend to the most extreme data points. The green arrows indicate correlations between homologous ROIs (L_SN:R_SN and L_VTA:R_VTA). The red arrows indicate correlations between non-homologous ROIs (L_SN:L_VTA, L_SN:R_VTA, R_SN:R_VTA and L_VTA:R_VTA). The blue arrow indicates correlations between the left and right white matter (L_WM:R_WM). ROIs denote SN, Substantia Nigra, VTA, Ventral Tegmental Area, and WM, White Matter.

Time course Pearson correlations in the fMRI data for resting state scans also revealed conflicting results (Table 5 and Figure 32). In the EPI scan, the mean correlation between the midbrain homologous ROI pairs were the following: L_SN: R_SN = 0.311, L_VTA:R_VTA = 0.371 and L_WM:R_WM = 0.323. In the FFE scan, the mean correlation between the midbrain homologous ROI pairs were the following: L_SN: R_SN = 0.408, L_VTA:R_VTA = 0.599 and L_WM:R_WM = 0.352. Finally, in the PRESTO scan, the mean correlation between the midbrain homologous ROI pairs were the following: L_SN: R_SN = 0.361, L_VTA:R_VTA = 0.614 and L_WM:R_WM = 0.470. Similar to the task scans, these homologous pair correlations were higher than the non-homologous pairs for the 3-D FFE and PRESTO sequences. However, in the EPI scans, the homologous pair correlations were indistinguishable from the non-homologous pairs, suggesting no implicit temporal correlation between the homologous midbrain regions. The low statistical power (N = 6 in each sequence) prevented us from testing for significant differences in correlations.
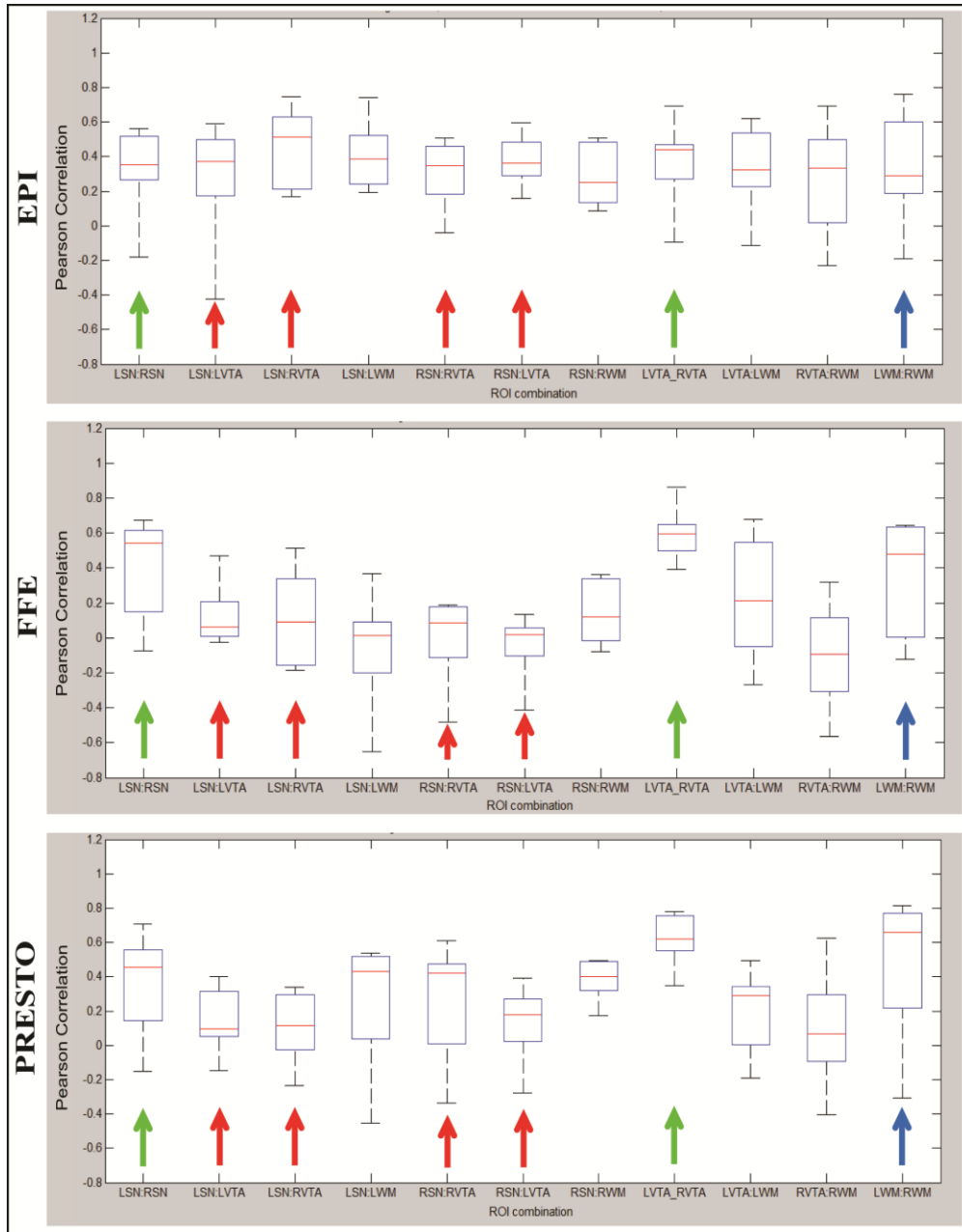
Figure 32: **Boxplot displaying Pearson correlations of temporal variance between midbrain nuclei for resting state scans.** The EPI (top row), FFE (middle row) and PRESTO (bottom row) resting state scans are shown here. On each box, the central mark is the median, the edges of the box are the 25th and 75th percentiles, and the whiskers extend to the most extreme data points. The green arrows indicate correlations between homologous ROIs (L_SN:R_SN and L_VTA:R_VTA). The red arrows indicate correlations between non-homologous ROIs (L_SN:L_VTA, L_SN:R_VTA, R_SN:R_VTA and L_VTA:R_VTA). The blue arrow indicates correlations between the left and right white matter (L_WM:R_WM). ROIs denote SN, Substantia Nigra, VTA, Ventral Tegmental Area, and WM, White Matter.

Partial correlations between the SN and VTA, accounting for shared variance with the white matter, revealed mixed results (Table 6). In both task and resting state EPI scans, the correlations between the homologous midbrain ROIs were not different from those seen in the non-homologous pairs. In the 3-D FFE scan however, the partial correlations demonstrated higher correlations in the homologous pairs compared to the non-homologous pairs. A similar pattern was seen for the PRESTO sequences. Interestingly, the homologous pair ROI correlations were higher in the resting state scan compared to the task scan for both 3-D sequences. The low statistical power (N = 5 in task scans and N = 6 resting state scans) prevented us from testing for significant differences in correlations.

Table 6: **Partial correlations of temporal variance between midbrain ROIs.** Partial correlations between midbrain ROIs are shown here accounting for shared temporal variance with neighboring white matter. Task scan and resting state scan correlation values are presented here. N = 5 in each task scan and N = 6 in each resting state scan. Values represent averages across runs and across participants. The homologous midbrain dopamine ROIs (SN and VTA) are highlighted in green.

Scan Type	Task	Rest	Task	Rest	Task	Rest
ROI pair	EPI	EPI	FFE	FFE	PRESTO	PRESTO
L_SN:R_SN	0.156	0.232	0.280	0.478	0.567	0.427
L_VTA:R_VTA	0.162	0.236	0.411	0.461	0.648	0.631
L_SN:L_VTA	0.159	0.177	0.169	0.053	0.285	0.038
L_SN:R_VTA	0.070	0.292	0.085	-0.025	0.214	0.012
R_SN:L_VTA	0.094	0.265	-0.041	0.032	0.295	0.123
R_SN:R_VTA	0.195	0.181	0.067	0.085	0.328	0.244

Discussion

In this study, we wanted to explore whether it was possible to detect task-related BOLD activations in the midbrain with any consistency across multiple participants. We implemented 2-D and 3-D sequences to observe differences across imaging protocols as well as voxel resolutions. A modified version of the monetary incentive delay task was used to activate the midbrain DA reward system. In addition, we collected resting state scans with the same imaging parameters as the task-based scans to compare the temporal correlations between midbrain DA regions with and without a task. We observed activation maps across individuals in each sequence type, measured BOLD percent signal changes for various contrasts of interest in specific midbrain ROIs, calculated TSNR in the midbrain ROIs across sequences and also evaluated time course correlations between the ROIs to determine functional connectivity patterns.

BOLD activation patterns

BOLD activation maps in the midbrain did not reveal significant or trend level responses for task-specific contrasts of interest (Figure 24). Prior studies using a similar task reported a large, smoothed activation cluster in the midbrain area for group results. Therefore, we did not know what to expect at the individual subject level at 7 T. With higher resolution scans and greater sensitivity to BOLD contrast at 7 T, we anticipated robust clusters of activation within the VTA and SN area. We attempted to parse out differential activity in the SN and VTA for task-specific contrasts of interest. However, we only observed a few activated voxels within the SN and VTA distinctly. We also observed likely false positives around the midbrain for these contrasts, decreasing our confidence in the ability to detect BOLD activation in the midbrain.

Across individuals and sequence types, activations maps demonstrated qualitative differences in the BOLD response of every individual. Sparse activations were observed in the

131

midbrain SN and VTA for a known task-specific contrast of interest (Gain Anticipation) at a low uncorrected voxel level threshold ($p < 0.05$). This contrast has been previously shown in similar fMRI paradigms at 3 T to activate the midbrain and ventral striatum during the anticipation of a rewarding cue compared to a neutral cue (Knutson, Westdorp et al. 2000; Knutson, Fong et al. 2003). The BOLD activations we observed in our study were thus not consistent across individuals within a certain scan sequence (Figure 25, 27, 28). Spurious activations were observed outside the midbrain, so we smoothed the data by 3 mm and constrained the fMRI analysis to solely the midbrain and basal ganglia regions. We assumed that this would reduce the presence of false positives in the data. However, even after smoothing, we did not observe a consistent pattern of activation (Figure 26). Such a result could mean that either the task was not powerful enough to robustly activate the midbrain or that there was noise within the data interfering with the ability of the GLM analysis to detect signal. We know that previous reward-based fMRI studies have reported task-based activations in the midbrain at lower field strengths (Berns, McClure et al. 2001; Bunzeck and Duzel 2006; D'Ardenne, McClure et al. 2008). Thus, we expected to detect at least some, if not greater sensitivity towards the stimulus at 7 T.

Percent signal change

Percent signal change measurements for individual midbrain ROIs revealed some task-specific contrast differences, although these differences were inconsistent across sequence types (Figure 29). Overall, the Gain Anticipation > Gain Outcome contrast demonstrated the most robust activation the midbrain areas across all sequences, but more so in the PRESTO sequence (4-5%). This suggests some sensitivity in the midbrain regions towards the anticipation of an outcome compared to the feedback of the outcome. Positive and negative prediction error contrasts did not show a high percent signal change in all three sequences (< 0.5%). This is surprising given the nature of the DA neuron response reported in non-human primate as well as human neuroimaging studies (Schultz 1998; Berns, McClure et al. 2001; D'Ardenne, McClure et

132

al. 2008). The Gain Anticipation contrast revealed a 1-2% signal change in the right VTA of the EPI and FFE scans in comparison to the other ROIs. However, in the PRESTO scan, the SN and VTA were both responsive to the Gain Anticipation contrast. The PRESTO scan was collected at a lower voxel resolution (2.5 mm isotropic), so it is possible that the signal strength may be more detectable at this resolution compared to the higher resolutions used in the EPI and FFE sequence. However, the BOLD activation maps did not show this on a consistent and significant scale (Figure 28) and the TSNR values did not reveal much difference across scan sequences (Figure 30). One thing to note is that percent signal change calculations do not account for noise variance in the data since it only measures the beta estimates with respect to the mean signal. When noise variance was taken into consideration in t-statistics calculations, the t-values were less than 1 for different task-based contrasts of interest in the midbrain across participants and across scan sequences. This implied a large influence of temporal variance in the data, reducing the strength of the observed task-based BOLD sensitivity.

We are unable to ascertain at this point if the differences in the task-based BOLD sensitivity within and across scan sequences were a result of reduced stimulation of the midbrain DA system. Another reason for the low signal detectability could be partial voluming effects due to the assumption that all the voxels in the ROI will be equally activated for a particular contrast of interest. We did not have an a priori hypothesis regarding which parts of the SN or VTA would selectively respond to one type of contrast, so we chose to use the entire ROI in the percent signal change analysis.

TSNR measurements

TSNR was quite low in the midbrain ROIs for both the task and resting state scans, suggesting a possible reason for the dearth of functional activity evidenced in our study (Figure 30). It is surprising that even the low resolution PRESTO scan had lower TSNR compared to the EPI sequence in the VTA ROIs. In a separate 3 T EPI study in which we ran the same fMRI

paradigm (at a voxel resolution of 1.88 x 1.88 x 2.5 mm^3), the TSNR in the SN was observed to be approximately five times larger at 3 T compared to 7 T. Furthermore, the TSNR in the VTA was three times more in the 3 T compared to the 7 T (results not shown here). This difference seems puzzling to interpret. While we know that there are differences between 3 T and 7 T (e.g., different receive coil sensitivity profile, B1 inhomogeneities, and faster T2* decay rate), the unreported results mentioned above imply some specific effect for these midbrain regions. 7 T studies have shown robust fMRI BOLD contrast in cortical visual areas (Barry, Strother et al. 2011), suggesting greater reliability for signal detection in these areas compared to subcortical areas. Although the T2 times at 7 T are shorter, this cannot account for substantial reductions in TSNR, so we conclude these reductions are caused by greater temporal variance in the MR signal in these regions. Moreover, the 7T with its increased sensitivity to BOLD effects may likely be more sensitive to such temporal variances within the midbrain compared to 3 T.

Potential functional connectivity patterns

One of the speculations we had was that the noise seen in the midbrain regions during our task-based fMRI scans was potentially driven by strong implicit functional correlations between midbrain ROIs which might be stronger between homologous in comparison to non-homologous pairs. In the EPI sequence, time course correlations between midbrain ROIs revealed no differences in the correlations between homologous ROIs compared the non-homologous pairs (Figures 31, 32 and Table 5). In fact strong correlations were observed between midbrain ROIs with their neighboring white matter ROI, suggesting shared temporal variance with an area that is not functionally correlated. This pattern was similar in the resting state EPI scan as well. In future studies, the white matter ROI can possibly be included as a regressor of no interest in the SPM GLM model to improve BOLD signal detectability. A recent 7 T fMRI study of the superior colliculus demonstrated a two-fold improvement in the t-statistics of the estimated data after a

regressor of no interest analysis was implemented using the anterior cerebellum (Krebs, Woldorff et al. 2010).

The midbrain ROI time course correlation revealed a different story for the 3-D sequences. The FFE scans demonstrated low-mid correlation effect for the homologous pairs compared to the non-homologous pairs in the task-based scan (Table 5 and Figures 31, 32). Moreover, the white matter ROI played a smaller role in influencing the connectivity pattern. A similar result was observed in the resting state scans with mid-high correlations between the homologous SN and VTA and low correlations between the white matter ROIs. This suggests that there are signal fluctuations in the SN and VTA regions (at least within the FFE scans) that covary across regions but only in functionally relevant ROIs. Further work must be attempted to test how the different acquisition parameters in the 2-D EPI and 3-D FFE are contributing to the observed signal difference.

The 3-D PRESTO sequence revealed a similar pattern of time course correlation to that of the FFE sequence (Table 5 and Figure 31, 32). The homologous SN and VTA had stronger correlations compared to the other ROI pairs. Additionally, the white matter ROI covaried more strongly in this sequence compared to the FFE. The resting state scans demonstrated a bigger difference between correlations for the homologous vs. non-homologous pairs, with less of an influence from the white matter. These results suggest that there are covarying signal fluctuations in the midbrain even though it may not be driving task-specific differences large enough to be detected by the GLM model.

The partial correlations between midbrain SN and VTA when accounting for the shared variance with the white matter showed improvements for both 3-D sequences in the rest and task-specific scans (Table 6). Interestingly, the differences in the partial correlations between the homologous compared to the non-homologous ROIs were stronger in the resting state scans than in the task-based scans. This suggests that the correlations in the resting state data can be interpreted more unambiguously without the confounding effects of task-related variance. In

135

contrast, there seemed to be a reverse effect for the 2-D EPI scans with a decrease in correlations between the left and right SN and VTA. This suggests that the EPI sequences are more influenced by the temporal variance in the white matter compared to the 3-D sequences. Image distortions observed in the EPI scans could likely be contributing to global signal inhomogeneities, thereby impeding sensitivity in the midbrain regions.

Overall, in the present study, we were able to test the same fMRI paradigm on three different acquisition modes to check for task-specific BOLD contrast in the midbrain across multiple participants. We failed to observe significant and trend level BOLD responses in the midbrain. TSNR was surprisingly low in the midbrain SN and VTA, indicating high levels of temporal variance. The analysis step that revealed the most promising result was the time course correlations between the midbrain ROI pairs. In 3-D sequences (for both task and resting state scans), this analysis demonstrated higher correlations between homologous midbrain pairs compared to the non-homologous pairs, suggestive of intrinsic functional connectivity patterns.

Conclusion

In conclusion, we were unable to detect significant task-related BOLD contrast across different imaging sequences, different voxel resolutions and across multiple participants. TSNR was low in the midbrain compared to 3 T studies suggesting a huge influence of the noise in the midbrain. Temporal noise correlations between midbrain nuclei demonstrated moderate-high correlations between midbrain ROIs during task-based as well as resting state scans for the 3-D sequences. This implies that the 7 T is sensitive to intrinsic connectivity patterns between midbrain ROIs, even though these patterns may not be driving task-specific differences that can be detected by the fMRI GLM analysis.

References

Barry, R., S. Strother, et al. (2011). "Data-driven optimization and evaluation of 2-D EPI and 3-D PRESTO for BOLD fMRI at 7 Tesla: I. Focal coverage." <u>NeuroImage</u> **55**(3): 1034-1043.

Berns, G. S., S. M. McClure, et al. (2001). "Predictability Modulates Human Brain Response to Reward." <u>The Journal of Neuroscience</u> **21**(8): 2793-2798.

Buckholtz, J. W., M. T. Treadway, et al. (2010). "Mesolimbic dopamine reward system hypersensitivity in individuals with psychopathic traits." <u>Nat Neurosci.</u> **13**(4): 419-421.

Bunzeck, N. and E. Duzel (2006). "Absolute Coding of Stimulus Novelty in the Human Substantia Nigra/VTA." <u>Neuron</u> **51**(3): 369-379.

D'Ardenne, K., S. M. McClure, et al. (2008). "BOLD Responses Reflecting Dopaminergic Signals in the Human Ventral Tegmental Area." <u>Science</u> **319**(5867): 1264-1267.

Glover, G. H., T.Q. Li, et al. (2000). "Image-based method for retrospective correction of physiological motion effects in fMRI: RETROICOR." <u>Magn Reson Imaging</u> **44**(1): 162-167.

Gruetter, R. (1993). "Automatic, localized in vivo adjustment of all first- and second-order shim coils." <u>Magn Reson Med.</u> **29**(6): 804-811.

Gruetter, R. and C. Boesch (1992). "Fast, Noniterative Shimming of Spatially Localized Signals. In Vivo Analysis of the Magnetic Field along Axes." <u>Journal of Magnetic Resonance</u> **96**(323-334): 323.

Knutson, B., G. W. Fong, et al. (2003). "A region of mesial prefrontal cortex tracks monetarily rewarding outcomes: characterization with rapid event-related fMRI." <u>NeuroImage</u> **18**(2): 263-272.

Knutson, B., A. Westdorp, et al. (2000). "FMRI Visualization of Brain Activity during a Monetary Incentive Delay Task." <u>NeuroImage</u> **12**(1): 20-27.

Krebs, R. M., M. G. Woldorff, et al. (2010). "High-field FMRI reveals brain activation patterns underlying saccade execution in the human superior colliculus." <u>PLoS One</u> **5**(1): e8691.

Pruessmann, K., M. Weiger, et al. (1999). "SENSE: sensitivity encoding for fast MRI." <u>Magn Reson Med.</u> **42**(5): 952-962.

Schneider, E. and G. Glover (1991). "Rapid in vivo proton shimming." <u>Magn Reson Imaging</u> **18**(2): 335-347.

Schultz, W., P. Dayan, et al. (1997). "A neural substrate of prediction and reward." <u>Science</u> **275**(5306): 1593-1599.

Schultz, W. (1998). "Predictive Reward Signal of Dopamine Neurons." <u>Journal of Neurophysiology</u> **80**: 1-27.

Shmuel, A., E. Yacoub, et al. (2007). "Spatio-temporal point-spread function of fMRI signal in human gray matter at 7 Tesla." <u>NeuroImage</u> **35**(2): 539-552.

CHAPTER VI

TECHNICAL CHALLENGES OF FUNCTIONAL IMAGING IN THE HUMAN MIDBRAIN DOPAMINE SYSTEM AT 7 T

Abstract

Functional MRI (fMRI) in the midbrain across individuals revealed low temporal signal to noise ratio (TSNR) in 2-D and 3-D sequences for both task and resting state scans (Chapter V). Additionally, we were unable to detect reliable and reproducible task-based blood oxygen level dependent (BOLD) contrast in the midbrain. The reason for the paucity of the signal in the midbrain is uncertain and requires further investigation. Various data acquisition and data analysis steps were explored in this study to better understand the cause of signal and noise differences in the fMRI data. Methods for examining noise sources including RETROICOR, phase regression and power spectrum maps localized in the respiratory and cardiac frequency domains revealed that physiological factors did not strongly influence noise within the midbrain more than elsewhere. A one-dimensional (1-D) phase navigator algorithm was also implemented to verify the influence of between shot phase errors in 3-D multi-shot FFE and PRESTO sequences. Methods for examining signal differences using a finite impulse response (FIR) method or a GLM analysis with regressors controlling for variance in the neighboring white matter as well as the anterior cerebellum did not demonstrate an improvement in the detectability of BOLD contrast. Finally, we attempted to calculate the steady state signal difference and the noise difference between the midbrain and cortex in resting state scans. This analysis revealed a small signal difference between the midbrain and the cortex, but a relatively large noise difference between the midbrain and the cortex. Thus, even though we are still unsure of the basis for the low TSNR in the midbrain, we are certain it is not being contributed by low signal, but

rather it appears to be driven by noise variations. These noise variations are not removed by conventional strategies nor do they correspond to known physiological sources. From the previous chapter of this thesis, we know that there are intrinsic fluctuations between the homologous midbrain ROIs (likely attributed to functional connectivity). It is possible that these fluctuations are being unaccounted for in our present analysis techniques and could therefore fall under the category of unexplained variance. Moreover, low frequency physiologic fluctuations (less than 0.1 Hz) associated with beat-to-beat cardiac pulsatility variations and breath-breath respiratory differences cannot be accurately resolved and reduced using standard noise correction algorithms. Further investigation must be undertaken to better understand the noise profile in the midbrain.

Introduction

As mentioned in Chapter V, fMRI based on task-based BOLD contrast has been unable to distinctly localize BOLD activity within the VTA or SN. While, high resolution MRI at 7 T appeared promising, work demonstrated in the last chapter established low BOLD signal detectability within the midbrain. There were limitations and challenges to imaging the subcortical midbrain in comparison to the cortex at 7T. In Chapter V, we observed that the midbrain had low TSNR explaining low signal detectability in the area. Moreover, fMRI based on a modified version of the monetary incentive delay task did not show task-specific BOLD variance in the midbrain VTA or SN for 2-D as well as 3-D pulse sequences. These findings were unreliable and irreproducible across participants. The source of the low TSNR is investigated in this study. To evaluate the extent of noise, we tested the contribution of two known physiological noise factors: cardiac pulsatility and motion associated with respiration. To evaluate signal integrity, we tested different fMRI analysis techniques to improve BOLD contrast detectability in the midbrain. Various techniques spanning the data acquisition, preprocessing and analysis stages

were assessed to ascertain the source of the low signal. Thus, the aim of this study was to evaluate the feasibility of these methods and discuss their limitations for functional imaging in the midbrain at 7 T.

Known sources of noise in the midbrain

There are various sources of noise in the midbrain including variations in partial volume effects, motion of cerebral spinal fluid (CSF) flow in the interpeduncular fossa (IPF), motion of the brainstem due to cardiac pulsatility in the arteries within and surrounding the midbrain, movements and changes in B_0 uniformity caused by chest movement induced by respiration and thermal noise associated with scanner electronics (Schroth and Klose 1992; Schroth and Klose 1992; Soellinger, Ryf et al. 2007; Yamada, Miyazaki et al. 2008). In addition to the contribution of cardiac and respiratory cycles, physiologic noise is also thought to include a BOLD element comprising hemodynamic and metabolic fluctuations in gray matter (Weisskoff 1996; Krüger, Kastrup et al. 2001). While the ratio between physiologic noise and thermal noise is supposed to increase with increasing field strength, moving toward higher spatial resolution at high field strengths has been shown to reduce this ratio, especially when TE is near T2* (Triantafyllou, Hoge et al. 2005). High noise reduces BOLD signal detectability and noise effects manifest themselves as image artifacts (distortion, ghosting, and multi-shot phase reconstruction errors) that vary within a slice, through the imaging volume and through time.

Techniques for mediating noise

There are several methods that may help alleviate noise sources. Here we briefly review the most prominent techniques for exploring and correcting noise in midbrain fMRI data.

RETROICOR

Glover and colleagues (Glover, Li et al. 2000) demonstrated the viability of utilizing a retrospective correction algorithm, RETROICOR, for removing quasi-periodic respiration and cardiac cycles in EPI data. This method assumes that the cardiac and respiratory variances do not overlap with the task-related variance. The RETROICOR technique was implemented in house using Matlab and is based on Glover and colleague's original algorithm (Courtesy of Dr. Rob Barry). The efficacy of this algorithm in the 7 T is also elaborated in Chapter IV of this dissertation.

Phase regression analysis

BOLD data driven by task-specific stimuli are often prone to contamination from large vessels which can impede localization of neural activity in high resolution fMRI studies. In order to remove the fraction of BOLD signal that arises from oriented vessels, a computational method is used to measure the influence of the phase angle from these vessels in the complex valued fMRI dataset and suppress BOLD signal changes from these large vessels and draining veins on a per-voxel basis (Menon 2002). In this analysis, blood vessels larger than the smallest intra-cortical veins (> 25 μm radius) are considered oriented, producing changes in both the magnitude and phase data during neural activation in comparison to vessels in the capillary beds that are typically randomly oriented, producing only magnitude changes. BOLD signal contributions from large vessels are estimated and removed using a maximum likelihood estimator from a linear least squares fit of the unwrapped phase to the magnitude time series (Menon 2002). In short, this technique suppresses noise sources that exhibit temporally correlated changes in both magnitude and phase data. These noise sources include blood flow changes in large vessels as well as motion associated with respiration.

The midbrain is highly vascularized with vessels sizes ranging from very small venules and arterioles up to approximately 100 μm in radius, and they perfuse the medio-lateral and

142

dorso-ventral extent of the midbrain (Naidich, Duvernoy et al. 2009). In cross sectional views of the midbrain, the vessels supplying the SN and VTA take on a geometric orientation with the arteries and veins (both parallel in their alignment to each other) running orthogonal to the SN and VTA. These arteries and veins belong to the internal anterolateral group of mesencephalic vessels (Figure 33). The suitability of the phase regression algorithm for reducing noise in the midbrain may have to be evaluated taking into consideration the oriented vasculature in the SN and VTA.

Figure 33: **Pictorial representation of vasculature in the midbrain at the level of the superior colliculus.** Reprinted with kind permission from Springer Science+Business Media: *Human Brain Stem Vessels*, from chapter, Arteries and Veins of the Brainstem, 2nd ed. Berlin, Germany: Springer-Verlag; 1999, page 81, Duvernoy HM, Figure 33a. Key midbrain regions are noted. **SN** = substantia nigra, **VTA** = Ventral Tegmental Area, **RN** = Red Nucleus and **CP** = Cerebral peduncles (white matter). Black colored blood vessels represent veins. Red, green and blue colored blood vessels represent arteries, (Duvernoy 1999).

1-D navigator during image acquisition to mediate multi-shot phase errors

3-D multi-shot scan sequences (PRESTO and FFE) can be susceptible to shot-shot phase errors. For the successful reconstruction of an entire imaging volume, all the shots (number of lines of k-space collected) associated with every slice need to be accurately combined together. If they are not accurately combined, ghosts are observed in the final image varying within the image (stationary ghosts) as well as across time (temporal ghosts). One way to correct for the shot – shot errors is to ensure that the phase information is maintained across shots. Versluis and colleagues (Versluis, Peeters et al. 2010) used a navigator echo to correct for phase changes associated with B_0 fluctuations. A navigator echo is collected for the center line of k-space before applying the phase encode gradients. This 1-D navigator provides an estimate of the phase projection along one dimension. For 3-D acquisitions, this represents a measure of phase offsets for the entire 3-D volume that is excited. When this technique was implemented in other imaging studies at 7 T, a two-fold improvement in resting state TSNR in the cortex was observed (unpublished, courtesy of Dr. Allen Newton). One of the disadvantages in using this approach is the assumption that phase variation is the same across all slices for a 3-D volumetric acquisition. This is untrue, particularly in the brainstem where B_0 field inhomogeneities can be observed as a result of motion from cardiac pulsations and respiration.

Power spectrum maps of the midbrain

Cardiac pulsatility and motion associated with respiration in the chest is known to introduce temporal instability in functional imaging data and can potentially hinder BOLD signal detectability (Guimaraes, Melcher et al. 1998; Dagli, Ingeholm et al. 1999). We estimated the degree of this temporal instability within the midbrain by examining the power spectra in the cardiac and respiratory frequencies. Using a very high temporal resolution scan (450 ms), data can be sampled fast enough to capture the cardiac (around 1Hz) and respiratory (around 0.25 Hz) frequencies. From these data, a spatial power spectrum map can be created in the cardiac and

respiratory frequency ranges to show the spatial distribution of power in the midbrain. This map then allows for the estimation of the percentage of noise in cardiac and respiratory frequencies with respect to the total noise in the data. Power spectrum density curves (as shown in Figure 22, Chapter III) can be also be created for different midbrain regions to observe the frequency peaks that are most prominent throughout the sampling period. This may help identify noise fluctuations in the data that are not part of the task frequency range.

Techniques for improving signal detection

The following section outlines possible methods for improving BOLD signal detection in the midbrain.

Regressors of no interest in the GLM analysis

Krebs and colleagues (Krebs, Woldorff et al. 2010) used the average time course from the anterior cerebellum (a region that is temporally, but not functionally correlated with the behavioral task) to perform a regressor of no interest analysis for functionally imaging the superior colliculus at 7 T. An improvement in the task-related t-statistics was demonstrated for the fMRI data. This method can be potentially advantageous because it makes no assumptions concerning the sources of noise in the data, and also attempts to remove all noise, whether physiological or technological in origin. To translate this approach for the midbrain, the cerebral peduncles (white matter area lateral to the SN) and the anterior cerebellum could be used. Both these regions represent areas that are not functionally correlated with the task and may have similar cardiac pulsatility profile to the ventral midbrain.

Using an optimal hemodynamic response function for the midbrain

Both the amplitude and shape of the Hemodynamic Response Function (HRF) have been observed to vary significantly across subjects, and across different brain areas (Aguirre, Zarahn et

146

al. 1998; Handwerker, Ollinger et al. 2004). Typical fMRI studies use a canonical HRF that peaks at 6 seconds as the statistical model for data analysis. However, this canonical HRF model may not be optimal for our studies. An optimized study of the superior colliculus at 3 T reported better signal sensitivity for an HRF that peaked at 4.5 seconds instead of one peaking at 6 seconds (Wall, Walker et al. 2009). The Finite Impulse Response (FIR) method is a standard way to characterize the shape of the HRF (Lindquist and D.Wager 2007) and this approach is explored as an alternative to detect signal in the midbrain.

Assessing signal difference between the midbrain and the cortex

In order to compare the magnitudes of the MR signal in the midbrain and the cortex, relevant imaging parameters (e.g., T1, TE, and T2*) must be evaluated for the midbrain and cortex. These values can be inserted into the appropriate steady state signal equation, which is

$$S\,(TE,\,TR) = S_0 * \frac{\sin\theta\,(1 - e^{(-TR/T1)})}{1 - \cos\theta\,(e^{(-TR/T1)})} * e^{(-TE/T2*)}$$

where TE = time to echo, TR = repetition interval, S_0 is the equilibrium signal, S is the steady state signal, T1 is the T1 value, T2* is the T2* value of the area and theta (θ) is the actual flip angle (calculated by multiplying the nominal flip angle with the measured normalized B1 maps in that area). This equation, in combination with measured signal values, allows the equilibrium signal, S_0, to be evaluated separately for the midbrain as well as the cortex. This equation can also be used across different fMRI imaging protocols (2-D EPI, 3-D FFE, and 3-D PRESTO) to estimate signal differences in the midbrain as well as the cortex (Haacke, Brown et al. 1999), page 455.

The present study attempted to explain the noise and the signal variability in fMRI data collected at 7 T.

<center>**Methods**</center>

Participants

Five healthy participants completed the FFE study with the task (5 males, mean age of participants = 26 years) and in this study only the magnitude data were recorded. For the following set of studies, both real and imaginary image data were retained after magnitude reconstruction. An additional five participants completed the FFE study with task (3 males, mean age of participants = 30.5 years). Five healthy participants completed the EPI study with task (3 males, mean age of participants = 31.2 years). Five healthy participants completed the PRESTO study with task (3 males, mean age of participants = 32 years). Six healthy participants completed the resting state fMRI scans that had EPI, FFE and PRESTO scans (4 males, mean age = 35.17 years).

For the following set of studies, only magnitude data were recorded. One healthy individual completed a study that collected high temporal resolution PRESTO and EPI data (male, 27 years of age). Two healthy individuals completed the study that collected imaging parameters to compare signal in the midbrain and the cortex (male, mean age of participants = 30.5 years). All participants provided written informed consent for the study, which was approved by the institutional review board of Vanderbilt University Medical Center. They were compensated $40 in addition to 20% of their total earnings in the PE-MID task. For scans that did not require a task, the participants were compensated $40.

fMRI data acquisition

Images were acquired using a 32 channel 7 T Achieva Scanner (Philips Healthcare, Cleveland, Ohio). Whole brain 3-D anatomical scans were acquired using a T1-weighted Turbo Field Echo pulse sequence for all scan sessions. 138 slices were collected in sagittal orientation with field of view (FOV) = 256 (FH) x 256 (AP) x 172.5 (RL) mm, reconstruction matrix = 204 x

<center>148</center>

204, parallel imaging factor (SENSE, (Pruessmann, Weiger et al. 1999)) = 2 in the AP direction, repetition time (TR) = 3.0 ms, echo time (TE) = 1.35 ms, voxel resolution =1.25 mm x 1.25 mm x 1.25 mm with zero gap, flip angle (FA) = 7°, acquisition time = 2 min and 12.2 s. This high resolution structural scan was used to determine the slice placement for the functional scans.

T2*- weighted BOLD images for all sequences described below were acquired in an oblique axial orientation with slices positioned to cover the dorso-ventral extent of the midbrain from the inferior edge of the caudate head to the dorsal border of the pons (Figure 22). The axial sections were tilted to make them parallel to a plane bisecting the mammillary body and the inferior frontal lobe. A volume shim was used for the 2-D single-shot EPI scans (Schneider and Glover 1991) and a pencil beam volume shim was used for the 3-D FFE and PRESTO scans (Gruetter and Boesch 1992; Gruetter 1993).

Task-based scans

The details of the task-based scans have been previously elaborated in the methods section of Chapter V.

Resting state scans with high TR and navigator patch

In order to characterize noise in the cardiac and respiratory frequencies, we collected very high temporal resolution resting state scans using PRESTO and EPI sequences. For the multi-shot PRESTO scans, a 1-D navigator was implemented to test differences between TSNR before and after shot-shot phase error correction. We also applied the navigator patch on a low TR FFE scan in order to compare results with the high TR scan.

The high temporal resolution single-shot EPI scans had the following imaging parameters: FOV = 220 (AP) x 172.86 (RL) x 8 (FH) mm, reconstruction matrix = 112 x 85, SENSE factor = 3 in the RL direction, TR (volume acquisition time or dynamic scan time) = 423 ms, TE = 20 ms, voxel resolution = 1.96 mm x 2.03 mm x 2.00 mm with zero gap, 4 slices and

FA = 28°. Image volumes were acquired in an oblique axial orientation in runs of 1 min and 38.6 s duration, with 200 volumes per run. The participant completed 2 runs of a resting state scan in this sequence.

When no navigator patch was applied, the PRESTO sequence had the following imaging parameters: FOV = 170 (AP) x 170 (RL) x 16 (FH) mm, reconstruction matrix = 84 x 82, SENSE factor = 2.0 in the AP direction, TR (time between shots) = 12 ms, TE = 19 ms, volume acquisition time or dynamic scan time = 346 ms, voxel resolution = 2.02 mm x 2.07 mm x 2.0 mm, 8 slices and FA = 10°. All image volumes were acquired in an oblique axial orientation in runs of 1 min and 43.1 s duration, with 265 volumes per run. The participant completed 2 runs of a resting state scan in this sequence.

When the navigator patch was applied, the PRESTO sequence had the following imaging parameters: FOV = 170 (AP) x 170 (RL) x 12 (FH) mm, reconstruction matrix = 96 x 96, SENSE factor = 2.0 in the AP direction, TR (time between shots) = 15 ms, TE = 22 ms, volume acquisition time or dynamic scan time = 360 ms, voxel resolution =2 mm x 2 mm x 2 mm, 6 slices and FA = 10°. All image volumes were acquired in an oblique axial orientation in runs of 1 min and 47.2s duration, with 265 volumes per run. The participant completed 2 runs of a resting state scan in this sequence.

When no navigator patch was applied, the FFE sequence had the following imaging parameters: FOV = 170 (AP) x 170 (RL) x 21.28 (FH) mm, reconstruction matrix = 128 x 127, SENSE factor = 3.1 in the RL direction, TR (time between shots) = 25 ms, TE = 17 ms, volume acquisition time or dynamic scan time = 2.0 s, voxel resolution =1.33 mm x 1.33 mm x 1.33 mm, 16 slices and FA = 15°. All image volumes were acquired in an oblique axial orientation in runs of 5 min and 4.8 s duration, with 150 volumes per run. The participant completed 2 runs of a resting state scan in this sequence.

When the navigator patch was applied, the FFE sequence had the following imaging parameters: FOV = 170 (AP) x 170 (RL) x 21.28 (FH) mm, reconstruction matrix = 128 x 128,

SENSE factor = 3.1 in the RL direction, TR (time between shots) = 25, TE = 17, volume acquisition time or dynamic scan time = 2 s, voxel resolution =1.33 mm x 1.33 mm x 1.33 mm, 16 slices and FA = 15°. All image volumes were acquired in an oblique axial orientation in runs of 5 min and 5.9 s duration, with 150 volumes per run. The participant completed 2 runs of a resting state scan in this sequence.

Resting state scans comparing midbrain and visual cortex

For measuring the signal difference between the midbrain and the cortex, the following series of scans were implemented. These scans allowed us to calculate imaging parameters including fMRI mean, noise and TSNR, T2* values, initial signal from a multi-echo scan, T1 maps as well as B1 maps. All the sequences described below were acquired in an oblique axial orientation with slices positioned to cover the dorso-ventral extent of the midbrain from the inferior edge of the caudate head to the dorsal border of the pons. The axial sections were tilted to make them parallel to a plane bisecting the mammillary body and the inferior occipital lobe.

The single-shot EPI scans had the following imaging parameters: FOV = 220 (AP) x 172.86 (RL) x 17.6 (FH) mm, reconstruction matrix = 112 x 85, SENSE factor = 3 in the RL direction, TR (volume acquisition time or dynamic scan time) = 446 ms, TE = 18 ms, voxel resolution = 1.96 mm x 2.03 mm x 2.00 mm with zero gap, 8 slices and FA = 28°. Image volumes were acquired in an oblique axial orientation in runs of 1 min and 38.6 s duration, with 200 volumes per run. The participant completed 2 runs of a resting state scan in this sequence.

The PRESTO sequence had the following imaging parameters: FOV = 223.46 (AP) x 173 (RL) x 17.6 (FH) mm, reconstruction matrix = 88 x 85, SENSE factor = 2.0 in the AP direction and 1.3 in the FH direction, TR (time between shots) = 16 ms, TE = 24 ms, volume acquisition time or dynamic scan time = 440 ms, voxel resolution =1.97 mm x 2.58 mm x 2.20 mm, 8 slices and FA = 10°. All image volumes were acquired in an oblique axial orientation in runs of 1 min

and 42.3 s duration, with 200 volumes per run. The participant completed 2 runs of a resting state scan in this sequence.

The FFE sequence had the following imaging parameters: FOV = 170 (AP) x 170 (RL) x 21.28 (FH) mm, reconstruction matrix = 128 x 127, SENSE factor = 3.1 in the RL, TR (time between shots) = 26 ms, TE = 17 ms, volume acquisition time or dynamic scan time = 2.0 s, voxel resolution = 1.33 mm x 1.33 mm x 1.33 mm, 16 slices and FA = 15°. All image volumes were acquired in an oblique axial orientation in runs of duration 5 min and 28.9 s, with 150 volumes per run. The participant completed 2 runs of a resting state scan in this sequence.

A multi-echo 3-D FFE scan was performed to acquire a T2* map. The imaging parameters for this scan included: FOV = 240 (AP) x 199.2 (RL) x 26.4 (FH) mm, reconstruction matrix = 400 x 330, SENSE factor = 2 in the RL direction and 1.2 in the FH direction, TR (time between shots) = 45 ms, TE1 = 4.6 ms, ΔTE = 3 ms, voxel resolution = 0.6 mm x 0.6 mm x 1.20 mm, 22 slices and FA = 10°. The scan duration was 3 min and 16.4 s.

A B1 map was created using a series of 11 single-slice gradient recalled echo (GRE) images acquired at flip angles ranging from 10° to 210° in 20 degree increments, with TR and TE, respectively, set to 6000 ms and 6.8 ms. The B1 maps scan had the following imaging parameters: FOV = 240 (AP) x 192 (RL) x 147 (FH) mm, reconstruction matrix = 64 x 77, voxel resolution = 3 mm x 3.12 mm x 3 mm, and 49 slices. The scan duration was 7 min and 54.1 s for each scan. The signal is calculated using the following formula: **Si = b * |sin (λ * a0i)|** with b representing the product of the received RF field (B1-) and the initial magnetization (M0) and lambda(λ) indicating the ratio of the actual transmitted RF field magnitude (B1+) with the nominal flip angle a0i of the i'th image in the series. A least-squares fit of the parameters b and lambda to the S vs. a0 curve for each voxel in the imaging slice results in a measure of lambda (i.e., the relative magnitude of the B1+ field) (Hornak, Szumowski et al. 1988) .

A B$_0$ map was collected to do distortion correction of the images used for the B1 map (since those scans were EPI). It had the following imaging parameters: FOV = 240 (AP) x 192

(RL) x 165 (FH) mm, reconstruction matrix = 64 x 80, no SENSE acceleration, TR = 4.1 ms, TE = 1.63 ms, voxel resolution = 3 mm x 3 mm x 3 mm, 55 slices and FA = 10°. The scan duration was 35.6 s.

A T1 map was made using inversion recovery scans. Each inversion recovery scan had a different inversion delay prior to signal acquisition. Both magnitude and phase of the signal were recorded. Data used to generate inversion recovery time series for 7 time points (100 ms, 200 ms, 400 ms, 800 ms, 1600 ms, 3200 ms, and 5000 ms). The inversion recovery scans had the following imaging parameters: FOV = 240 (AP) x 192 (RL) x 26 (FH) mm, reconstruction matrix = 160 x 121, TR = 8000 ms, T1 varies from 100 ms to 5000 ms, voxel resolution = 1.5 mm x 1.5 mm x 2 mm, and 9 slices. The scan duration was 3 min and 44 s for each scan. The time series from these scans were fit using the inversion recovery signal equation:

M = M0 * (1- (1 - cos(α)) * e$^{(-TI/T1)}$) where M0, alpha (α, the flip angle of the inversion pulse), and T1 are the fit parameters. TI is the inversion delay.

A T2-weighted GRASE scan was performed at the same resolution as the T1 maps in order to aid in drawing ROI masks. The T1 maps did not have enough contrast to delineate between structures of interest in the midbrain.

Physiological monitoring equipment

The participant's pulse rate was monitored using a finger peripheral pulse unit (PPU) that interfaced with the scanner. It was placed on the left middle or index finger of each participant. The participant's respiration was monitored using a respiratory belt placed around the abdomen or sternum area. The location was chosen based on the region that displayed largest motion during normal breathing. This belt also interfaced with the scanner. Both the PPU and the respiration physiological component measurements were sampled at 500 Hz and stored in a log file during each scan session.

PE-MID Experimental design

Details of the PE-MID task have been elaborated in the methods section of Chapter V.

fMRI data analysis

Functional images were corrected for participant head motion and analyzed using Statistical Parametric Mapping (SPM5; Wellcome Department of Imaging Neuroscience, University College, London, UK). All the EPI scan sequences were slice time corrected and put through the RETROICOR algorithm (modified version of the Glover *et al.*, 2000 algorithm). The FFE and PRESTO scans are 3-D multi-shot sequences, and all lines of k-space are not acquired in a single-shot. Therefore, scan time correction is inappropriate as a pre-processing step in these scans. Instead, after motion correction, the FFE and PRESTO sequences were directly run through the RETROICOR algorithm. The RETROICOR technique was implemented in house using Matlab (version R2010a, MathWorks, Natick, Massachusetts) and is based on Glover and colleague's (Glover, Li et al. 2000) original algorithm (Courtesy of Dr. Rob Barry).

For the fMRI scans in which the PE-MID task was incorporated, a general linear regression model (GLM) was used to analyze the data. Each participant's data were inspected for excessive motion and only subjects with <1.5 mm motion in every direction across all runs were included in the analyses.

Single-subject SPMs

Details of the PE-MID data analysis have been elaborated in the methods section of Chapter V.

Estimating TSNR

Region of interest (ROI) masks for the VTA and SN were drawn on the functional dataset. Once the fMRI analysis was completed, the SPM mean signal for each run and the

residual mean square (unexplained noise variance) were extracted from each of the ROI masks. Then to calculate the TSNR in the ROI, the mean signal was divided by the square root of the noise variance. For the resting state scans, we calculated the mean signal in every voxel and the standard deviation (SD) in every voxel over time. TSNR was then determined in every voxel by taking the calculated mean signal and dividing it by the calculated SD value across all time points. ROI masks of the SN and VTA were drawn in the mean signal fMRI data. These masks were used to extract the TSNR in an ROI by taking the mean of the TSNR in the voxels falling within the ROI.

Phase regression analysis

Real and imaginary data were retained during data acquisition. These were combined to produce magnitude data. A 2-D rigid body motion correction was implemented on these magnitude data to estimate translational and rotational motion parameters. The motion correction parameters were then applied to the original real and imaginary data. These motion corrected real and imaginary data were then combined to produce new motion corrected magnitude and phase data. Linear, quadratic and cubic polynomial detrending were applied to the motion corrected magnitude and phase data. This was followed by phase regression analysis on a voxel wise basis to remove the influence of BOLD effects produced by large vessels (detailed method in (Menon 2002; Barry, Williams et al. 2010)).

1-D navigator to correct for multi-shot phase errors

In this technique, a navigator echo is collected for the center line of k-space before applying the phase encode gradients. This 1-D navigator provides an estimate of the phase projection along one dimension. For 3-D acquisitions, this represents a measure of phase offsets for the entire 3-D volume that is excited. During the reconstruction stage, this global phase value is then subtracted from phase information in all lines of k-space. This was applied for the resting

state high temporal resolution PRESTO sequence and for the low temporal resolution FFE sequence.

Power spectrum maps in the cardiac and frequency ranges

From the high temporal resolution PRESTO and EPI sequences, we were able to sample the data fast enough to capture the cardiac and respiratory frequencies. For all the imaging slices acquired, we calculated spatial power spectrum maps in the cardiac and respiratory frequency ranges separately and estimated the percent noise in the cardiac and respiratory frequency ranges. This provides an estimate of the noise contribution in the cardiac and respiratory frequencies with respect to the total noise in the data.

Implementing a regressor of no interest analysis

Three dimensional ROIs in the cerebral peduncles (white matter, WM) located adjacent to the SN and the anterior cerebellum (ACb) posterior to the superior colliculus were used for this analysis. We extracted the average time course in these regions (method described in (Krebs, Woldorff et al. 2010)) and performed a slice- by-slice Pearson correlation analysis between the average time course in the WM, the ACb and the average time course in the VTA as well as the SN. This procedure helped verify that these regions were temporally correlated. Both the left and right WM average time courses were included as a regressor of no interest along with the other PE-MID task regressors for the full brain GLM SPM analysis. A separate analysis was performed in a similar way using the left and right ACb ROIs. The FFE data we had obtained on our initial five participants was used for this analysis. These five datasets were motion corrected and included in the regressor of no interest analysis with and without RETROICOR. Our assumption was that the variance in the WM and ACb may explain some of the noise variance in the SPM analysis and therefore be regressed out in the GLM, resulting in a better estimate of the BOLD activity in the VTA and SN.

Estimating optimal HRF in the midbrain

In this approach the onset times of the six different cues (+$0; +$2, +$5; -$0; -$2,-$5) were included in the SPM FIR analysis for the initial five participant FFE dataset. We combined the response in the $2 and the $5 monetary categories because the BOLD response for the positive rewards was assumed to be similar. Seven sample points per trial, each 2 s apart, corresponding to the volume acquisition time were used. This was performed over three runs for every single participant. Hence there were a total of 84 regressors that SPM had to estimate (4 cue types x 7 sample points x 3 runs). This approach provided BOLD response information for the entire 14 second window of our trial, allowing enough time for the HRF to rise and fall with respect to the onset of the cue phase. SPM estimated the signal associated with a specific cue type for each of the seven time points beginning from the onset of the cue. We made the assumption that all trials were 14 s (or 7 TRs long). For the shorter trials, however, this FIR analysis estimated the last two time points (sample points at TR 6 and 7) differently taking into account the overlap that may happen with the next cue onset. Thus every time point in the trial had a parameter estimate and time points that fell in between trials (overlapping events) were estimated by accounting for this overlap. We were most interested in capturing the time to peak for the HRF with respect to the cue onset. The SPM FIR is calculated for all voxels in the brain, across events of the same type. We extracted ROIs in the VTA and SN to observe the average HRF shape over the 7 sample points. For statistical testing, we ran a region of interest FIR analysis on the VTA and SN average time series and computed the F statistic for the overall model fit.

Results

For the task-based fMRI scans, the SN or VTA exhibited very little improvement in the TSNR when RETROICOR or phase regression analyses were used (Figure 34).
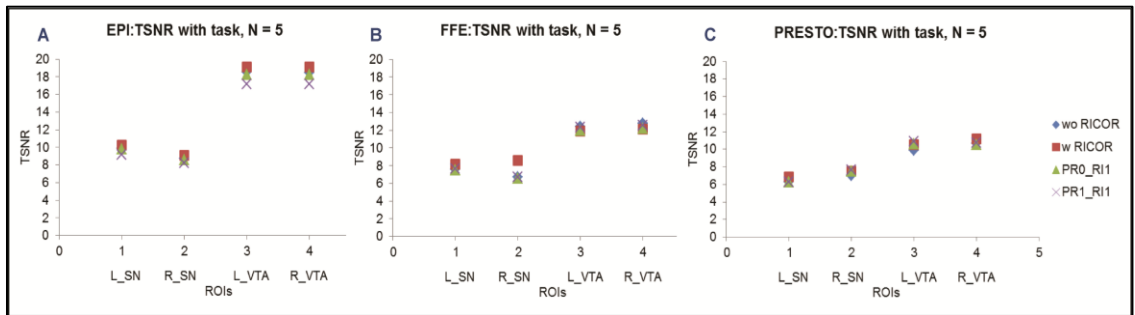
Figure 34: **TSNR in EPI, FFE and PRESTO sequences comparing different analysis methods.** Panel **A** 2-D EPI, panel **B**, 3-D FFE and panel **C**, 3-D PRESTO. Analysis techniques are: wo RICOR = without RETROCIOR, w RICOR = with RETROCIOR, PR0_R1 = no phase regression with RETROCIOR, and PR1_R1 = phase regression with RETROCIOR. Average of N = 5 in each sequence.

Using the 1-D navigator patch, we observed a decrease in the TSNR estimation in the midbrain for the high TR PRESTO scan (Figure 35). The TSNR, however, improved marginally in the midbrain for the low TR FFE sequence. Overall, the TSNR in the midbrain was low in both sequences (8-20 range for the SN and VTA, compared to 35-45 range for the cortex).
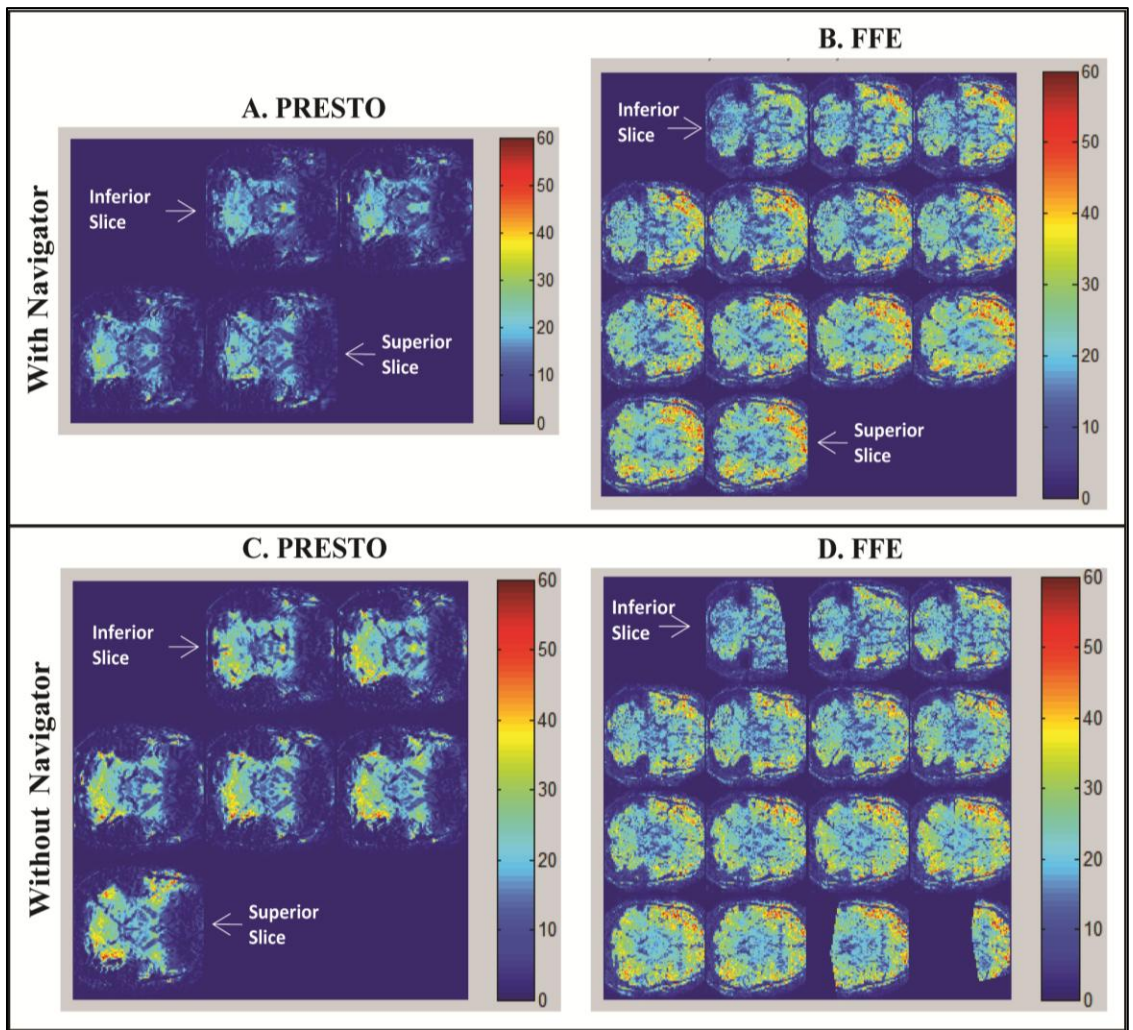
Figure 35: **Spatial TSNR maps with and without the use of a 1-D phase navigator.** Left column shows the PRESTO sequence and the right column shows the FFE sequence. Top row shows the data with the navigator and the bottom row shows the data without the navigator. Color bar indicates TSNR.

From the high temporal resolution PRESTO and EPI sequences, we examined the noise estimate (power spectrum map) in the midbrain area with respect to the noise in the entire frequency range (Figure 36). For the PRESTO sequence within the cardiac frequency range, the noise power spectrum maps revealed noise concentrated around the midbrain region, particularly in areas of CSF flow, within the IPF and areas surrounding the lateral aspects of the midbrain (Figure 36, Panel B). In fact, there was greater contribution of noise in the cardiac frequencies compared to the respiratory frequencies. This noise did not decrease even after the RETROICOR algorithm was applied (results not shown here). Although the PRESTO sequence exhibited a high concentration of noise in the midbrain, this was not localized specifically in the SN and VTA regions. EPI power spectrum maps revealed a different result with less concentration of noise power in the middle of the brain in both the respiratory and cardiac frequencies (Figure 36, panel C, D). Noise was not centered, however, in the midbrain regions of interest.
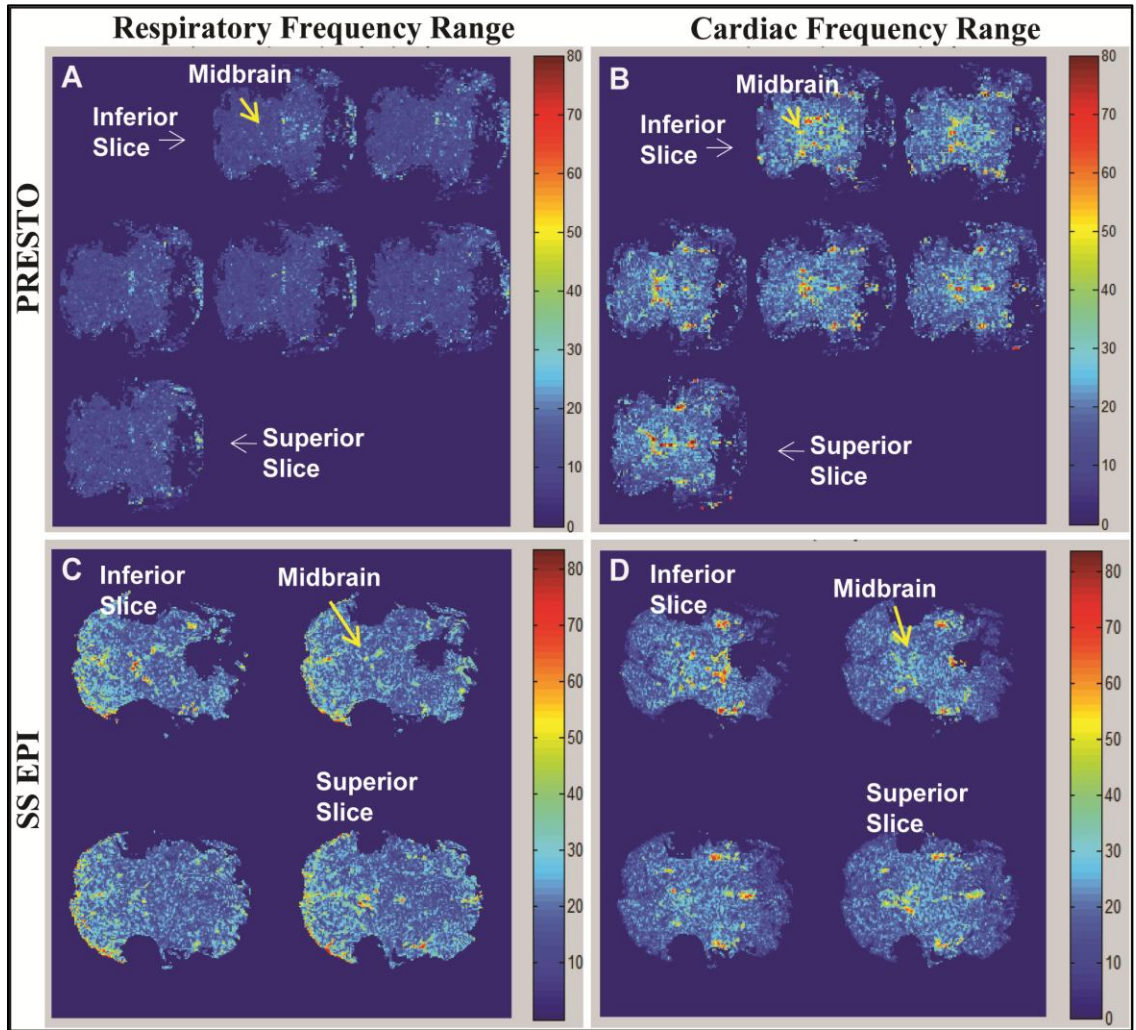
Figure 36: **Spatial power spectrum maps of the noise levels in midbrain area within the respiratory and cardiac frequency ranges.** Color scale indicates percentage of noise in the respiratory and cardiac frequencies with respect to total noise in the brain. The midbrain is located in the middle portion of these cross sectional maps (Anterior is to the right in these maps). Power spectrum maps in the midbrain for high TR PRESTO (Panel A, B) and EPI (Panel C, D) scans sequences. The respiratory frequency range is shown in the left column and the cardiac frequency is shown in the right column.

The regressor of no interest analysis was performed to measure an improvement in the signal within the midbrain for the initial set of five FFE participants. The average time course of the WM (white matter) ROI was not highly correlated with the average time course within the VTA and SN (average Pearson correlation, SN:WM = 0.260; VTA:WM = 0.174). As a result, the fMRI data analysis with this WM regressor did not improve the t-statistics for the task-related contrasts. The TSNR was very low, ranging from 8-10 for the SN and 12-15 for the VTA (Figure 37). The time series data in the ACb (Anterior cerebellum) ROI was more highly correlated with the midbrain than the WM ROI (average Pearson correlation, SN:ACb = 0.273; VTA:WM = 0.334). Similar to the WM ROI, using the ACb ROI as a regressor of no interest in the GLM analysis did not yield significant results.
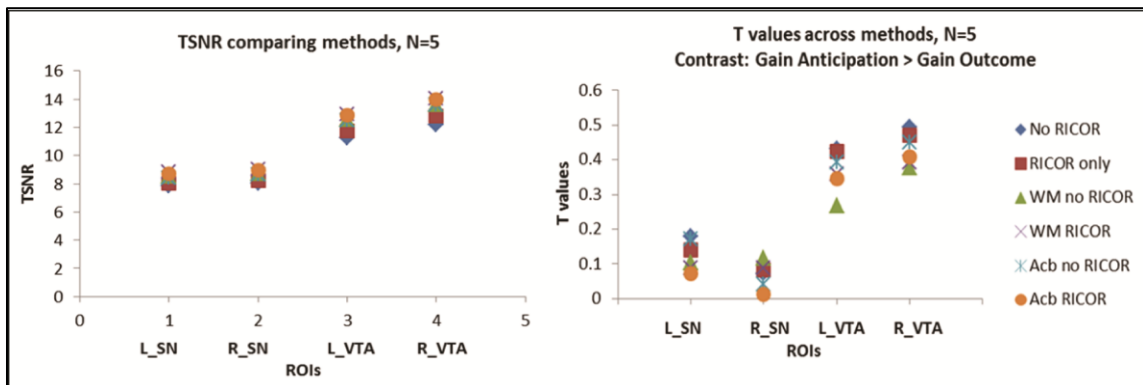
Figure 37: **TSNR and T-values from the regressor of no interest analysis.** TSNR (left panel) and T-values for a contrast of interest (right panel) are shown here. The different methods compared include: No RICOR (no RETROICOR), RICOR only (RETROICOR only), WM no RICOR (WM without RETROICOR) , WM RICOR (WM with RETROICOR), ACb no RICOR (ACb without RETROICOR) , ACb RICOR (ACb with RETROICOR). Average over five individuals in the FFE sequence is shown here.

An FIR analysis was performed on the initial set of five FFE participants to observe task-related variance compared to the conventional statistical model using the canonical HRF. We could also estimate if a different HRF shape was evolving in these midbrain ROIs compared to the canonical curve. With respect to the cue onsets in the midbrain ROIs, we did not observe a distinguishing pattern for the HRF shape (See Figure 38). The F-statistics established that the FIR model did not explain significant task-based variance in the data: $F(84,996) < 1.1$ ($p > 0.26$) for $N = 4$, all regions and $F(56,664) < 1.35$ ($p > 0.05$) for $N = 1$, all regions.
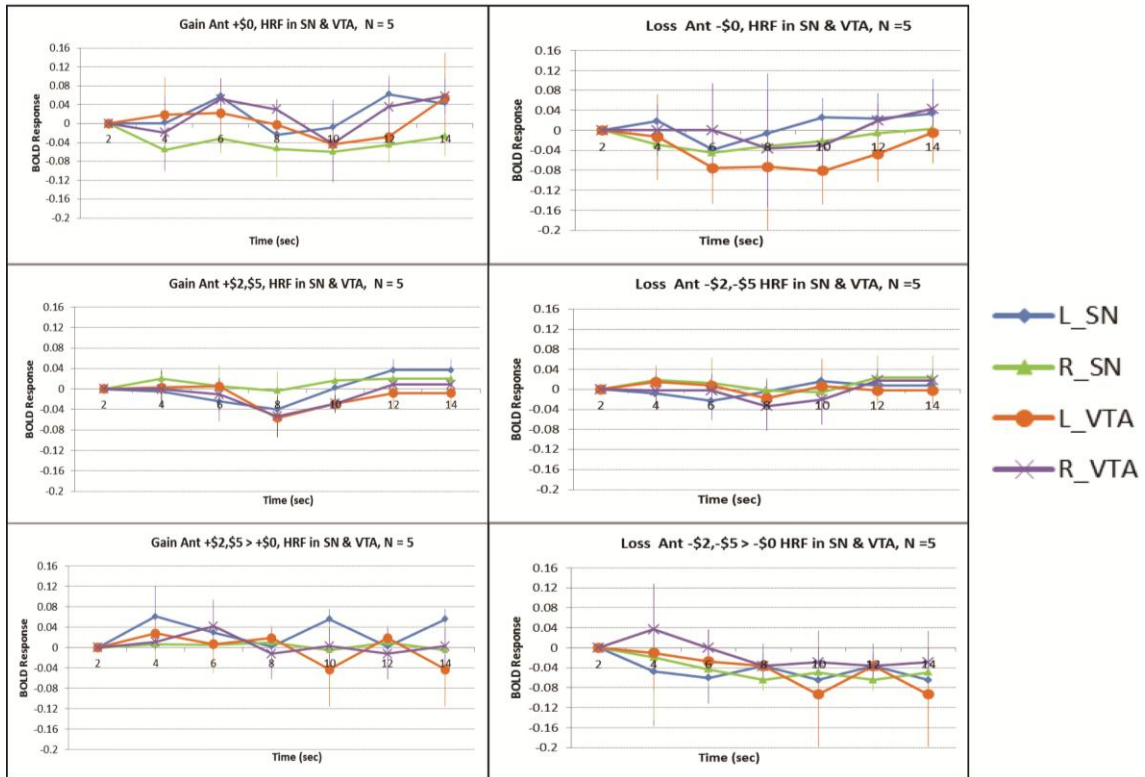
Figure 38: **HRF response in midbrain ROIs with respect to cue onset after FIR analysis.**
Events include: Gain Anticipation +$0, +$2 and +$5; Gain Anticipation +$2 and +$5 > +$0; Loss
Anticipation -$0, -$2 and -$5; Loss Anticipation -$2 and -$5 > -$0. Error bars represent 95%
confidence intervals. ROIs include left SN (L_SN), left VTA (L_VTA), right SN (R_SN) and
right VTA (R_VTA). Average over five individuals shown here.

The mean signal, noise and TSNR calculation between the SN and VTA with respect to the cortex in the three different sequences revealed a notable trend (Table 6). We observed that the mean signal in the cortex was approximately 1.5 times that in the SN (higher for the FFE scan). The mean signal in the cortex was almost comparable to that in the VTA across the three scans (slightly higher in the FFE scan). In contrast, the noise in the midbrain was approximately 1.5 or sometimes close to three times the noise in the cortex (in PRESTO and EPI). As a result, the TSNR in the cortex turned out to be approximately 3.25 times that in the SN and approximately 2.25 times that in the VTA.

Table 7: **Comparing mean signal, noise and TSNR between the cortex and the midbrain in FFE, PRESTO and EPI sequences.** Ratios between the cortex and the SN as well as the cortex and the VTA are shown here. In the noise column (middle section) the ratio between the midbrain vs. the cortex is also shown. Values represent the average of two participants.

Sequence	ROI	Mean Signal Ratio		Sequence	ROI	Noise Ratio		Sequence	ROI	TSNR Ratio
FFE	CTX/SN	2.17		FFE	SN/CTX	1.65		FFE	CTX/SN	3.71
PRESTO	CTX/SN	1.12		PRESTO	SN/CTX	2.92		PRESTO	CTX/SN	3.39
EPI	CTX/SN	1.07		EPI	SN/CTX	2.03		EPI	CTX/SN	2.69
Sequence	ROI	Mean Signal Ratio		Sequence	ROI	Noise Ratio		Sequence	ROI	TSNR Ratio
FFE	CTX/VTA	1.49		FFE	VTA/CTX	1.57		FFE	CTX/VTA	2.60
PRESTO	CTX/VTA	0.69		PRESTO	VTA/CTX	2.70		PRESTO	CTX/VTA	2.21
EPI	CTX/VTA	0.71		EPI	VTA/CTX	1.88		EPI	CTX/VTA	1.85

Discussion

The main goal of this study was to discuss the technical challenges associated with functional imaging of the midbrain at 7 T, particularly with regards to achieving reliable and reproducible BOLD signal changes in response to a task. A number of analysis techniques were explored in an attempt to investigate the loss of BOLD signal during a slow event-related fMRI task, which has been previously reported to activate the midbrain in group averages at lower MR field strengths. To investigate the source of the noise, we applied a known noise correction algorithm, RETROICOR, and used a regression approach that accounted for phase changes influencing the magnitude data. We also tested the efficacy of a 1-D navigator to correct for

between-shot phase errors and estimated the power spectrum frequency maps inside and outside the midbrain within the cardiac and respiratory frequency ranges. In an attempt to improve BOLD signal fidelity, we regressed out signal within ROIs (white matter, anterior cerebellum) that were not functionally correlated with the midbrain SN and VTA. Additionally, we employed a FIR model to detect task-related BOLD contrast when a canonical HRF shape was not assumed as a statistical model for fMRI analysis. Finally we explored the mean signal and noise in the midbrain and the cortex to examine if the TSNR distinction observed between these regions is driven by a signal difference or a noise difference.

Noise mitigation techniques

RETROICOR

The techniques utilized to control for noise in this study demonstrated that the common sources of physiological noise (cardiac pulsations and motion due to respiration) do not significantly contribute to noise in the midbrain. When RETROOICOR was applied to the high TR PRESTO and EPI scans, it marginally reduced the influence of respiration. However, it did not reduce noise in the cardiac frequencies. Moreover, the technique performed better for 2-D EPI scans compared 3-D PRESTO scans. The original RETROICOR algorithm developed by Glover and colleagues (Glover, Li et al. 2000) was shown to work effectively for single-shot 2-D EPI sequences in which each image is collected at a discrete time and unique cardiac and respiratory phases can be assigned for these images. The same principle may not hold true for multi-shot acquisitions since one TR does not represent an entire image. In 3-D multi-shot sequences (e.g., FFE), images are acquired over multiple TRs before the entire image is combined into a full volume (different lines of k-space collected at different times). Consequently, one image may span several cardiac cycles (~2) and a substantial fraction of a respiratory cycle. Thus RETROICOR did not perform adequately for the 3-D multi-shot sequences in the present study. Even though the original algorithm was shown to regress out physiological fluctuations in 2-D

168

single shot EPI sequences, we did not observe an improvement in the temporal stability of the data after RETROICOR was implemented (Figure 34). This suggests that there are other noise sources influencing TSNR at 7T which may not be problematic at lower field strengths.

Moreover, for the task-related fMRI scans in which a 2 second TR was used (EPI, PRESTO and FFE), RETROICOR did not show an improvement in the midbrain SN and VTA TSNR (Figure 34). As elaborated in Chapter III, with a 2 second TR, we can only sample up to 0.25 Hz which corresponds to the upper edge of the respiratory frequency range. Cardiac frequencies typically fall around 1 Hz (assuming a heart rate with an average of 60 beats per minute) and since our fMRI scans did not sample at this frequency range, cardiac frequencies aliased into lower frequency ranges (typically under 0.1 Hz). While RETROICOR may effectively regress out variance associated with respiration, it may not be able to manage the cardiac physiologic component. In fact, RETROICOR has been shown to not remove slower signal changes (~ 0.03Hz) induced by breath-to-breath variations in the depth and rate of breathing (Birn, Smith et al. 2008). Similarly, signal fluctuations less than 0.1 Hz have also been reported to not be effectively removed by RETROICOR (Shmueli, Gelderen et al. 2007). These low frequency fluctuations (< 0.1 Hz) can include breathing variability, resting state default mode network activity (~ 0.03 Hz), beat-to-beat variability in the cardiac rate and higher order harmonics of the cardiac frequencies being aliased to very low frequencies. In our data, the task-related frequency ranged from 0.07 to 0.1 Hz, which falls in the category of all these mixed physiologic noise variability. Hence it is possible that the task-related BOLD contrast is not detectable over and above these aforementioned noise variances.

When this task was implemented in lower field strength group fMRI studies, BOLD activity was reported in the midbrain. The cardiac frequency aliasing likely occurred in these studies, nonetheless they were able to detect BOLD signal contrast. The same is not true at 7 T. It should be noted though that the TSNR at 3 T in the midbrain is also significantly higher. When we did the same task-based study at 3 T using a 2-D EPI scan, we found the TSNR in the SN to

be approximately 50 and the TSNR in the VTA to be approximately 60 (results not shown here). This means that there is at least a five-fold difference in the TSNR for the midbrain between 3 T and 7 T. Thus, if on average a 1% signal change is reported for a BOLD contrast at 3 T, we may need at least a 5% BOLD signal change for the same contrast at 7 T (assuming a linear improvement). We are certainly not accomplishing this level of BOLD signal change for any of our contrasts at 7 T across pulse sequences (see Chapter V, Figure 29). Therefore in order to improve BOLD sensitivity at 7 T, we may either need to increase our scan time to include more runs (and therefore increase the power of detectability, (Murphy, Bodurka et al. 2007)) or find ways to reduce the temporal variance in the midbrain. Given that it is impractical to conduct extremely long scans on participants, techniques for reducing noise will be necessary to make it feasible to perform 7 T fMRI of the midbrain. Intriguingly, the observation that temporal variance is much higher at 7 T may be explained if the variance is a result of increased BOLD signal fluctuations rather than noise.

Phase regression

The phase regression analysis was implemented in order to reduce variance in the phase of an image that may be influencing BOLD signal detectability in the magnitude image. In this analysis, blood vessels larger than the smallest intra-cortical veins (> 25 μm radius) are considered oriented, producing changes in both magnitude and phase data during neural activation. In comparison, vessels in the capillary beds are randomly oriented, producing changes only in magnitude data (Menon 2002). BOLD contrast arising from task-based activations is known to primarily take place in the capillary bed area. Therefore suppressing the influence of spurious activations seen in larger vessels would be potentially beneficial for improving task-related signal detectability. This approach, nevertheless, did not improve TSNR or t-statistics for the PE-MD task-specific contrasts in the midbrain (Figure 37). One possible explanation may be that the midbrain is densely vascularized with arteries and veins running through the SN and

VTA in an oriented fashion. Some of the vessels running through the midbrain ROIs are greater than 25 μm in radius, risking the chance that BOLD activity in these regions will be regressed out by the algorithm. Hence, the phase regression technique may be potentially removing BOLD activity associated with a task in the SN and VTA.

A limitation of the phase regression algorithm is that during the correction process, the phase is unwrapped temporally. The phase of an image can vary in time and space and produce wraps (huge changes in signal intensity) around magnetic susceptibility areas (air-tissue interface, CSF-tissue interface). The ventral portion of the midbrain is proximal to the IPF which has CSF flowing through it. This area is thus highly susceptible to phase wraps. In and near these regions the noise is rather high and therefore the phase values cannot be estimated accurately. In addition, it is also known that more fluctuations are observed in phase than magnitude images for areas of low SNR (particularly in the midbrain) (Gudbjartsson and Patz 1995). In fact phase looks more like noise in these regions thereby impeding the effectiveness of the regression algorithm.

1-D navigator

One of the disadvantages of using multi-shot imaging sequences is the possibility of developing phase instability errors between shots as different lines of k-space are acquired at different times. The primary reason for the instability is the use of multi-shot EPI in these 3-D sequences. As part of the reconstruction process, the EPI trains in these sequences get interleaved to make an entire imaging volume. If there are changes in the magnitude or phase of an image in these EPI trains, the EPI trains get interleaved differently producing periodic changes in k-space. These become evident as image artifact ghosts that can overlap with a region of imaging interest in space. If the EPI trains get interleaved differently over time, then the ghosts can also vary over time, producing temporal variance that is not related to the task.

A 1-D navigator echo was tested to mitigate this problem while imaging the midbrain using PRESTO and FFE sequences. In resting state scans, with the use of a navigator, the FFE

and PRESTO sequences demonstrated a TSNR improvement in the cortex, but very little

improvement in the midbrain. In fact the PRESTO sequence revealed a lower TSNR in the

midbrain compared to the FFE sequence (Figure 35). The 1-D navigator algorithm also has

limitations. 1-D means that the correction algorithm averages phase changes for the entire volume

(approximately 15-23 mm slab thickness in our study) instead of performing it for every slice or

for any particular direction. This may not be very efficient and most likely will not produce a

good estimate of phase instabilities because B_0 fluctuations can vary shot-to-shot as a result of

breathing (variation through different points in the volume). Thus the phase of the MR signal is

different in each shot and thus cannot benefit from a global estimation of phase performed by the

1-D navigator. A 2-D phase correction algorithm may have to be used in future studies to observe

a more accurate estimate of phase in multi-shot sequences (Barry, Klassen et al. 2008).

In comparison, when using 2-D single-shot EPI, these temporal instabilities were not

present, but instead, the image suffers from huge spatial geometric distortions, reducing our

confidence in estimating the actual location of a structure of interest. In all our EPI studies,

shimming allowed for the midbrain area to be mostly spared from these geometric distortions.

Even so, we did not see a big difference in the TSNR for the 2-D EPI compared to the 3-D

sequences (Chapter V, Figure 29). This suggests that the cause of the low TSNR observed in our

study is not related to specific differences in imaging sequences.

Power spectrum maps

Noise in the midbrain influenced by physiological measures cannot be easily mitigated by

common noise correction algorithms, so other strategies were employed to characterize the noise

profile in the midbrain. Resting state high temporal resolution PRESTO and EPI sequences were

used to create power spectrum maps that exhibited a spatial distribution of the noise in the

midbrain. This approach revealed conflicting evidence. The PRESTO sequence displayed noise

concentrated around the midbrain area, possibly contributed by CSF pulsatility in the IPF and the

arteries surrounding the lateral edges of the midbrain. When examining the noise spectrum map, we also observed that while the high noise power was localized in the cardiac pulsatility regions (IPF and arteries), these high power values did not propagate into the adjacent midbrain areas (SN and VTA). This indicates that noise in the midbrain ROIs cannot be fully explained by the cardiac noise. EPI on the other hand, demonstrated greater noise in the respiratory frequency range around the midbrain in comparison to the cardiac frequency (although not as prominent as PRESTO). Again, the spatial distribution of the noise did not propagate into the midbrain regions suggesting that respiration may not be the dominant noise factor in the midbrain DA nuclei. In addition, power spectrum density curves (not shown in this paper) in midbrain DA nuclei for both sequences revealed peaks in the cardiac and respiratory frequencies along with peaks in other frequencies. This implies that while there is noise in this region of the brain, the source of the noise cannot be fully explained by the cardiac and respiratory fluctuations.

One might wonder why we did not perform prospective cardiac gated fMRI for our study, especially since this type of scan has been previously implemented for subcortical fMRI studies at 1.5 T and 3 T (Guimaraes, Melcher et al. 1998; D'Ardenne, McClure et al. 2008). The main purposes of cardiac gated scanning include controlling for bulk motion associated with brainstem movement and reducing the temporal signal variability contributed by cardiac fluctuations. From the retrospective cardiac gated scan performed in Chapter IV, we observed that the net displacement for the midbrain was approximately 0.05 mm in the anterior direction and 0.11 mm in the caudal direction. This motion represents approximately 2-5% of a typical voxel size (1.33 mm^3), suggesting that even with cardiac pulsatility, the brainstem is not moving very much. Additionally, the power spectrum maps from the current study indicated that while temporal instability is present in the areas neighboring the midbrain (arteries and CSF flow regions), it does not propagate into the SN or VTA region. This suggests that the temporal variations produced by cardiac and associated CSF pulsations are not a prominent noise source in the midbrain. Thus we

determined that it may not be beneficial to perform prospective cardiac gating for our midbrain fMRI studies.

Moreover, there are many factors to take into consideration for successfully implementing cardiac gated imaging at 7T. These include optimizing imaging parameters to accommodate for the long T1 relaxation time and variability in T1 saturation because of the variability in when the images are acquired. Additionally, various imaging parameters may have to be optimized to ensure that the entire imaging volume can be attained within a cardiac cycle. In particular, for fMRI paradigms with a repetition times of two or more seconds, this may involve sacrificing slice coverage or going to a lower resolution. This may not be feasible for fMRI in the midbrain when attempting to study distinct and differential BOLD responses in adjacent brain structures. Moreover, for a slow event-related jittered fMRI paradigm (as used in our study), retrospectively assigning the appropriate imaging volume to the respective trial onset can become problematic if there is variability in the timing of image acquisition. For 3-D multi-shot sequences, this becomes more complicated since the repetition time refers to the time between shots and the entire imaging volume is not acquired in one shot. Again, we may have to compromise on the imaging information that can be obtained within one cardiac cycle.

Techniques for improving BOLD signal detectability

Our results indicated that the known noise sources were not substantially contributing to the low TSNR. We next examined if the BOLD signal was being accurately detected. We regressed out signal in ROIs (white matter, anterior cerebellum) that were known not to be functionally correlated with the midbrain SN and VTA. A low temporal correlation was revealed between the midbrain area and these non-interest regions and the analysis did not improve the TSNR (Figure 37). This means that removing shared variance with regions that have potentially similar cardiac and respiratory profile does not improve the TSNR in the midbrain. These

174

findings imply that there may be other sources of temporal variability influencing the temporal profile of the midbrain SN and VTA that cannot be accurately accounted for at this time.

Additionally, we implemented an FIR model that did not assume the canonical HRF shape for statistical modeling of the task data. Different parts of the brain are known to have a different HRF shapes (Aguirre, Zarahn et al. 1998; Handwerker, Ollinger et al. 2004), so we hypothesized that the loss in signal may be due to an inappropriate statistical HRF model for estimating the midbrain BOLD signal. This approach, however, did not show a consistent pattern of the HRF shape in the midbrain SN and VTA for various task-related contrasts of interest (Figure 38). Moreover, the F-statistics revealed that the FIR model did not explain significant task variance our data. One of the assumptions we make is that the HRF shape is similar throughout the entire volume of the midbrain ROI. The HRF at every single time point was thus estimated by averaging signal from the entire midbrain SN or VTA, potentially being susceptible to partial volume effects. Our results did not show any striking HRF pattern, so we concluded that there is either low inherent signal or high sources of noise confounding signal detectability.

It should also be noted that unlike a retinotopic visual stimulus such that can robustly activate the visual cortex, a similar localizer is not available for the midbrain. This makes it difficult to observe robust BOLD related signal and establish a baseline BOLD signal level within the DA midbrain system.

As our final analysis, we explored the difference in the mean signal and noise within the midbrain and the cortex since we know that cortical BOLD contrast has been previously reported at 7 T in the visual cortex (Barry, Strother et al. 2011). Our aim was to examine whether the TSNR difference between these regions was driven by a signal difference or a noise difference. We observed that the mean signal was almost comparable in both the midbrain as well as the cortex (Table 7, even though the FFE values are uncertain). However, the noise in the midbrain was double or sometimes triple that of the cortex. Consequently, the TSNR in the cortex turned out to be double or triple that of the midbrain. The source of this high level of noise in the

175

midbrain is uncertain at this time. The common sources of noise contributing to low signal were explored in this study, but they did not sufficiently the present uncertainty. One possibility is that the intrinsic fluctuations between homologous midbrain regions are being particularly sensed at the 7T. The partial correlation values observed between the left and right SN and the left and the right VTA in the FFE and the PRESTO scans demonstrated such a trend (Chapter V, Table 6), but we did not have the statistical power to test for significance between correlations. The fidelity of such correlations may have to be further researched using a robust functional connectivity analysis with a larger sample size.

Conclusion

In conclusion, this study investigated the various technical challenges related to functional imaging of the midbrain DA system. Various noise and signal mediating techniques were implemented to measure an improvement in the TSNR within the midbrain. We observed that physiological noise sources associated with cardiac pulsatility and respiration were not markedly influencing noise in the midbrain. An evaluation of signal and noise difference between the midbrain and the cortex also revealed a considerable noise component within the midbrain compared to the cortex. The source of this noise in the midbrain is uncertain and cannot be accurately localized at this time. Further testing on the intrinsic fluctuations between the homologous midbrain SN and VTA regions will have to be explored as a potential factor that is contributing to strong temporal variance, but are not as random noise.

References

Aguirre, G., E. Zarahn, et al. (1998). "The variability of human, BOLD hemodynamic responses." NeuroImage **8**(4): 360-369.

Barry, R., S. Strother, et al. (2011). "Data-driven optimization and evaluation of 2-D EPI and 3-D PRESTO for BOLD fMRI at 7 Tesla: I. Focal coverage." NeuroImage **55**(3): 1034-1043.

Barry, R. L., L. M. Klassen, et al. (2008). "Hybrid two-dimensional navigator correction: A new technique to suppress respiratory-induced physiological noise in multi-shot echo-planar functional MRI." NeuroImage **39**(3): 1142-1150.

Barry, R. L., J. M. Williams, et al. (2010). "Evaluation of preprocessing steps to compensate for magnetic field distortions due to body movements in BOLD fMRI." Magn Reson Imaging **28**(2): 235-244.

Birn, R. M., M. A. Smith, et al. (2008). "The respiration response function: the temporal dynamics of fMRI signal fluctuations related to changes in respiration." Neuroimage **40**(2): 644-654.

D'Ardenne, K., S. M. McClure, et al. (2008). "BOLD Responses Reflecting Dopaminergic Signals in the Human Ventral Tegmental Area." Science 319(5867): 1264-1267.

Dagli, M., J. Ingeholm, et al. (1999). "Localization of cardiac-induced signal change in fMRI." NeuroImage **9**(4): 407-415.

Duvernoy, H. M. (1999). Human Brain Stem Vessels: Including the Pineal Gland and Information on Brain Stem Infarction. Berlin, Springer-Verlag.

Glover, G. H., T.Q. Li, et al. (2000). "Image-based method for retrospective correction of physiological motion effects in fMRI: RETROICOR." Magn Reson Imaging **44**(1): 162-167.

Gruetter, R. (1993). "Automatic, localized in vivo adjustment of all first- and second-order shim coils." Magn Reson Med. **29**(6): 804-811.

Gruetter, R. and C. Boesch (1992). "Fast, Noniterative Shimming of Spatially Localized Signals. In Vivo Analysis of the Magnetic Field along Axes." Journal of Magnetic Resonance **96**(323-334): 323.

Gudbjartsson, H. and S. Patz (1995). "The Rician Distribution of Noisy MRI Data." Magn Reson Med **34**(6): 910-914.

Guimaraes, A. R., J. R. Melcher, et al. (1998). "Imaging Subcortical Auditory Activity in Humans." Hum Brain Mapp. **6**(1): 33-41.

Haacke, E. M., R. W. Brown, et al. (1999). <u>Magnetic resonance imaging: physical principles and sequence design</u>. NewYork, Wiley-Liss.

Handwerker, D. A., J. M. Ollinger, et al. (2004). "Variation of BOLD hemodynamic responses across subjects and brain regions and their effects on statistical analyses." <u>NeuroImage</u> **21**(4): 1639-1651.

Hornak, J., J. Szumowski, et al. (1988). "Magnetic field mapping." <u>Magn Reson Med</u> **6**(2): 158-163.

Krebs, R. M., M. G. Woldorff, et al. (2010). "High-field FMRI reveals brain activation patterns underlying saccade execution in the human superior colliculus." <u>PLoS One</u> **5**(1): e8691.

Krüger, G., A. Kastrup, et al. (2001). "Neuroimaging at 1.5 T and 3.0 T: comparison of oxygenation-sensitive magnetic resonance imaging." <u>Magn Reson Med</u> **45**(4): 595-604.

Lindquist, M. A. and T. D.Wager (2007). "Validity and power in hemodynamic response modeling: a comparison study and a new approach." <u>Human Brain Mapping</u> **28**(8): 764-784.

Menon, R. S. (2002). "Postacquisition suppression of large-vessel BOLD signals in high-resolution fMRI." <u>Magn Reson Imaging</u> **47**(1): 1-9.

Murphy, K., J. Bodurka, et al. (2007). "How long to scan? The relationship between fMRI temporal signal to noise ratio and necessary scan duration." <u>Neuroimage</u> **34**(2): 565-574.

Naidich, T. P., H. M. Duvernoy, et al. (2009). <u>Duvernoy's Atlas of the Human Brain Stem and Cerebellum: High-Field MRI, Surface Anatomy, Internal Structure, Vascularization and 3 D Sectional Anatomy.</u> New York, Springer-Verlag Wien.

Pruessmann, K., M. Weiger, et al. (1999). "SENSE: sensitivity encoding for fast MRI." <u>Magn Reson Med.</u> **42**(5): 952-962.

Schneider, E. and G. Glover (1991). "Rapid in vivo proton shimming." <u>Magn Reson Imaging</u> **18**(2): 335-347.

Schroth, G. and U. Klose (1992). "Cerebrospinal fluid flow. I. Physiology of cardiac-related pulsation." <u>Neuroradiology</u> **35**(1): 1-9.

Schroth, G. and U. Klose (1992). "Cerebrospinal fluid flow. II. Physiology of respiration-related pulsations." Neuroradiology **35**(1): 10-15.

Shmueli, K., P. v. Gelderen, et al. (2007). "Low-frequency fluctuations in the cardiac rate as a source of variance in the resting-state fMRI BOLD signal." NeuroImage **38**(2): 306-320.

Soellinger, M., S. Ryf, et al. (2007). "Assessment of Human Brain Motion Using CSPAMM." Journal of Magnetic Resonance Imaging **25**: 709-714.

Triantafyllou, C., R. D. Hoge, et al. (2005). "Comparison of physiological noise at 1.5 T, 3 T and 7 T and optimization of fMRI acquisition parameters." NeuroImage **26**(1): 243-240.

Versluis, M. J., J. M. Peeters, et al. (2010). "Origin and reduction of motion and f0 artifacts in high resolution T2*-weighted magnetic resonance imaging: application in Alzheimer's disease patients." NeuroImage **51**(3): 1082-1088.

Wall, M. B., R. Walker, et al. (2009). "Functional imaging of the human superior colliculus: an optimised approach." NeuroImage **47**(4): 1620-1627.

Weisskoff, R. (1996). "Simple measurement of scanner stability for functional NMR imaging of activation in the brain." Magn. Reson. Med **36**(4): 643-645.

Yamada, S., M. Miyazaki, et al. (2008). "Visualization of cerebrospinal fluid movement with spin labeling at MR imaging: preliminary results in normal and pathophysiologic conditions." Radiology **249**(2): 644-652.

CHAPTER VII

CONCLUSIONS AND FUTURE DIRECTIONS

Conclusions

The main goal of this work involved studying the structure and function of the midbrain dopaminergic (DA) substantia nigra (SNc) and ventral tegmental area (VTA) using high resolution MRI at 7 T. Functionally, non-human primate research in these midbrain nuclei have reported an association between DA activity and behaviors involving reward-related learning (Schultz and Romo 1990), motivation (Salamone 1996; Ikemoto and Panksepp 1999), attention (Redgrave, Prescott et al. 1999), novelty processing (Reed, Mitchell et al. 1996; Kakade and Dayan 2002), and other goal-directed functions (Schultz 1998). Neuroimaging functional MRI (fMRI) studies in humans at lower field strengths have reported BOLD (blood oxygen level dependent) activation maps in the VTA and SN for tasks involving reward related learning (Berns, McClure et al. 2001; D'Ardenne, McClure et al. 2008; Buckholtz, Treadway et al. 2010), motivation and novelty (Bunzeck and Duzel 2006). The imaging protocols in these studies could not, however, distinctly localize BOLD activity in the VTA and SNc.

Anatomical evaluation of the midbrain

We began by optimizing the MR imaging parameters that would enable us to accurately view the anatomy of the midbrain at high resolutions. Even though neuromelanin sensitive T1-weighted scans had detected contrast in the brainstem (Sasaki, Shibata et al. 2006), the T1-weighted proton density scans we explored did not display contrast sensitivity for differentiating accurate boundaries of midbrain structures, internal substructure nor microvasculature. Upon testing various T2- and T2*- weighted sequences, we observed that a two-dimensional (2-D)

180

Gradient and Spin Echo (GRASE) scan exhibited particular delineation of the midbrain outline and detailed anatomy within midbrain nuclei. Similarly, a T2*- weighted three-dimensional (3-D) Fast Field Echo (FFE) scan revealed excellent visual contrast within the midbrain, particularly highlighting the vascularized segments of the red nuclei and the dorsal and ventral components of the SN. Contrast sensitivity in the iron-containing midbrain nuclei was of particular importance in accurately tracing the boundary of the VTA, which does not have cell-specific magnetic susceptibility features. Only one previous study (4 T using SWI) had reported similar levels of contrast, although they did not highlight substructure nor microvascular detail (Manova, Habib et al. 2009). From our anatomical studies, a voxel size of 0.4 x 0.4 x 2 mm^3 was established as optimal for detecting the midbrain structures of interest and for accurately measuring contrast to noise ratios (CNRs). A TE between 16-22 ms exhibited the highest CNR between the SN and VTA. An axial oblique slice orientation positioned over the midbrain extending from the superior edge of the pons to the inferior edge of the basal ganglia was determined as the area of imaging coverage.

This imaging protocol was then tested for reliability in ten individuals. Both the GRASE and FFE scans exhibited consistent anatomical detail in the midbrain area. The T2*-weighting of the FFE scan made it particularly sensitive to both the poorly and densely vascularized zones of the red nucleus (RN) and the microvasculature in the SN (e.g., visibility of vessels traveling laterally toward the cerebral peduncles). The T2- and T2*- weighting of both the GRASE and FFE scans also made them sensitive to detect substructure within the SN (pars compacta and pars reticulata), although this distinction was more apparent in the FFE scans. A segmentation algorithm enabled volumetric tracing of the SN, VTA and RN (Li, Kao et al. 2008). From this tracing step, the absolute volume of the SN, VTA and RN (across GRASE and FFE scans) were approximated to be 740 mm^3, 156.5 mm^3 and 214.3 mm^3 respectively. These values were much larger than what was reported through estimates using brainstem atlases (Paxinos and Huang 1995; Mai, Paxinos et al. 2008). There was no volume difference observed between the lateral

sides of the SN and the RN. However, the VTA did show a small difference between sides, suggesting that the method of volume tracing for the VTA may not be entirely reliable since its boundaries were estimated with reference to neighboring topographic landmarks. Nonetheless, the anatomical detail observed across individuals using both the GRASE and FFE scans provided confidence in discretely detecting contrast in the midbrain regions and using it as a framework for localizing BOLD activity in fMRI studies. Accurate contrast detection of midbrain anatomy can also be beneficial in clinical settings for the purpose of localizing structural changes associated with neurodegenerative pathologies (as in Parkinson's disease).

Functional evaluation of the midbrain

Given that we were able to successfully characterize the anatomy of the midbrain, we moved toward functional imaging of the midbrain. Again, it was necessary to optimize certain parameters, some of which could be translated from the parameter settings that were used in the anatomical scans. Because the T2* values of the SN (14 ms) and VTA (28 ms) were different, an echo time (TE) of 20 ms was arbitrarily chosen. This value was approximately halfway between the T2* values of the SN and VTA. Using this as one of the imaging parameter constraints, we optimized other scan parameters. 2-D single-shot EPI and 3-D multi-shot FFE scans were compared at different voxel resolutions, volume acquisition times and SENSE factors. We additionally evaluated signal quality and temporal stability using temporal signal to noise ratios (TSNR). Visually, the EPI images displayed greater distortion around the sinuses and ear canals compared to the FFE images. The midbrain areas were spared of distortions because the shim box was centered on that area. Moreover, the FFE images had higher TSNR in the midbrain SN and VTA compared to the EPI, although this difference was not significant. At the chosen TE of 20 ms, a voxel resolution of 1.33 mm^3 with a volume acquisition time of 2 s proved to be most favorable for imaging the midbrain with minimal distortion, maximum slice coverage (14 slices for EPI and 12 slices for FFE) and highest TSNR. SENSE factors of 3 for the EPI scans and 3.1

182

for the FFE scans were also established as optimum within the other imaging parameter constraints. We determined that both the EPI and FFE sequences could be used as candidate pulse sequences for performing functional imaging of the midbrain.

A retrospective cardiac-gated scan was also employed to evaluate the degree of brainstem motion as a result of cardiac pulsatility. This scan measured the displacement of the midbrain at various positions along the cardiac cycle. We observed that the overall brainstem displacement was less than 5% of the voxel volume (1.33 mm^3) over the course of an entire cardiac cycle. This suggests that while motion associated with cardiac pulsatility is present, it is not contributing greatly to the noise in that area. Additionally, we examined the efficacy of RETRIOCOR as a post-processing step to reduce the influence of cardiac pulsatility and motion associated with respiration in the midbrain. RETROICOR was able to mitigate the effects of respiratory noise. However, since cardiac frequencies were aliased to lower frequency zones, RETROICOR did not reduce the impact of this physiologic noise factor.

After standardizing an imaging protocol, we implemented fMRI scans across individuals using a modified version of the monetary incentive delay task (Knutson, Westdorp et al. 2000; Knutson, Fong et al. 2003) that included reward prediction error. Non-human primate work has shown that dopamine neurons signal in response to a change in the timing of the expected reward as well as a change in the magnitude of the reward (Schultz 1998; Schultz and Dickinson 2000). We examined potential changes in BOLD response associated with DA activity when the magnitude of the reward was increased or decreased from the expected amount. In a single participant for a 3-D FFE scan, we observed small BOLD activations in the midbrain SN and VTA at low uncorrected voxel level p-values for various contrasts of interest. When the threshold was made more stringent, the activations in the midbrain disappeared. Moreover, at lower thresholds, we observed BOLD activations around and outside the midbrain, likely representing false positives. This decreased our confidence in the ability to detect BOLD activation in the midbrain.

Across participants and in 2-D EPI, 3-D FFE and 3-D PRESTO sequences, neither significant nor trend level BOLD activation were observed. When we extracted percent signal change values in individual ROIs for various contrasts of interest, we did not observe a consistent pattern of BOLD responses across sequences. BOLD percent signal change was approximately < 2% in the midbrain for contrasts of interest shown in previous studies to robustly activate this area. The t-statistics for these contrasts of interest were low (< 1) implying low signal sensitivity or high noise variance in these regions. Previous 3 T studies had reported robust midbrain activation for this type of task, so the source of the dearth of BOLD signal activation was uncertain.

TSNR values were low in the midbrain as well (approximately 10 for the SN and approximately 16 for the VTA), with little difference across 2-D and 3-D sequences. The 2-D EPI TSNR was slightly higher than the 3-D FFE and PRESTO, especially within the VTA. Temporal correlations between homologous ROIs (left and right SN; left and right VTA) were moderately strong compared to the non-homologous pairs. This was more evident when partial correlations between homologous midbrain ROI pairs demonstrated stronger correlations than non-homologous pairs, after accounting for the shared variance with the neighboring white matter. These temporal correlations imply that the 7 T may be particularly sensitive to intrinsic fluctuations between the midbrain ROI pairs that are unrelated to task-specific BOLD modulations. More participants will need to be assessed in the future to increase statistical power for testing significant differences in these correlations.

Technical challenges of functional imaging in the midbrain

The low TSNR prevented us from observing any task-related BOLD contrast, so we determined to examine whether the reason for the signal paucity was due to high noise or low signal. Various noise reducing techniques were explored in an attempt to gauge the noise profile in the midbrain. Among these were RETROICOR, a phase regression algorithm, a one-

dimensional (1-D) phase navigator correction algorithm, and power spectrum spatial maps in the cardiac and respiratory frequency ranges. Confirming our aforementioned findings, RETROICOR did not improve the TSNR within the midbrain SN or VTA. As elaborated in Chapter VI, RETROICOR has certain limitations and may not effectively resolve aliased cardiac signals and frequencies under 0.1 Hz. Similarly, phase regression did not improve the TSNR in the midbrain. It is possible that the phase in the midbrain (particularly in the ventral areas close to the interpeduncular fossa) cannot be accurately estimated due to differences in phase unwrapping at the liquid-tissue boundaries. Consequently, phase cannot be well-differentiated from noise, reducing the effectiveness of the algorithm to properly regress out noise. If a spatial unwrapping technique were to be implemented together with the temporal unwrapping steps, phase regression may prove to be more effective for the midbrain. In addition, the uniform orientation of blood vessels in the midbrain SN and VTA area may result in the removal of task-related BOLD data, since the algorithm is known to remove any noise in oriented vessels greater than 25 μm in radius.

3-D multi-shot sequences are known to be susceptible to phase errors between shots and these errors can produce ghosting artifacts that vary in space and time. Therefore, we implemented a 1-D phase navigator algorithm to correct for potential multi-shot phase errors. This procedure displayed an improvement in the cortex for both PRESTO and FFE scans. It did not, however, improve the TSNR in the midbrain. The spatial power spectrum maps created using the high temporal resolution fMRI data revealed low contribution of cardiac and respiratory noise within the midbrain SN and VTA. In fact, both EPI and PRESTO sequences exhibited higher noise in the arteries and the CSF flow regions surrounding the midbrain, particularly within the cardiac frequency range. This noise source did not, however, propagate into the midbrain regions, suggesting that it may not be an important source of noise influencing the midbrain. The same result prevailed in the respiratory frequency range.

In order to examine the lack of the signal in the midbrain VTA and SN, a regressor of no interest analysis and an FIR analysis was explored to improve BOLD signal detectability. A regressor of no interest GLM analysis with ROIs in the midbrain white matter (cerebral peduncles) and the anterior cerebellum did not improve the TSNR nor did it improve the t-statistics for various contrasts of interest. This implies that although the white matter and the anterior cerebellum were not functionally correlated with the midbrain, their shared temporal variance did not significantly influence the variance within the midbrain SN or VTA.

Furthermore, while the FIR approach did not make any assumptions regarding the HRF shape, it was unable to significantly explain task-related variance in the midbrain. We observed that the HRF shape for various contrasts of interest did not show a consistent temporal BOLD profile. Because cortical 7 T fMRI studies have been successful in detecting BOLD signal in the cortex, we attempted to compare the mean signal and the noise difference between the midbrain and the cortex. We observed that while the midbrain and the cortex had comparable mean signal, the noise was two or three time larger in the midbrain compared to the cortex.

Hence, in the aforementioned techniques, we attempted to reduce or eliminate all known sources of noise in the midbrain and explore alternative methods for improving BOLD signal detectability in the midbrain. We are uncertain about the additional noise sources in the midbrain impeding signal detectability at this time. The temporal correlations between homologous midbrain ROIs (left SN with right SN; left VTA with right VTA) suggest that the 7 T may be sensitive to intrinsic fluctuations related to functional connectivity between midbrain regions. These fluctuations may be accounted for by temporal variations observed in the data and may not be reflective of random noise.

In summary, this dissertation attempted to evaluate the structural architecture and the functional significance of the human midbrain dopaminergic system at 7 T. While the anatomical component of our aims had fruitful results, further functional imaging research must be conducted

to reliably detect BOLD contrast in the midbrain. Through this endeavor, one can certainly appreciate the difficulty as well as the potential benefit of imaging the midbrain at 7 T.

<div align="center">**Future Directions**</div>

Anatomical Applications

Imaging patients with Parkinson's disease

The accuracy and reliability of detecting anatomical contrast in the midbrain can be translated into clinical settings, especially in tracing structural changes associated with disease progression in neurodegenerative diseases. Parkinson's is a disease in which there is a known loss of DA neurons in the SNc (Fearnley and Lees 1991) and an increase in iron deposition within the SN (Dexter, Carayon et al. 1991). The source of MR imaging signal-intensity changes in Parkinson disease is not fully understood. There is conflicting evidence for the structural changes observed in Parkinson's patients as the disease progresses. Studies have shown a reduction in the width of the SNc, arising from an increase in iron content within the SNr or loss of DA neurons in the SNc (Duguid, Paz et al. 1986). Some studies have associated the structural changes with a "smudging" of the SNr hypo-intensity along with decreased distance between the RN and the SN (Drayer 1988). Other studies have shown T2-weighted hyper-intense signal intensity within the SNr or a loss of the hypo-intense signal intensity within this area (Braffman, Grossman et al. 1989; Stern, Braffman et al. 1989).

The region-based segmentation algorithm developed in the current work allows for quantification of the distance between and volume dimensions of various midbrain brain structures, especially at higher voxel resolutions. This technique may be further utilized to trace tissue-related structural changes occurring longitudinally in disease states. T2 relaxation time may also be another marker for measuring disease-related structural changes within the SN (Ordidge,

Gorell et al. 1994). R2' measurements in the SN at 3 T have been shown to correlate with simple motor scores in Parkinson disease (Gorell, Ordidge et al. 1995). These T2* measurements could be extended to observe correlations with various neuropsychological assessments. The intricate vascular architecture offered by the T2*- weighted scans in this work may also be helpful in evaluating vascular differences and changes in the SN complex over time.

There are numerous difficulties in imaging Parkinson's patients at the 7 T. Movement in Parkinson's patients can be a significant issue, particularly within the confined imaging space. While most movement in the disease can be controlled through medication, the mid to late-stage patients often have dyskinesia (involuntary movements), which can be extremely uncomfortable within the closed space of an MRI bore. Most MRI studies on Parkinson's patients to date have been conducted during the early stages of the disease. In order to view structural changes associated with disease progression, mid to late-stage patients would also need to be imaged, requiring an MR protocol which may necessitate sedation.

Parkinson's typically develops between 50-60 years of age. Consequently, there are several contraindications in scanning older adults. Metals stents, staples and other MR incompatible implants from previous surgeries can prevent patients from being scanned, therefore reducing the pool of subjects available for these anatomical studies. It is also difficult to assess which variables to control when stratifying patient cohorts. Age, disease duration (based on first prescription of medication), disease state reported by neurologist (Hoehn and Yahr staging scale, (Hoehn and Yahr 1967)), current medications and cognitive indications (depression, dementia, memory loss, visual hallucinations) are criteria by which to potentially stratify Parkinson's patients.

Functional Strategies

The unresolved noise in the functional data prohibits specific applications at this time. We can, however, consider alternate strategies that may allow us to investigate and target noise sources in the midbrain.

Power spectrum maps in the 0.02 – 0.1 Hz frequency range

The high temporal resolution scans collected in this work were used to create power spectrum maps in the respiratory (~ 0.15 - 0.25 Hz) and cardiac (~ 0.9 - 1.1 Hz) frequency ranges. As expected, these noise sources did not influence the noise in the midbrain SN and VTA. Different fluctuations have been shown to fall under the 0.1 Hz frequency zone. These fluctuations represent breath-to-breath variations in the depth and rate of breathing, beat-to-beat variability in the cardiac rate, higher order harmonics of the cardiac and respiration frequencies being aliased to very low frequencies, and default mode network activity (~ 0.03 Hz) (Shmueli, Gelderen et al. 2007; Birn, Smith et al. 2008). It will be beneficial to investigate the power spectrum maps in the 0.02 – 0.1 Hz frequency range to observe how the aforementioned varied noise sources are influencing noise in the midbrain. Additionally, since we know that the task frequency ranges between 0.07 – 0.1Hz, we can compare the power spectrum maps from 0.02 – 0.07 Hz and 0.07 – 0.1 Hz. This may provide additional information regarding the noise variability in these two frequency ranges. At this time, findings regarding the cardiac and respiratory higher order harmonics aliased into the lower frequency zones (under 0.1 Hz) remain inconclusive.

Filtering frequencies above 0.1 Hz

Because the task frequency range of interest falls specifically between 0.07 - 0.1 Hz, we can likely filter data above 0.15 Hz or even 0.1 Hz. This may show an improvement in TSNR as we attempt to remove known sources of noise in the respiratory and cardiac frequency ranges. We

must still, however, consider the influence of aliased and other frequency fluctuations under 0.1 Hz.

Independent Component Analysis

This approach may offer another perspective on the temporal variance in the midbrain areas without making assumptions as to the underlying causes of noise or signal changes in the data. fMRI data masked to cover the midbrain or the midbrain together with the basal ganglia exclusively may demonstrate the spatial and temporal variability within different components. One disadvantage of this approach is that we do not adequately know what the different components represent or signify. While the quasi-periodically varying noise sources associated with cardiac pulsations and respiration may be readily apparent, localized BOLD contrast and other inherent imaging artifacts (ghosting, distortions) may be difficult to resolve using ICA.

Imaging another subcortical area or using a different fMRI task

The midbrain DA system is intricately connected to parts of the basal ganglia. Therefore, it may be beneficial to attempt to observe BOLD contrast in the basal ganglia, especially within the segments pertaining to motor circuitry. The putamen and the caudate (part of the dorsal striatum) and associated motor circuitry have been shown to contribute to action-based learning when, for example, through trial-and-error, a participant learns stimulus-action-reward associations (Haruno and Kawato 2006; Wouwe, Ridderinkhof et al. 2011). This type of reward-based motor task , may reveal a robust BOLD signal in a subcortical region connected to the midbrain DA system.

Alternatively, since neuroimaging studies have shown BOLD activations in the SN/VTA to be associated with stimulus novelty (Bunzeck and Duzel 2006), a task combining novelty-seeking and reward dependence may be worthy of exploration (Krebs, Schott et al. 2009). This

may result in a task-related signal improvement in the midbrain area. Nonetheless, noise remains an impeding factor in reliably detecting BOLD signal.

Pharmacological MRI

A reliable stimulus that selectively localizes BOLD activity in the midbrain has not been identified. Therefore, it may be beneficial to explore pharmacological manipulation of the midbrain DA circuitry. BOLD activations have been reported in the mesolimbic VTA, nucleus accumbens and medial prefrontal cortex in studies involving humans with cocaine addictions (Breiter, Gollub et al. 1997; Kufahl, Li et al. 2005). Furthermore, when methamphetamine was used in psychostimulant-naive human participants, BOLD activations were observed in parts of the ventral striatum and the medial prefrontal cortex (major projection sites of the midbrain DA neurons)(Völlm, Araujo et al. 2004). The reproducibility of these pharmacologically-induced BOLD activations, particularly at 7 T, is uncertain. Moreover, the effectiveness of this approach in producing task-related BOLD contrast, beyond what was measured using the monetary reward-based task in the current work, is uncertain.

While some of the aforementioned functional imaging strategies may aid in improving BOLD signal detectability in the midbrain, additional research is required to mitigate the noise contributions discussed in this dissertation.

References

Berns, G. S., S. M. McClure, et al. (2001). "Predictability Modulates Human Brain Response to Reward." The Journal of Neuroscience **21**(8): 2793-2798.

Birn, R. M., M. A. Smith, et al. (2008). "The respiration response function: the temporal dynamics of fMRI signal fluctuations related to changes in respiration." Neuroimage **40**(2): 644-654.

Braffman, B. H., R. I. Grossman, et al. (1989). "MR imaging of Parkinson disease with spin-echo and gradient-echo sequences." American Journal of Roentgenology **152**(1): 159-165.

Breiter, H., R. Gollub, et al. (1997). "Acute effects of cocaine on human brain activity and emotion." Neuron **19**(3): 591-611.

Buckholtz, J. W., M. T. Treadway, et al. (2010). "Mesolimbic dopamine reward system hypersensitivity in individuals with psychopathic traits." Nat Neurosci. **13**(4): 419-421.

Bunzeck, N. and E. Duzel (2006). "Absolute Coding of Stimulus Novelty in the Human Substantia Nigra/VTA." Neuron **51**(3): 369-379.

D'Ardenne, K., S. M. McClure, et al. (2008). "BOLD Responses Reflecting Dopaminergic Signals in the Human Ventral Tegmental Area." Science **319**(5867): 1264-1267.

Dexter, D. T., A. Carayon, et al. (1991). "Alterations in the levels of iron, ferritin and other trace metals in Parkinson's disease and other neurodegenerative diseases affecting the basal ganglia." Brain **114**(4): 1953-1975.

Drayer, B. P. (1988). "Imaging of the aging brain. Part II. Pathologic conditions." Radiology **166**(3): 797-806.

Duguid, J., R. D. L. Paz, et al. (1986). "Magnetic resonance imaging of the midbrain in Parkinson's disease." Annals of Neurology **20**(6): 744-747.

Fearnley, J. M. and A. J. Lees (1991). "Ageing and Parkinson's disease: substantia nigra regional selectivity." Brain **114**: 2283-2301.

Gorell, J., R. Ordidge, et al. (1995). "Increased iron-related MRI contrast in the substantia nigra in Parkinson's disease." Neurology **45**(6): 1138-1143.

Haruno, M. and M. Kawato (2006). "Different neural correlates of reward expectation and reward expectation error in the putamen and caudate nucleus during stimulus-action-reward association learning." J Neurophysiol. **95**(2): 948-959.

Hoehn, M. and M. Yahr (1967). "Parkinsonism: onset, progression and mortality." Neurology **17**(5): 427-442.

Ikemoto, S. and J. Panksepp (1999). "The role of nucleus accumbens dopamine in motivated behavior: a unifying interpretation with special reference to reward-seeking." Brain Research Reviews **31**(1): 6–41.

Kakade, S. and P. Dayan (2002). "Dopamine: generalization and bonuses." Neural Networks **15**: 549-559.

Knutson, B., G. W. Fong, et al. (2003). "A region of mesial prefrontal cortex tracks monetarily rewarding outcomes: characterization with rapid event-related fMRI." NeuroImage **18**(2): 263-272.

Knutson, B., A. Westdorp, et al. (2000). "FMRI Visualization of Brain Activity during a Monetary Incentive Delay Task." NeuroImage **12**(1): 20-27.

Krebs, R. M., B. H. Schott, et al. (2009). "Personality Traits Are Differentially Associated with Patterns of Reward and Novelty Processing in the Human Substantia Nigra/Ventral Tegmental Area." Biol Pscyhiatry **65**(103-110): 103.

Kufahl, P., Z. Li, et al. (2005). "Neural responses to acute cocaine administration in the human brain detected by fMRI." NeuroImage **28**(4): 904-914.

Li, C., C.-Y. Kao, et al. (2008). "Minimization of Region-Scalable Fitting Energy for Image Segmentation." IEEE Transactions on Image Processing **17**(10): 1940-1949.

Mai, J. K., G. Paxinos, et al. (2008). Atlas of the Human Brain New York, Academic Press.

Manova, E. S., C. A. Habib, et al. (2009). "Characterizing the Mesencephalon Using Susceptibility-Weighted Imaging." American Journal of Neurobiology **30**: 569-574.

Ordidge, R., J. Gorell, et al. (1994). "Assessment of relative brain iron concentrations using T2-weighted and T2*-weighted MRI at 3 Tesla." Magnetic Resonance in Medicine **32**(3): 335-341.

Paxinos, G. and X.-F. Huang, Eds. (1995). Atlas of the Human Brainstem. San Diego, Academic Press.

Redgrave, P., T. J. Prescott, et al. (1999). "Is the short-latency dopamine response too short to signal reward error?" Trends in Neurosciences **22**(4): 146-151.

Reed, P., C. Mitchell, et al. (1996). "Intrinsic reinforcing properties of putatively neutral stimuli in an instrumental two-lever discrimination task." Animal Learning & Behavior **24**(1): 38-45.

Salamone, J. D. (1996). "The behavioral neurochemistry of motivation: methodological and conceptual issues in studies of the dynamic activity of nucleus accumbens dopamine." Journal of Neuroscience Methods **64**(2): 137-149.

Sasaki, M., E. Shibata, et al. (2006). "Neuromelanin magnetic resonance imaging of locus ceruleus and substantia nigra in Parkinson's disease." Neuroreport **17**(11): 1215-1218.

Schultz, W. (1998). "Predictive Reward Signal of Dopamine Neurons." Journal of Neurophysiology **80**: 1-27.

Schultz, W. and A. Dickinson (2000). "Neuronal coding of prediction errors." Annu Rev Neurosci. **23**: 473-500.

Schultz, W. and R. Romo (1990). "Dopamine Neurons of the Monkey Midbrain: Contingencies of Responses to Stimuli Eliciting Immediate Behavioral Reactions." Journal of Neurophysiology **63**(3): 607-624.

Shmueli, K., P. v. Gelderen, et al. (2007). "Low-frequency fluctuations in the cardiac rate as a source of variance in the resting-state fMRI BOLD signal." NeuroImage **38**(2): 306-320.

Stern, M., B. Braffman, et al. (1989). "Magnetic resonance imaging in Parkinson's disease and parkinsonian syndromes." Neurology **39**(11): 1524-1526.

Völlm, B., I. d. Araujo, et al. (2004). "Methamphetamine activates reward circuitry in drug naïve human subjects." Neuropsychopharmacology **29**(9): 1715-1722.

Wouwe, N. v., K. Ridderinkhof, et al. (2011). "Dose dependent dopaminergic modulation of reward-based learning in Parkinson's disease." Neuropsychologia.